UNIVERSITY OF OKLAHOMA

GRADUATE COLLEGE

STABILITY OF A DROPLET PINNED IN A CHANNEL UNDER GRAVITY

A DISSERTATION

SUBMITTED TO THE GRADUATE FACULTY

in partial fulfillment of the requirements for the

Degree of

DOCTOR OF PHILOSOPHY

By

HAIDER HEKIRI
Norman, Oklahoma
2012

STABILITY OF A DROPLET PINNED IN A CHANNEL UNDER GRAVITY

A DISSERTATION APPROVED FOR THE
SCHOOL OF AEROSPACE AND MECHANICAL ENGINEERING

BY

_____
Dr. Takumi Hawa, Chair

_____
Dr. Feng C. Lai

_____
Dr. Wilson E. Merchan-Merchan

_____
Dr. George Emanuel

_____
Dr. Brian Grady

To my mother and family
for their love and support

ACKNOWLEDGMENTS

I would like to gratefully and sincerely thank Dr. Takumi Hawa for being a great advisor. His guidance, understanding and most importantly his patience and support have given me the driving force to complete this work. He encouraged me not only to grow as a researcher, but also as an independent thinker. His mentorship and advice was vital in providing a well-rounded knowledge that is consistent with my long-term career goals. His financial support and his commitment to support me all the way through my graduate study have made reaching this achievement possible, so thank you for everything.

I also would like to thank Dr. George Emanuel for his tremendous help and constant support throughout my early days as a graduate student in Texas, until achieving this milestone in my life. I want to thank Dr. Wilson Merchan-Merchan for his support, valuable discussions and most importantly his friendship. In addition, I would like to thank Dr. Feng Lai for his help and valuable suggestions, some of which have become a significant part of my research work. I want to express my appreciation and gratitude to Dr. Brian Grady for being a member of my dissertation committee and for offering his help whenever I needed it.

I would like to thank the Department of Aerospace and Mechanical Engineering for offering me the opportunity of being a teaching assistant for the past years. Also a special thank you goes to Dr. Mistree Farrokh for his great advice and support throughout my doctoral study and beyond.

Most importantly, I would like to thank my mother Naima for her support, encouragement, quiet patience and unconditional love, which were the absolute foundation for this accomplishment.

I am also deeply grateful to my grandmother Fatma, my aunts: Latifa and Mounira, my uncles (and their families): Mokhtar, Kais, Hasan, Noureddine, Lotfi, and my brother and sister: Hakim and Imen, and all my family for their absolute love and support throughout my life.

I want to thank all my friends, especially my close friends Saeed and Mohannad for their sincere friendship, cherished memories and fun times. And, I have to thank Mrs. Emanuel for her love and encouragement, and also for her time and effort to drive with Dr. Emanuel to Oklahoma every time in order to attend all my doctoral events, including my convocation ceremony, this means a lot to me, thank you. To all the names I have mentioned above, you all made my life joyful and colorful. Thank you!

TABLE OF CONTENTS

LIST OF TABLES

LIST OF FIGURES

ABSTRACT

The stability of a two-dimensional, incompressible water droplet, with two cylindrical-caps that is pinned in a channel, is investigated through the development of an analytical model based on Yong-Laplace relationship. The center of mass of the droplet is derived analytically by assuming a perfectly 2-D circular shape of the droplet cap. The derived analytical expressions are validated through the use of CFD. In the simulations, FLUENT with a 2-D pressure based solver is utilized, and Gambit with 2-D rectangular mesh is used to generate the grid. The pinned droplet states are measured by the location of the center of mass. The stability of the droplet states without gravity is evaluated by the growth rate σ_H of the Hamiltonian of the system computed by CFD for various drop sizes.

When a droplet is suspended on the straight channel and under no gravity conditions, it is proven analytically and through the use of CFD that there is a critical droplet volume, V_{cr}, where asymmetric droplet states appear in addition to the basic symmetric states when the drop volume $V > V_{cr}$. It is demonstrated that when $V < V_{cr}$ the symmetric droplet states become stable and the growth rate of the disturbance decays. However, when $V > V_{cr}$ and the growth rate σ_H is positive, the symmetric states become unstable and the asymmetric states become stable. The bifurcation of asymmetric states at V_{cr} has a pitchfork nature, and the growth rate σ_H increases with the volume size.

When the channel holding the droplet is contracted, the pitchfork bifurcation diagram of the droplet system changes into two separate branches of equilibrium states. The analytical expression of those stability branches has been developed for various

contraction ratios ε. The primary branch describes a gradual and stable change of the droplet from a nearly symmetric to asymmetric state as the droplet volume, V, is increased. The secondary branch appears at a modified critical volume, V_{mcr}, and describes two additional asymmetric states for $V>V_{mcr}$. It is demonstrated that the large-amplitude states along the secondary branch are stable whereas the small-amplitude states are unstable.

When the capillary length and the channel width have the same order of magnitude, the effect of gravity is not negligible. An analytical expression is developed to find the effect on gravity, in terms of β, on the behavior of a vertically suspended droplet in straight channel. When gravity is considered, the droplet stability behaves similar to that of the contracted channel apart from one conditions; unlike the contracted channel, there exists a maximum volume on each of the primary and secondary branch where the droplet no longer sustains its weight. The maximum volume on the primary branch, V_{p_max}, is smaller than the maximum volume on the secondary branch, $V_{s\_max.}$ A critical β value, β_{cr}, is also found. That critical value describes the maximum condition at which the droplet will have only one range of solutions at the primary branch, and no longer sustain stability on the secondary branch. All analytical solutions are validated with CFD.

CHAPTER ONE: INTRODUCTION AND OBJECTIVES

1.1 Review of the Literature

Micrometer and less-than-a-millimeter droplets have been extensively studied to eliminate many mechanical components from several high performance consumer products, as well as practical application such as an electronically switchable adhesion devices [1], which are devices that combines two concepts: capillarity based adhesion through surface tension force, and device switch-ability through electronic controls. It uses grab and release process that operates within a fraction of a second (see Figure 1.1).

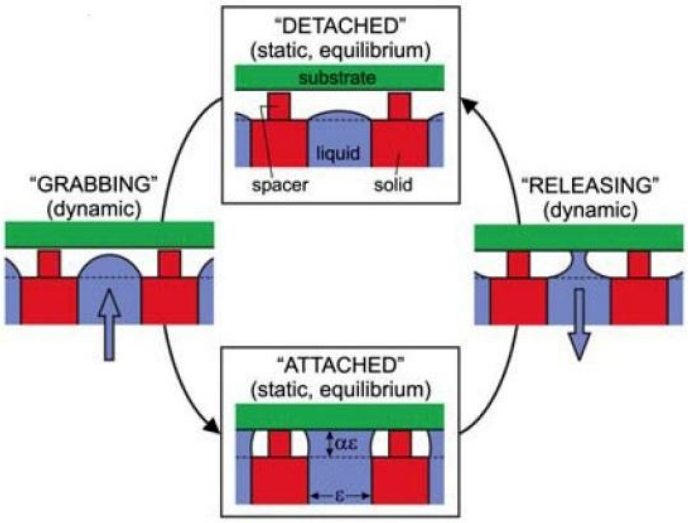

Figure 1.1 Capillary-based switchable adhesion device shows the grab-release process (*Courtesy of Vorgel and Steen [1]*)

Another practical application is the use of small-scale droplets as an electronic liquid pistons for capillarity based pumping [2]. With this application system, two adjoining magnetized fluid droplets can behave as an electronically controlled switch or

oscillator by balancing of the capillary, magnetic and inertial forces. As shown in Figure 1.2, the oscillatory movement can be utilized to move the adjacent liquid,

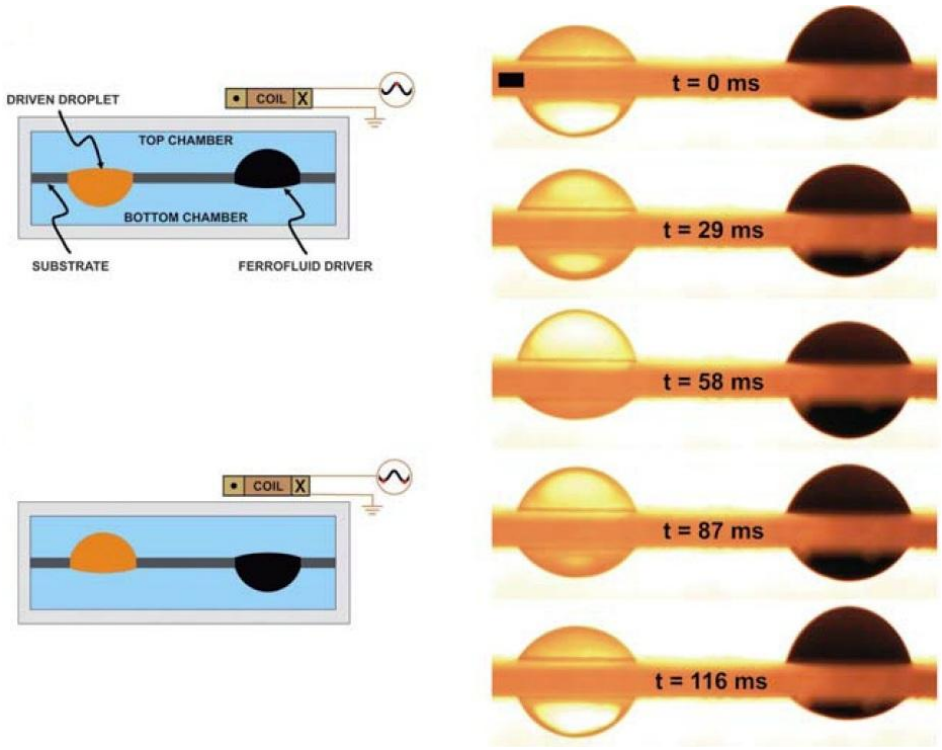

Figure 1.2 Electromagnetic liquid pistons for capillary-based pumping (*Courtesy of Malouin et al. [2]*)

forming an electromagnetic liquid piston.

As the design of integrated circuits become smaller and circuit devices become more dense, cooling techniques become very challenging, and as a result, micro-droplets have been utilized for thermal management [3] and cooling [4] applications for such devices. One of these devices uses a platform that employs nanoliter-sized discrete liquid droplets immersed in oil in order to independently actuate the cooling

droplets in user-defined patterns over an array of electrodes by use of electrowetting (see Figure 1.3), thus, getting rid of the need for external pumps.

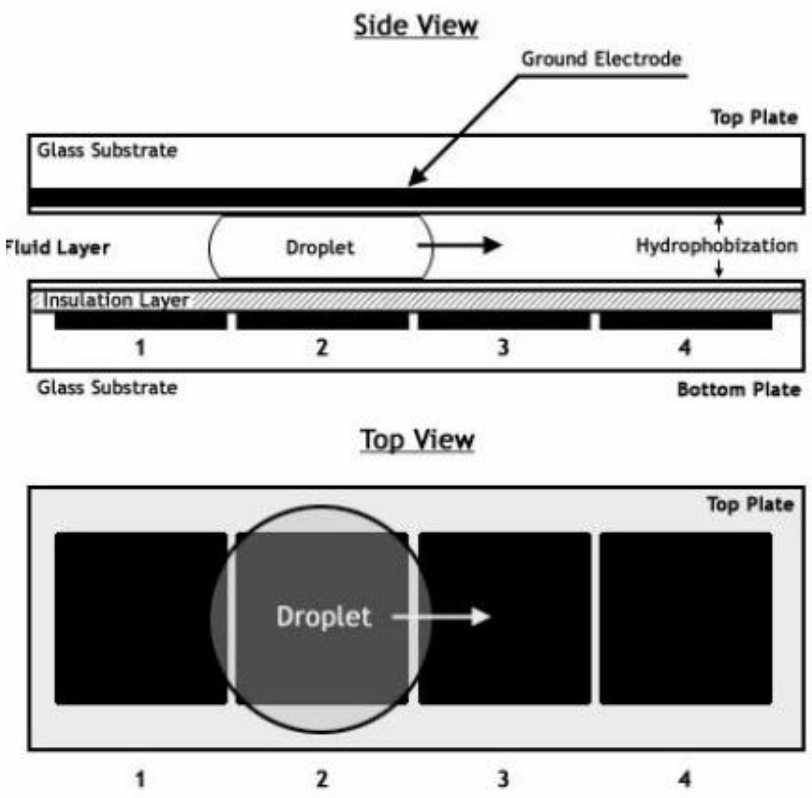

Figure 1.3 Schematic side and top views of the electrowetting chip (*Courtesy of Paik et al. [2]*).

The device has proven experimentally to reduce as much as 30% of temperature increase in small-scale electronic devices.

Also, there has been great interest recently in the use of small liquid droplet systems in surveillance and defense applications such as cell phone cameras and high performance camcorder that can be used in micro and large scale UAVs. Optical focusing in high performance cameras is usually a slow process, but most of the delay comes from time spent to mechanically move the camera's lenses until the image is in

focus. Lopez and Hirsa [5] have developed a liquid lens application for adaptive optics that can provide fast focusing response. Figure 1.4 shows the application of a micro-droplet developed by Lopez and Hirsa for a fast optical focusing device [6], using an oscillating liquid lens. The liquid lens is formed by trapping a drop of water in a hole on a Teflon plate, and a speaker generates a variable air pressure in one side of the plate. This variable pressure produces a frequency, which then varies the shape of the lens and its focal length (see Figure 1.5) depending on the instantaneous air pressure inside the chamber.

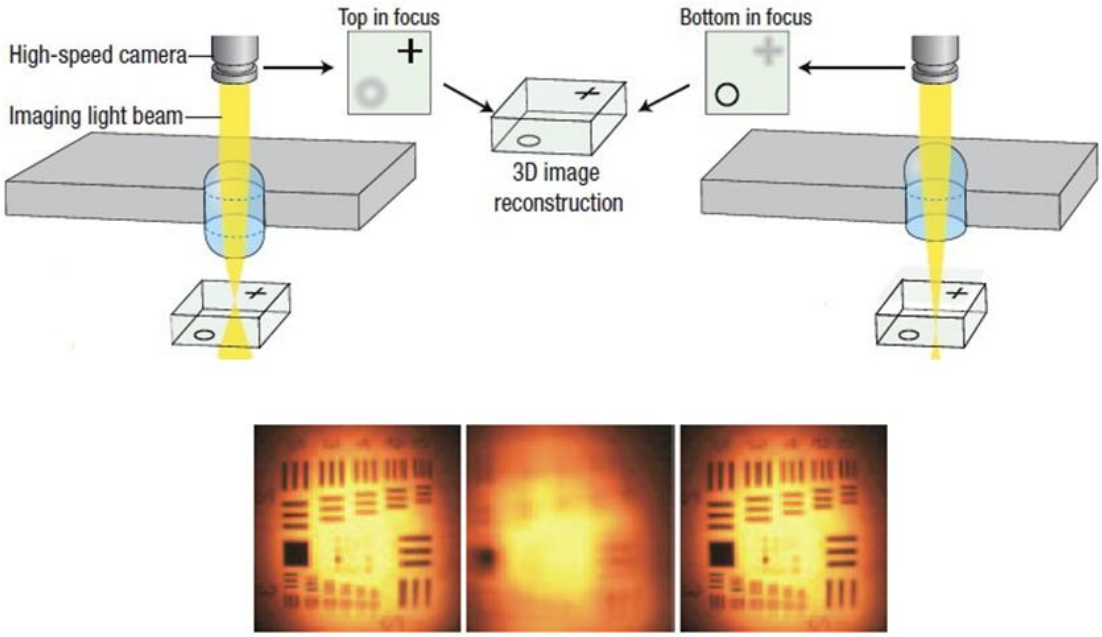

Figure 1.4 The schematics of fast focusing droplet (*Courtesy of Stan C.A [6]*)

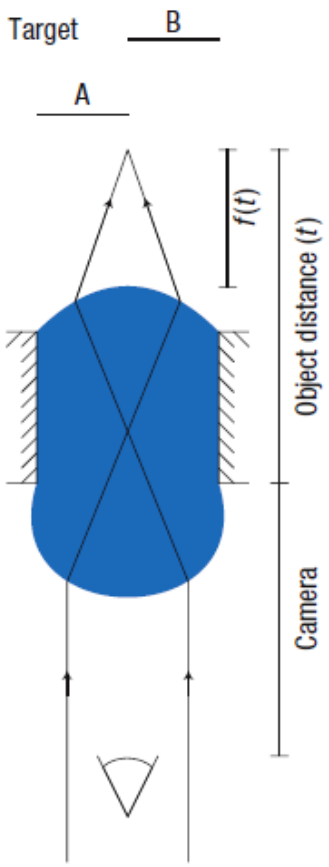

Figure 1.5 A liquid lens droplet shows the instantaneous focal length f(t) (*Courtesy of Stan C.A [6]*).

Small liquid droplets (1 mm or smaller) characteristically maintain their spherical shapes due to surface tension. When the characteristic length of a system is much less than the capillary length, surface tension becomes the dominant force on the bulk liquid. However, when the characteristic length becomes comparable to the capillary length, forces such as inertial and gravity force should be considered.

The coupled-droplet system that is pinned in a cylindrical tube and is slightly less than a millimeter in diameter has been studied experimentally by Lopez and Hirsa [5] and Olles et al. [7], and analytically investigated by Theisen et al. [8] for optical

applications. In their analytical model, they assumed that the shape of the free surface of the droplet remains spherical at all time. In their analyses, two droplet states were observed: 1) a symmetric state with two equal sized sub-hemispherical caps at both ends of the tube (Figure 1.6(a)), and 2) an asymmetric state with a super-hemisphere at one end and a sub-hemisphere at the other end (Figure 1.7). In our discussion, these top and bottom hemispherical caps are referred to as V_U and V_L, which are the upper and lower droplet cap volumes with radii of curvatures of R_U and R_L, respectively. Their theoretical analyses also found a critical volume of the droplet V_{cr}, which has a volume of $\frac{4}{3}\pi {r_t}^3$, where r_t is tube radius (3D case). Note that in Figure 1.6, V=1 when $V_U+V_L=V_{cr}$ and $V = \frac{V_U+V_L}{V_{cr}} = 1$, the derivation is discussed in Chapter 3. At $V_{cr,}$ asymmetric states appear as a pitchfork bifurcation nature when $V_U+V_L > V_{cr}$ (Figures 1.6 (b and c)).

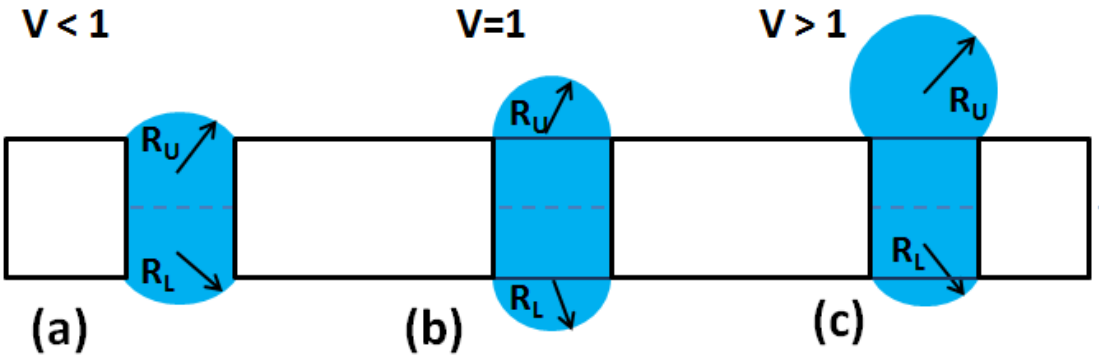

Figure 1.6 Various droplet states: (a) Droplet caps volume is less than critical volume V<1. (b) Droplet cap volume is equal to critical volume, R_U=R_L, V=1 (c) Droplet cap volume is greater than critical volume V>1.

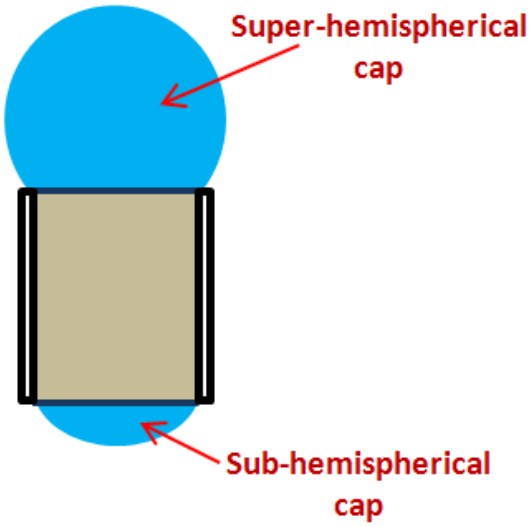

Figure 1.7 Super- and sub-hemispherical caps of a suspended liquid droplet

Slobozhanin and Alexander [9] have observed similar transition phenomena in their system (See Figure 1.8a). They considered that two droplets are suspended from a two circular holes of two equal radii in a horizontal plate and connected by a liquid layer that lays above the plate, which means that the droplets were coupled. When both of the hole sizes are the same, these droplets introduce a critical volume where asymmetric states appear as $V_{L1}+V_{L2} > V_{cr}$, and symmetric state appears as $V_{L1}+V_{L2} < V_{cr}$ (see Figure 1.8b). V_{L1} and V_{L2} are the two droplet cap volumes suspended from the two circular holes.

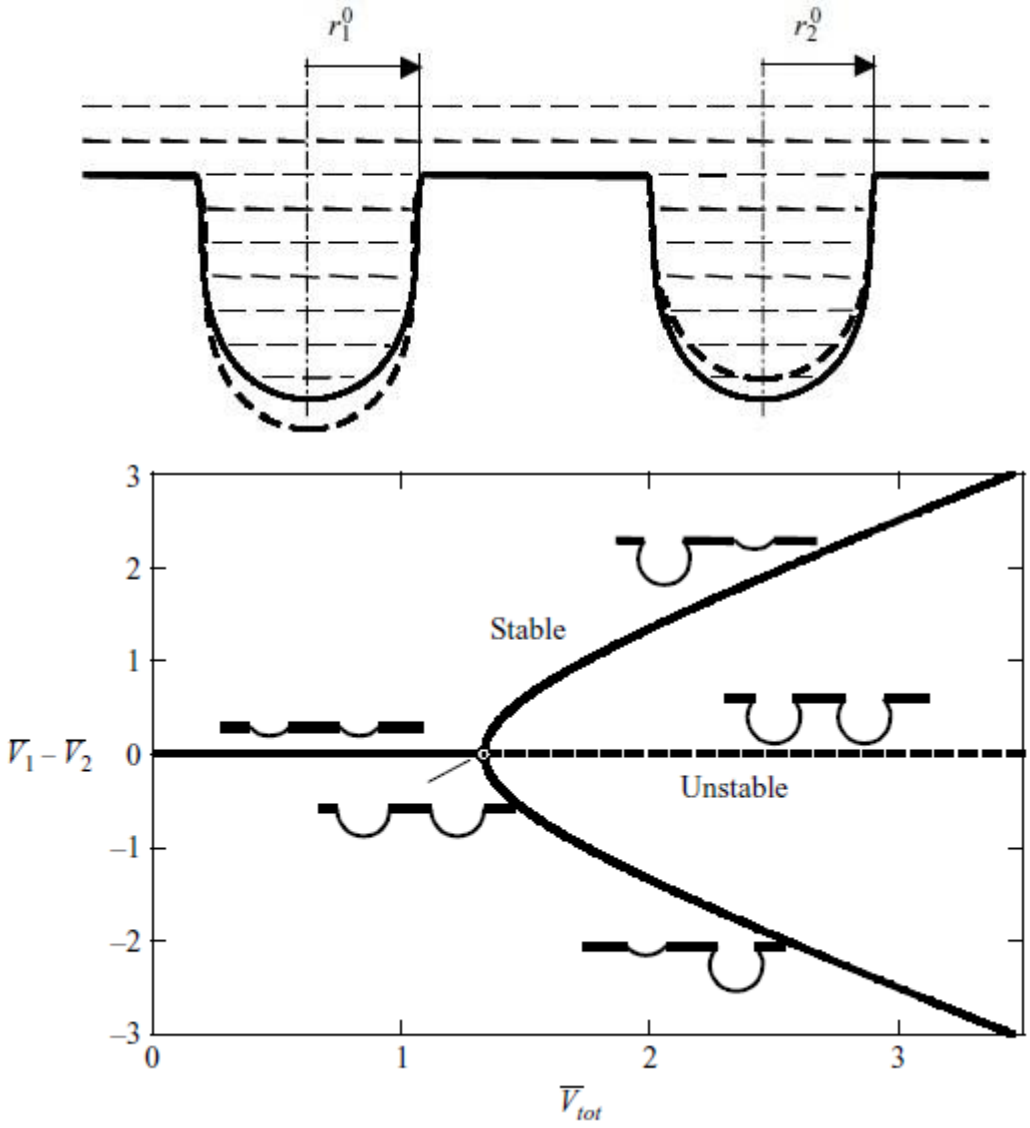

Figure 1.8 (a) The transition from the unstable to stable state. (b) Bifurcation diagram as found by Slobozhanin and Alexander (*Courtesy of Slobozhanin and Alexander* [9]).

Slater et al. [10] investigated a suspended droplet behavior subjected to periodic forcing and also observed a pitchfork bifurcation nature of the droplet profiles. They considered two spherical cap droplets pinned to a cylindrical tube. The movement of the droplet was modeled as a second-order nonlinear dynamical system, and the capillary pressure caused a force to act from either top or bottom of the droplet. That force is a

function of the cylindrical tube's radius squared. They also found that the shape of static droplets that are smaller than a millimeter is nearly spherical.

An experimental study by Russo and Steen [11] focused on an axisymmetric capillary liquid bridge formed between circular endplates. They showed a loss of symmetry of the liquid profile while preserving the liquid volume and increasing an aspect ratio of the cylindrical tube's diameter to its length beyond a critical value (see Figure 1.9). Their analysis demonstrated that the symmetric state loses its stability to asymmetric disturbances at the critical bifurcation breaking point (critical volume). Their experimental results supported their analysis.

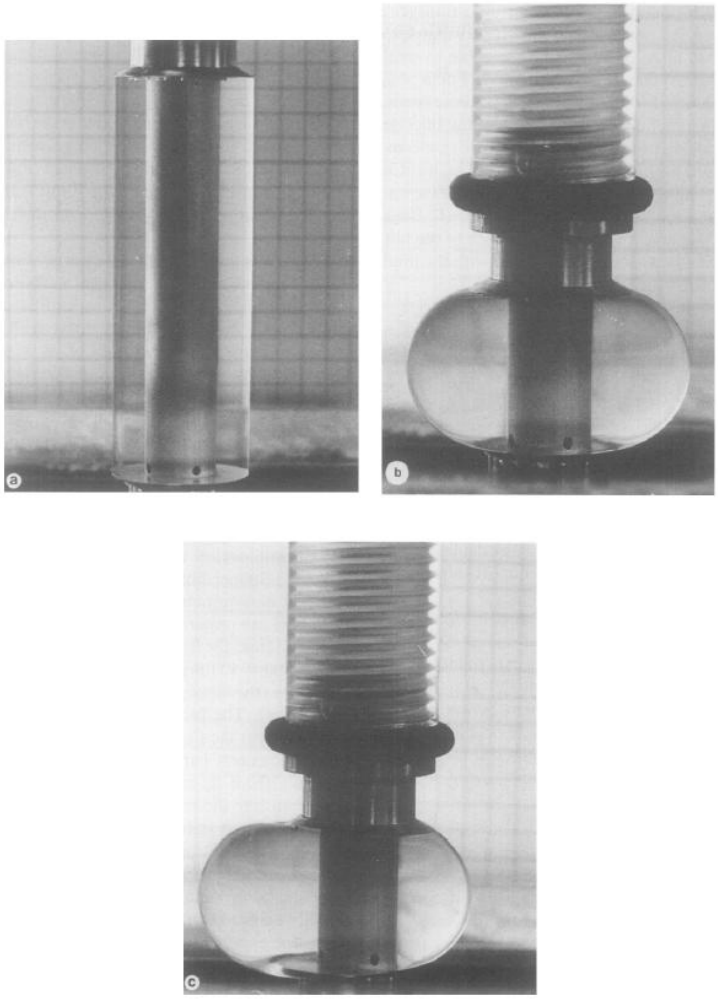

Figure 1.9 Photographs of liquid bridges during an experiment showing an initial cylindrical shape (top left), then a bridge symmetric distribution (top right), finally a loss of symmetry (bottom) (*Courtesy of Russo and Steen [11]*).

Ramalingam and Basaran's [12] considered a system that consists of sessile and pendant droplets coupled through a pipe that was filled with water under the condition of zero gravity (see Figure 1.10). Their double droplet system is surrounded by gas, and it was excited by the gas pressure surrounding one of the droplet caps. They also observed a pitchfork bifurcation nature of the droplet profiles when the pressures around the droplet caps were equal.

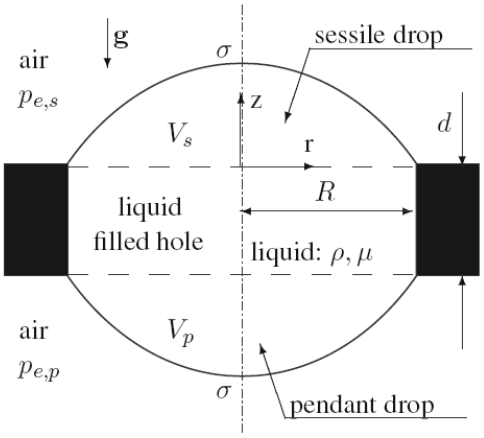

Figure 1.10 A schematic, as shown in reference [12], describes the sessile and pendant droplets coupled through a pipe (*Courtesy of Ramalingam and Basaran [12]*)

Bostwick's and Steen's [13] performed a numerical study on an inviscid spherical liquid droplets held by surface tension. In their study, they observed a deformation of a droplet's free surface. An oscillation was observed on the droplet with large cap volumes at large amplitudes. They found that the deformation of the large cap volumes has a significant effect on the droplet behavior and state. Such a droplet deformation will be observed in our study and discussed in Chapter 3.

Asymmetry in channel radii ($r_U \neq r_L$) changes the behavior of the bifurcation diagram. Slobozhanin and Alexander [9] investigated this asymmetry in their analytical study. They found that due to this asymmetry, the bifurcation diagram changes from its pitchfork nature to two separate stability branches, as shown in Figure 1.11. The first branch consists of only a stable state, whereas the second branch consists of stable and unstable states. The stable and unstable states bifurcate from a critical droplet volume that is larger than that of when the two channel radii are equal ($r_U = r_L$). All the states for the first and second branches were found to be asymmetric.

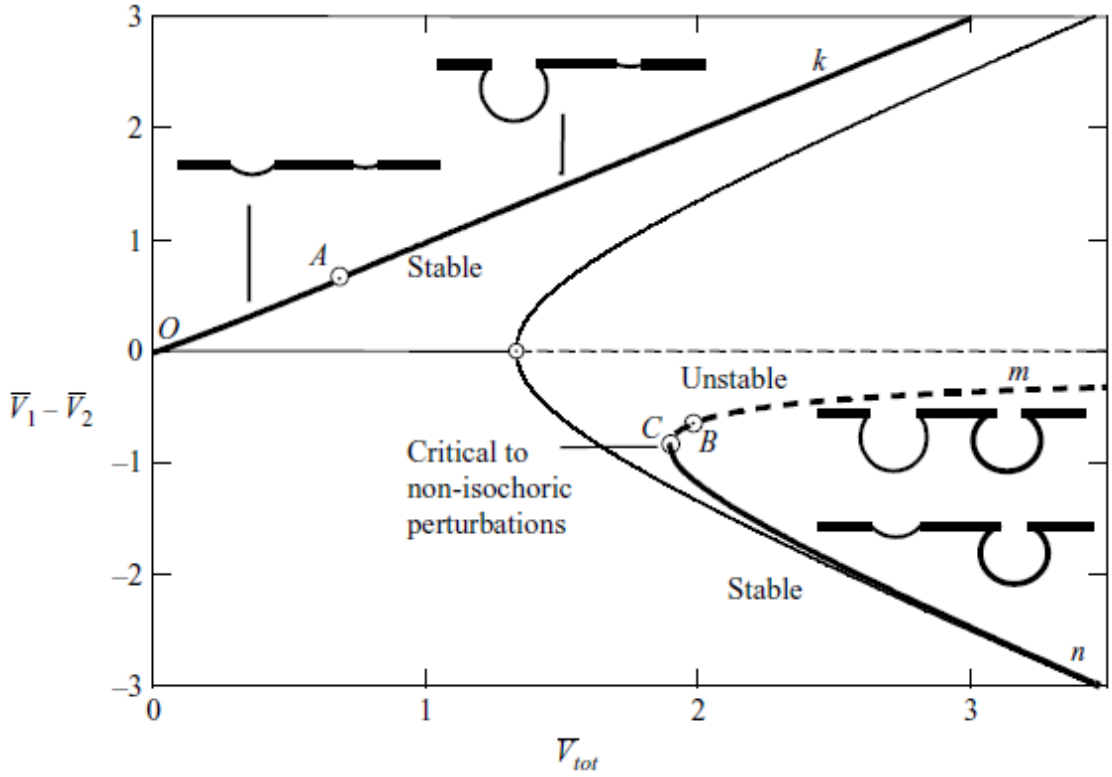

Figure 1.11 The change of the bifurcation diagram from its pitchfork nature to two separate stability branches (*Courtesy of Slobozhanin and Alexander* [9])

The contraction of a channel is a geometrical asymmetry, now the review of a force field asymmetry will be discussed; particularly the gravitational field. Both Lopez and Hirsa [5], and Theisen et al. [8] had also considered gravity in their analytical and experimental study. The gravitational force in both studies is counteracted by using an air pressure chamber controlled by an acoustic wave (see Figure 1.12). The effects of gravity, through the bond number, and the external pressure field are included in their

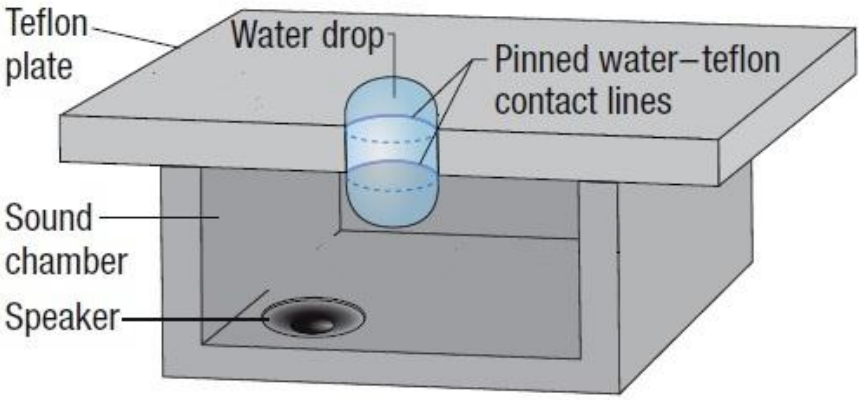

Figure 1.12 Water droplet trapped in a hole drilled in a Teflon plate, and a speaker generates variable air pressure on one side of the plate (*Courtesy of Lopez and Hirsa [5]*).

analytical model. The Bond number, which measures the relative importance of gravitational force to the surface tension force [14], is defined as $B = \rho g r_t^2/\gamma$, where ρ is the droplet density, g is the acceleration due to gravity, r_t is the tube radius, and γ is the surface tension.

Hirsa et al. [15] performed analytical as well as experimental work on low dissipation capillary switches using water droplets with the consideration of gravity and pressure bias resulted from electrochemical effect. In the experiment, electrical conductive rings were pushed into the end of each hole in the cylindrical tube holding the droplet. Then, an electrochemical actuator of a small voltage (1 Volt) was applied on the bottom ring relative to the top ring, which then oxidized the surfactant on the bottom droplet cap, and reduced it on the top cap. This process decreased the surface activity on the top and increased it on the bottom of the droplet, which as a result counterbalanced the gravity effect in their switch system. The gravity and pressure fields in their experiment changed the pitchfork bifurcation diagram into two separate

branches. One branch (primary branch) describes a stable and a smooth transition of droplet states from nearly symmetric to asymmetric states near V_{cr}. The other branch (secondary branch) describes asymmetric states, starts from a modified critical volume, $V_{mcr} > V_{cr}$, and bifurcates into stable and unstable states. The capillary length, $\sqrt{\gamma/\rho g}$, in their experiment was 3 mm for water, which was not much larger than their characteristic length of 0.89 mm. Their experiment was in a close agreement with their analytical model within the range of their droplet volumes they have studied.

Vogel and Steen's [1] work, which was illustrated earlier, is about a switchable adhesion device that is based on the surface tension force from a number of small liquid droplets that form liquid bridges between two objects. The droplets in the electronically controlled capillary adhesion device is suspended at zero voltage against gravity force until that force is counterbalanced using a small release of voltage of the opposite sign. Their method was similar to the work investigated by Malouin et al. in [16] and [2]. A time varying electromagnetic field was applied to control and to drive the coupled droplets through a cylindrical tube whose diameter is 1.7 mm.

Slobozhanin and Alexander [9] also investigated the gravitational effect on the stability of liquid droplet states analytically. Similar to the non-gravity case, the two droplets were suspended from two circular holes of two equal radii in a horizontal plate and connected by a liquid layer lying above the plate. Since the gravity has an effect on both droplets in the same direction, the droplet shape will be the same if the masses are the same, and different if the masses are different. In their analysis, gravity force was applied to both droplets with the same masses, and the effect of gravity on the two droplet caps cancels. Gravitational force, however, leads to the breakage of the

suspended droplets as the droplets reach to a maximum volume. The maximum droplet volume corresponded to the droplet characteristic length which is defined similar as the capillarity length, $\sqrt{\gamma/\rho g}$. Beyond that characteristic length, a breakage of the droplet was observed.

Similar behavior of a maximum volume of suspended droplet is also observed by Majumdar and Michael [17]. In their work they studied the equilibrium and the stability of equilibrium of two dimensional pendent drops hanging under gravity force and surface tension. They showed that a droplet can be deformed if it is hanged from a horizontal lower edge of a plate, when it does, there is a limit point (critical point for droplet volume) at which the droplet loses its stability, and that volume is the maximum droplet volume.

Slater et al. [10] found that at earth gravity, the shape of static droplets that are smaller than a millimeter are nearly spherical. However, they pointed out that the gravity at that small scale induces a small perturbation known as “g-jitter” in the droplet system, which increases the instability of certain droplet states.

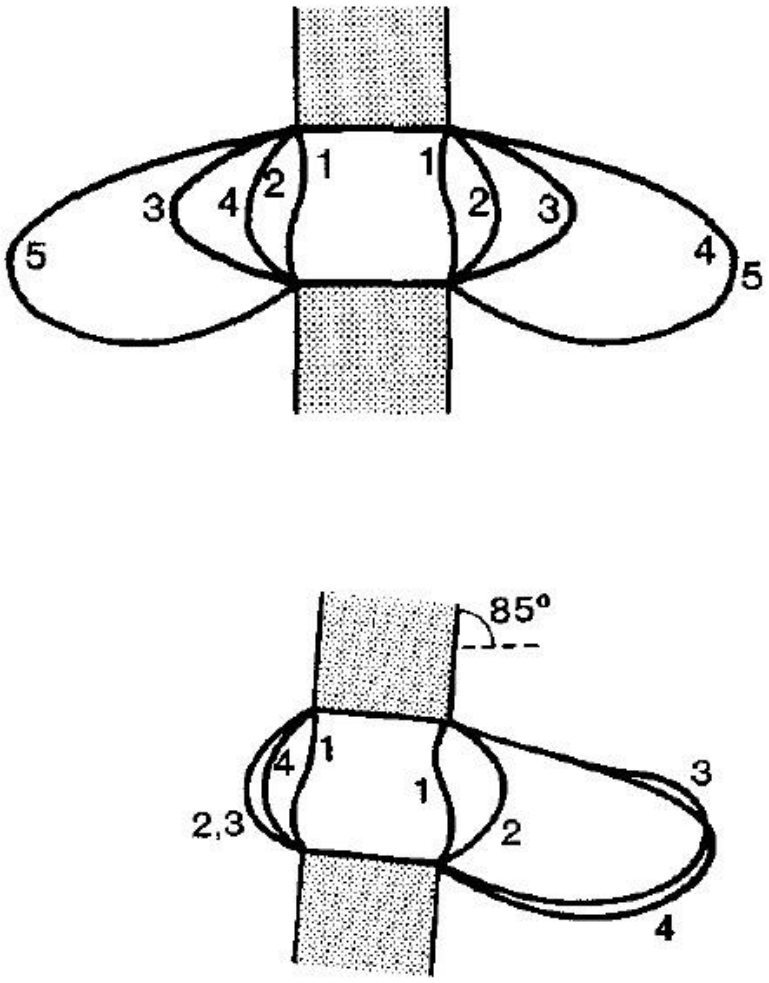

Figure 1.13 The symmetric behavior of a vertical liquid bridge under gravity (top), and loss of symmetry when tilted (bottom)

Chen and Chang [18] investigated a two-dimensional bridge [19] with a consideration of a slight tilt angle. This was a similar experimental orientation constructed by Russo and Steen [11]. With the absence of gravitational effects they found an existence of V_{cr} and an appearance of asymmetric bridge profiles depending on the aspect ratio of the bridge diameter (or channel length) to the liquid bridge length. When the vertical liquid bridge is considered with the introduction of gravitational effects, they found that the droplet volume will stay symmetric (see Figure 1.13) until it reaches a breaking point at $V_{max} = \frac{1.5}{\eta B} + 1$, where η is the bridge's diameter to length

ratio. However, when the bridge is tilted, a transition from symmetric to asymmetric state is observed.

1.2 Objectives

The review of the previous experimental and analytical investigations on stability of liquid droplets shows that a channel contraction and gravity have little effect on the dynamics when the bond number is near zero. However, even at $B \approx 0$, gravitational effects become significant when $V >> 1$, in addition, any level of channel asymmetry will cause an asymmetry in the droplet stability state. Therefore, both cases have to be further investigated. To our knowledge there is no CFD study that investigates the stability of the droplet suspended from a straight channel, or when subjected to either channel contraction or gravitational force effect. As the channel contraction ratio gets larger, the bifurcation diagram might deviate from its pitchfork nature of the straight channel case. Similarly, when gravity is considered and the droplet volume gets larger, the gravity force will have a large effect on the droplet behavior, and the bifurcation diagram might deviate from its pitchfork nature of the non-gravity case into the other form, such as two separate branches: primary and secondary branches. Moreover, for any value of gravity, there must be a maximum volume of the droplet to sustain its weight in the system, and the maximum volume of the primary branch might be different from that of the secondary branch.

Our analytical study investigates a droplet's behavior while suspended from a straight channel. In the study, the Hamiltonian of the droplet system is derived to verify its stability. When a channel contraction is introduced, the droplet stability behavior changes, and an analytical investigation is performed for various contraction ratios to

study this behavior. We also examined the effect of a gravitational force on a droplet suspended vertically in a straight channel. An analytical model is developed to test the various conditions of droplet behaviors under gravitational force effect. The validity of the analytical model, which assumes a spherical droplet cap volumes, is validated using CFD to determine the stable and unstable states. The physical mechanism that drives the droplet stability state is also studied and carefully reviewed. To our knowledge, there is no analytical investigation has been developed to study the limit of gravitational force effect on a vertically suspended droplet. Also no CFD examinations has been done to verify the droplet states under the previous conditions.

The dissertation is organized as follows: The CFD approach used to simulate the droplet system is described in Chapter 2, and then a detailed description of the analytical and CFD results of droplet suspended in a straight channel is shown in Chapter 3. The effect of a channel contraction, with analytical and CFD verifications is studied in Chapter 4. The gravity effect on the droplet transition behavior as well as droplet stability in the system obtained by the simulation and the analytical model are discussed in Chapter 5. Summary and future work are in Chapter 6.

CHAPTER TWO: NUMERICAL SCHEME

CFD simulations are used to demonstrate the droplet states and to validate the analytical model derived in later chapters. Dimensions of the simulation domain, shown in Figure 2.1, are described as follows. A half channel length, L, and width, r, are 0.91 mm and 0.84 mm, respectively. A water droplet is suspended in the channel surrounded by air in our system. Bulk water density and viscosity are ρ = 998.2 kg/m^3 and μ=1.003x10^{-3} kg/m-s, and air is at 1 atm pressure with a density, ρ_{air}=1.225 kg/m^3 and a viscosity, μ=1.7894x10^{-5} kg/m-s. The interfacial tension γ at the water-air interface is 0.072 N/m [8, 20]. The simulation domain is a closed rectangular space, and the channel is located at the center of the domain. Velocity boundary conditions along the domain boundaries and channel walls are the tangency and no-slip conditions during the simulations, respectively.

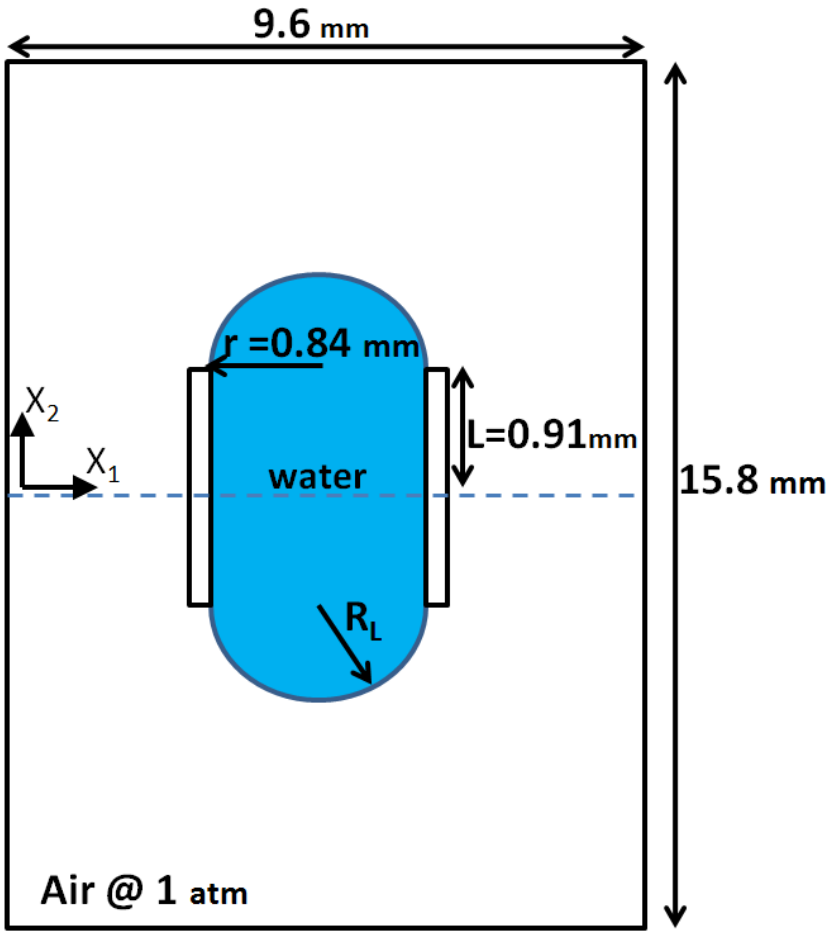

Figure 2.1 Geometry and dimension of the simulation domain

The two-dimensional incompressible viscous Navier-Stokes equations are solved for both air and water [21]:

$$\frac{\partial U_1}{\partial X_1} + \frac{\partial U_2}{\partial X_2} = 0, \tag{2.1}$$

$$\frac{\partial U_1}{\partial t} + U_1\frac{\partial U_1}{\partial X_1} + U_2\frac{\partial U_1}{\partial X_2} = -\frac{1}{\rho}\frac{\partial p}{\partial X_1} + v\left(\frac{\partial^2 U_1}{\partial X_1^2} + \frac{\partial^2 U_1}{\partial X_2^2}\right) + g_1 \quad \text{, and} \tag{2.2a}$$

$$\frac{\partial U_2}{\partial t} + U_1\frac{\partial U_2}{\partial X_1} + U_2\frac{\partial U_2}{\partial X_2} = -\frac{1}{\rho}\frac{\partial p}{\partial X_2} + v\left(\frac{\partial^2 U_2}{\partial X_1^2} + \frac{\partial^2 U_2}{\partial X_2^2}\right) + g_2 \quad , \tag{2.2b}$$

where the density ρ, pressure p, the kinematic viscosity $v = \mu/\rho$, and dynamic viscosity μ are constants during the simulation. Of course, the liquid pressure is not constant.

The parameters U and X represent the velocity and position vectors, respectively, and g is the gravitational acceleration. The subscripts 1 and 2 denote horizontal and vertical components of the vectors.

The CFD simulation is performed with the use of FLUENT 6.3 CFD package [20] with parallel processing. The number of processors ranges between 4 and 6 processors. FLUENT 6.3 CFD package is a control volume (CV) based solver that uses the CV technique to convert a general transport equation into an algebraic equation, which can be solved numerically as follows [20, 22]

$$\frac{(\rho\phi_c)^{t+\Delta t}-(\rho\phi_c)^{t}}{\Delta t}\Delta V + \sum_{faces}\rho_f\phi_f U_f A_f = \sum_{faces}\Gamma_f(\nabla\phi_f)A_f + S_\phi\Delta V, \qquad (2.3)$$

where ϕ is the transport equation variable. For example, for $\phi = 1$ the equation becomes the continuity equation, and for $\phi = U$ (velocity) it becomes the momentum equation. ΔV is the cell volume, Δt is the change in time, A is the cell area, and subscripts f and c denote for the variable value at the cell face and at the cell center, respectively (see Figure 2.2). U_f is the flow speed across a cell face, Γ is a coefficient for the diffusion term, and S is a source term. This numerical method integrates the transport equation at each control volume, which results in a discrete equation that expresses the conservation law on a control volume basis.

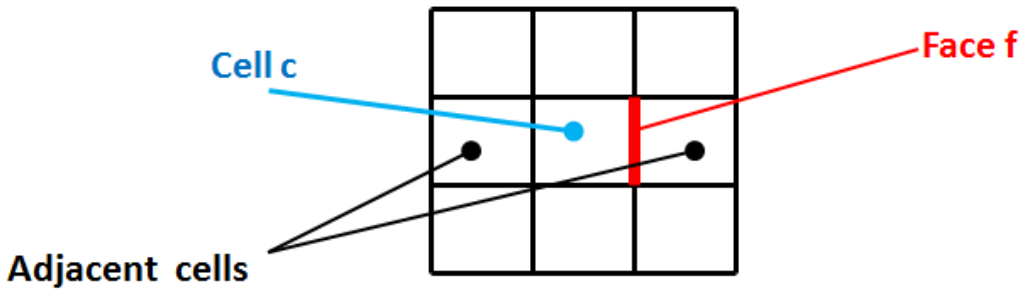

Figure 2.2 Cells structure with central cell in the middle

For domain discretization, a multiphase Volume of Fluid (VOF) model [23], for water and air, is used. This model, which is designed for two or more immiscible fluids, is an interface tracking technique that is applied to a fixed Eulerian mesh [24]. In each domain cell, the volume fraction of the liquid α is tracked, and a single set of the momentum equations is shared by the fluids. The VOF model can be applied in tracking any transient or steady liquid-gas interface, prediction of jet breakup [25], the dynamics of the liquid after a dam break [26], the dynamics of large bubbles in a liquid, sloshing, filling, free-surface flows, and stratified flows [23, 27-29]. The limitation of the VOF model is that it is restricted to the use of pressure-based solver; therefore, a density based solver is not applicable with this model [20]. In addition, a void or blank region, where there exists no fluids of any type in the simulation domain is not allowed in the VOF model. This indicates that, the control volume has to be filled with single- or multi-combinations of fluid phases. Furthermore, if the VOF model is used, the second-order implicit time step formulation cannot be used [20, 23]. Therefore, tracking the interface between the phases is achieved by solving the continuity equation for the

volume fraction of one of the phases. For example, in order to solve the volume fraction α_w for the water phase at a water and air interface, the equation is as follows [20, 30]:

$$\frac{\partial(\alpha_w \rho_w)}{\partial t} + \nabla \cdot (\alpha_w \rho_w \vec{v}_w) = \sum_{p=1}^{m} (\dot{m}_{aw} - \dot{m}_{wa}), \tag{2.4}$$

where $\dot{m}_{wa}$ is the mass transfer from water to air, and $\dot{m}_{aw}$ is the mass transfer from air to water. The density and velocity of the water phase are ρ_w and $\vec{v}_w$. When discretizing the continuity equation using the implicit scheme, we get

$$\frac{\alpha_w^{n+1}\rho_w^{n+1} - \alpha_w^n \rho_w^n}{\Delta t} V_{vol} + \sum_f \left(\rho_w^{n+1} U_f^{n+1} \alpha_{w,f}^{n+1}\right) = \left[\sum_{p=1}^{m} \dot{m}_{aw} - \dot{m}_{wa}\right] V_{vol}, \tag{2.5}$$

where the superscript (n+1) and (n) are the index for the new time step and the current time step, respectively. $\alpha_{w,f}^n$ is the face value of the water volume fraction [20, 23], V_{vol} is the volume of the cell, and U_f is the volume flux through the cell face. After solving for the volume fraction of the water phase α_w, the properties for the transport equations are determined by the knowledge of the component phases in each control volume. The density and the viscosity in each cell can be calculated by

$$\rho = \alpha_w \rho_w + (1 - \alpha_w)\rho_a, \text{ and} \tag{2.6}$$

$$\mu = \alpha_w \mu_w + (1 - \alpha_w)\mu_a. \tag{2.7}$$

The new density ρ and viscosity μ are then substituted in the momentum Eqs. (2.2a) and (2.2b) to solve for the flow field properties. As mentioned earlier, the VOF model

requires the use of pressure based solver for incompressible flow, which is one of the two numerical solvers that FLUENT provides [31]. It utilizes a projection method algorithm [20] that decouples the computations of the velocity and pressure fields [32]. The governing equations are non-linear and coupled, and the solution loop is carried out iteratively, as shown in Figure 2.3, in order to obtain a converged numerical result. Each iteration in the pressure-based solver consists of the following steps [20, 31]:

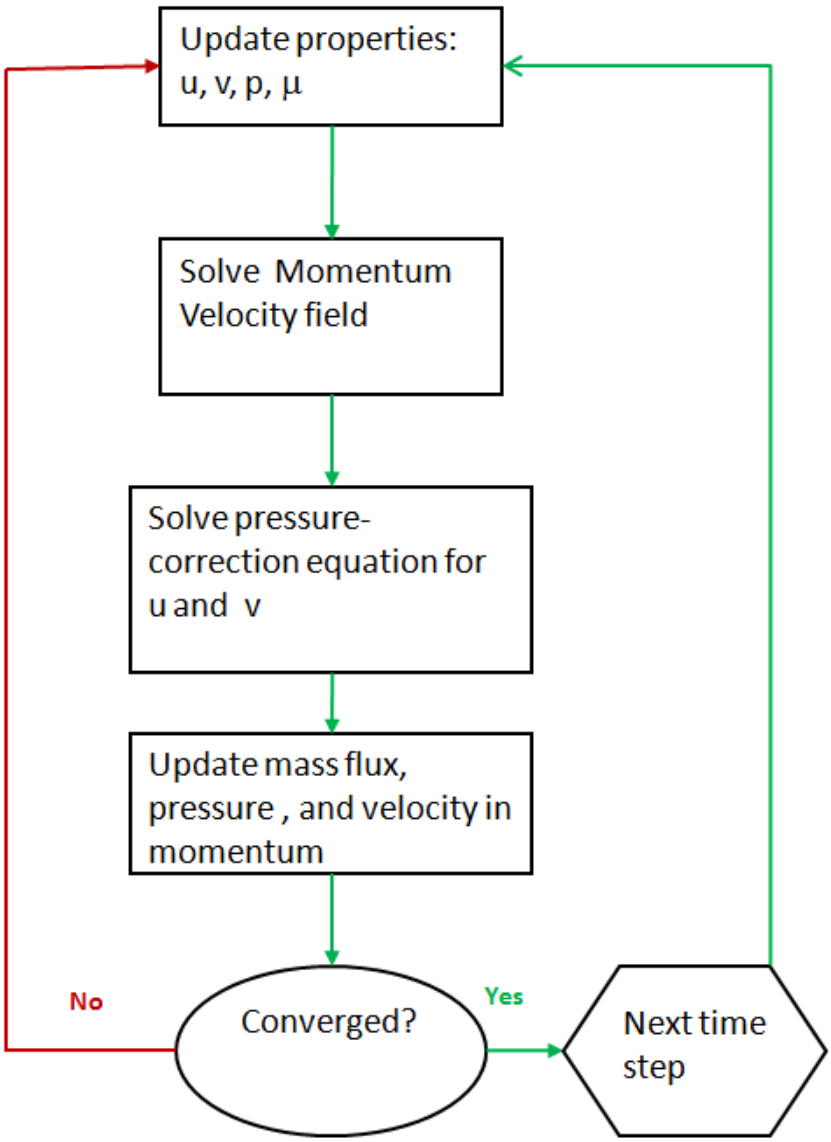

Figure 2.3 Pressure-based solution diagram

1. Fluid properties are updated based on the current or previous time steps.

2. The momentum equations are solved using the recently updated values of pressure and mass flux through the face from equation 2.3.

3. The pressure correction continuity equation is solved using the velocity field found in step two.

4. The mass flux, pressure, and velocity field are updated using the pressure from step 3

5. The convergence of the iterative scheme is checked.

This sequential type algorithm is considered to be efficient when it comes to computer memory. Only the equations that need to be discretized are stored one at a time.

The momentum equations are solved by the implicit method whose numerical stability condition dictates the scheme as unconditionally stable [33]. However, because the selection of a large time step leads to an increase in truncation errors [33], a simulation time step $1x10^{-6}$ seconds is used. The time step is selected to satisfy the absolute convergence criterion of $1x10^{-3}$ for continuity, x and y components of velocity, and volume fraction of the water. Tecplot [34] is used to generate all CFD illustrations for this work.

CHAPTER THREE: STRAIGHT CHANNEL WITH ZERO GRAVITY

The droplet of a two-dimensional, viscous, Newtonian, and incompressible fluid surrounded by the air is studied in a channel where the droplet is suspended. The channel is located in the center of the computational domain, and the channel width and length are 2r and 2L, respectively (see Figure 2.1). R_U and R_L are the upper and lower cap radii of the water drops.

3.1 Mathematical Model

In order to estimate steady-state (or equilibrium) solutions of a droplet in the channel, we first consider a non-gravity case, g=0, where the Young-Laplace equation describes the relationship between the pressure difference across the two droplet caps and the size of the droplet caps [22, 35]. In a dimensional form, it is written as follows:

$$\Delta p = \gamma \left(\frac{1}{R_L} - \frac{1}{R_U}\right), \tag{3.1}$$

where Δp is the pressure difference, p_L-p_U, in a droplet, and γ is the surface tension, which is independent of the curvature R. This relationship suggests that the droplet state will be equilibrated at $\Delta p=0$, which leads to $R_U=R_L$. Thus, we will find the equilibrium flow states that satisfy the condition $R_U=R_L$. The flow state will be described in terms of the center of mass of the droplet, Y, in the y-direction. This parameter is used as a

measure of the asymmetry of a droplet state; when Y=0 the droplet is symmetric. The normalized center of mass is defined as $Y_{cm} = Y/r$. Here, Y_{cm} can be computed by CFD simulations or by an analytical model, assuming that the droplet-air interfaces remain circular arcs. The analytical dimensional expression for the center of mass of the droplet state is derived in the Appendix-A and is written as follows

$$Y = \frac{2}{V_T}[I_L - I_U] + \frac{L}{V_T}(V_L - V_U), \tag{3.2}$$

where all symbols on the right hand side of the above equation are defined in the appendix. Note that these terms depend on θ_U and θ_L in Equation (A-4) (see Figure A-1). For g=0, $R_U = R_L$ condition that is needed to achieve steady-state induces $\theta_U = \theta_L$ or $\theta_U + \theta_L = 2\pi$. When $\theta_U = \theta_L$, $I_U = I_L$ and $V_U = V_L$ which leads to the symmetric state ($Y_{cm} = 0$). On the other hand, when $\theta_U + \theta_L = 2\pi, V_U > V_L$ or $V_U < V_L$, which are asymmetric states. These two cases show that the asymmetric states may be established in two possible ways, which are opposite to each other. Note that when $\theta_U = \theta_L = \pi$, $V_U = V_L = \frac{V_{cr}}{2}$, where $V_{cr} = V_U + V_L = \pi r^2$. For convenience, the normalized total droplet cap volume, V, is defined as

$$V = \frac{V_U + V_L}{V_{cr}} = \frac{V_U + V_L}{\pi r^2}. \tag{3.3}$$

Here, V = 1 at the critical volume. These solutions, based on the above analytical expressions, demonstrate that only the symmetric states exist when $V < 1$. However,

when $V > 1$, steady asymmetric states exist in addition to an unsteady symmetric state see Figure 3.1.

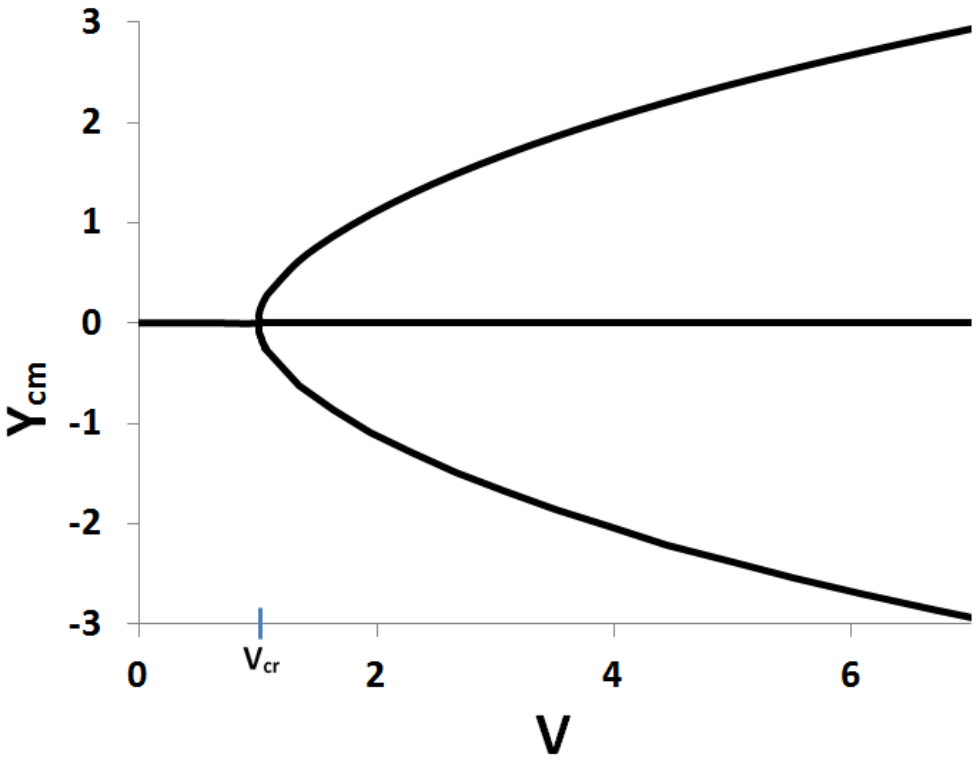

Figure 3.1 Analytical expression of the center of mass Y_{cm} shows a pitchfork bifurcation at V=1.

A numerical approach to evaluating the stability of each droplet state for various droplet sizes is to compute the convergence rate of Hamiltonian, $\overline{H}$, of the systems. The Hamiltonian is defined as the sum of the kinetic energy and the potential energy associated with the system [36]:

$$H = Ke + Pe, \tag{3.4}$$

where the kinetic energy (Ke) and the potential energy (Pe) are defined as:

$$Ke = \frac{1}{2}mv^2, \text{ and } Pe = mah, \tag{3.5}$$

where m, h, v, and a are the droplet mass, the distance between a reference state and the location of the center of mass of the droplet, the velocity, and acceleration of the droplet with respect to the center of mass, respectively.

The Hamiltonian $\bar{H}$ is normalized using the liquid surface tension γ and the channel half width r as follows

$$\bar{H} = \frac{H}{\gamma r^2} \tag{3.6}$$

The time, t, throughout this work is normalized using the liquid density ρ, channel half width r, and the liquid surface tension γ, using this following relation:

$$\bar{t} = \frac{t}{\sqrt{\rho r^2/\gamma}} \tag{3.7}$$

3.2 CFD Model Validation

The sensitivity of the CFD simulations to grid refinement and time step reduction is investigated. The investigation concentrates on V = 0.5. Discussions on the droplet's behavior, in this case, are described in the Results and Discussions section. For the model validation, the droplet state is initially perturbed, the disturbance decays in time, and the droplet returns to a symmetric state. Meshes with 5000, 15000, 25000, 50000, and 100000 nodes are used in the grid refinement analysis. Results of the center of mass of the droplet at the equilibrium states obtained from the simulations using the various meshes are shown in Figure 3.2(a). The figure demonstrates the convergence of

the computed steady-state results with mesh refinement. Note that the ideal location of the center of mass is zero since the equilibrium state of the droplet is a symmetric state for $V \leq 1$. It is found that the meshes with 15000 and 25000 nodes provide sufficient accuracy for the computations when compared with computations using the more refined mesh with 100000 nodes and the coarse mesh with 5000 nodes. The absolute values of the variations of steady-state locations of the center of mass of the droplet from the ideal location are about 0.5 and 0.4% for 15000 and 25000 nodes, respectively.

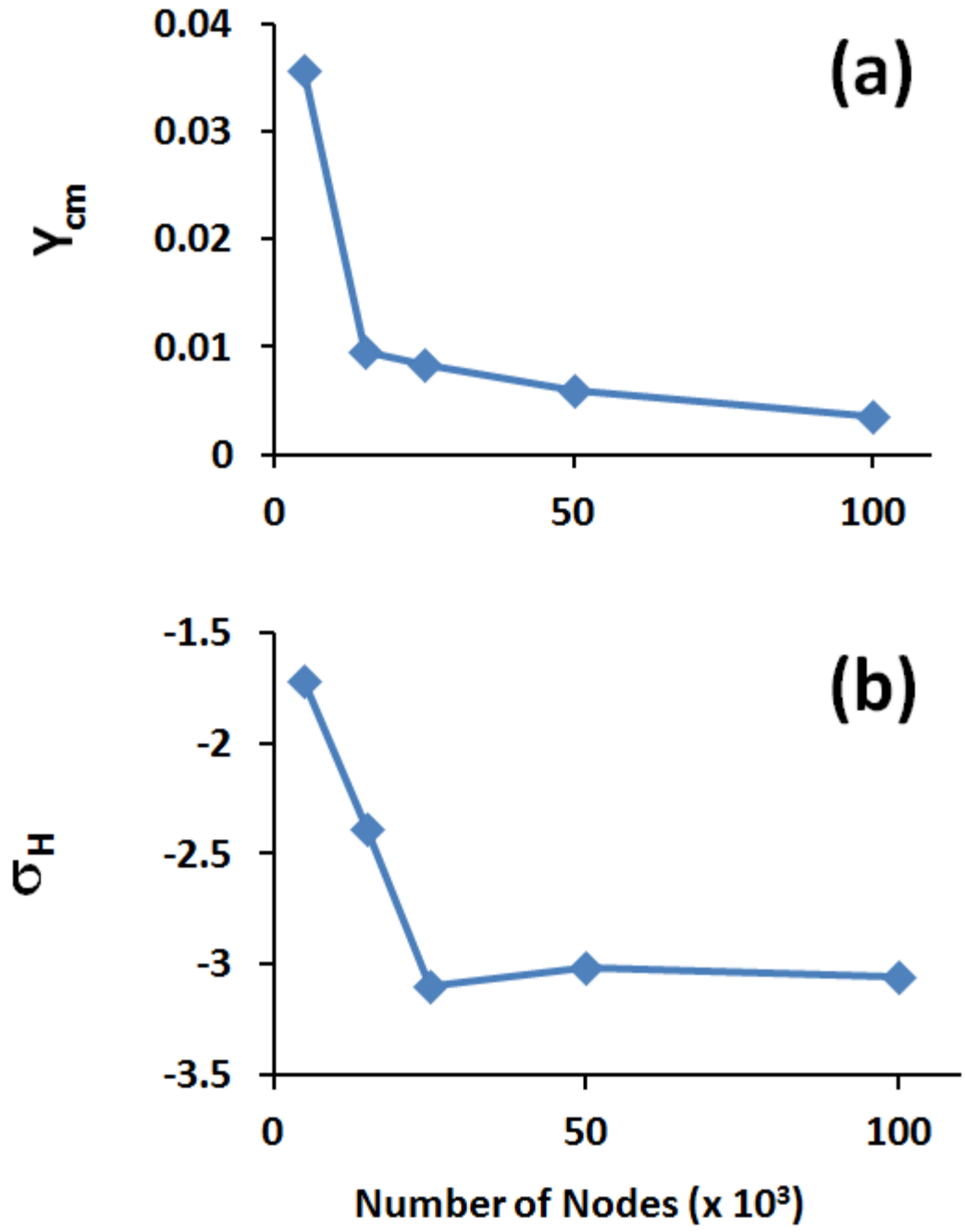

Figure 3.2 (a) Center of mass (normalized) at the equilibrium state with respect to the number of nodes for V=0.5. (b) Decay rate (normalized) with respect to the number of nodes for V=0.5.

Results of the decay rate of time-history plot of Hamiltonian of the system obtained from the CFD simulations based on the dynamics of the center of mass location are also

investigated (see Figure 3.2(b)). The dynamics of a Hamiltonian near a steady-state may decay exponentially [36]. In studying the decay rate of the system, a suitable mode of the following form:

$$\bar{H}_{system} = Ae^{\sigma_H \bar{t}} \tag{3.6}$$

is considered where A is an amplitude of the mode and σ_H is the non-dimensional decay rate of the Hamiltonian. The parameter, σ_H, is evaluated at various times during a run by post processing the fluent results. Details of the discussion of the decay rate obtained from CFD simulations are described in the Results and Discussion section.

The Figure 3.2 demonstrates the convergence of the computed dynamic parameters with mesh refinement. It is found that the mesh with 25000 nodes provides sufficient accuracy for the computations when compared with computations using the more refined mesh with 100000 nodes and the coarse mesh with 15000 nodes. The absolute value of the variations of decay rate compared with the value obtained from 100000 nodes is about 1.5% for 25000 nodes. Numerical results for the above mentioned test cases show sufficient accuracy for the computations with 25000 nodes for both static and dynamic tests when even finer meshes were used. Moreover, the simulation time is about 30% of the time required for the mesh with 100000 nodes. Therefore, we choose to use 25000 nodes in our CFD simulations.

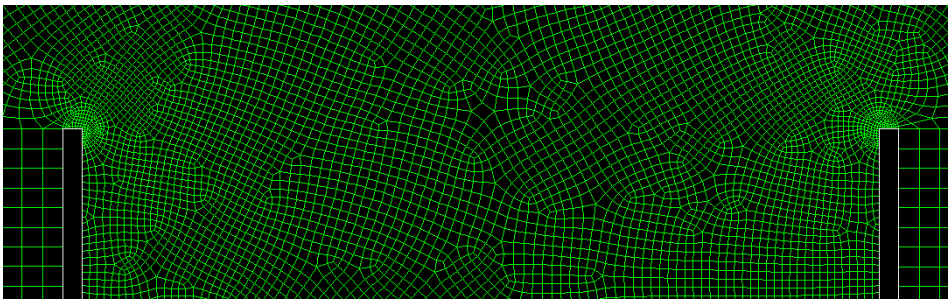

Figure 3.3 Mesh refinements over the corners.

In order to be capable of simulating various droplet sizes, two sizes of the computational domain have been prepared through the use of GAMBIT [20]. A larger domain is for simulations with larger droplet sizes $V > 1.6$, and a smaller domain is for smaller droplets, $V \leq 1.6$. Dimensions, node and cell numbers of both computational domains are summarized in Table 3.1. Figure 3.3 shows a local mesh grid refinement that is introduced near the channel walls and corners to reduce singularities and improve interfacial accuracy.

Table 3.1 Domain properties: Domain 1 for larger droplet volumes, Domain 2 for smaller droplet volumes.

	Dimensions (mm)	Number of Nodes (≈)	Number of Cells (≈)
Domain 1 (large)	15.8 x 9.6	32000	45000
Domain 2 (small/intermediate)	7.8 x 3.7	25000	27000

3.3 Results and discussion:

The dynamics of various drop size cases in a channel for both V < 1 and V > 1 is studied using CFD. In the first case, a V = 0.5 is studied using the smaller domain (Domain 2 in Table 3.1) for computational efficiency. In this case V < 1, and the symmetric state is unconditionally stable to any disturbance. The initial large disturbance, $Y_{cm}(\bar{t}=0)=0.4$ is introduced on the droplet, and the schematic view is shown in Figure 3.4(a). It can be seen that even a large asymmetric disturbance is relatively quickly decayed with an oscillatory motion and dissipated due to the viscosity of the fluids (see Figure 3.4(b)). After approximately $\bar{t}=3$, the droplet returns to a symmetric state and stays there as expected (see Figure 3.4(c)). Similar droplet dynamics were observed with any other disturbance sizes of V<1. However, the simulation time taking the disturbance to decay becomes longer by increasing the initial disturbance size and shorter when decreasing the drop sizes. These phenomena have been observed in the analytical and experimental studies mainly by Theisen et al [8]and Hirsa et al [5].

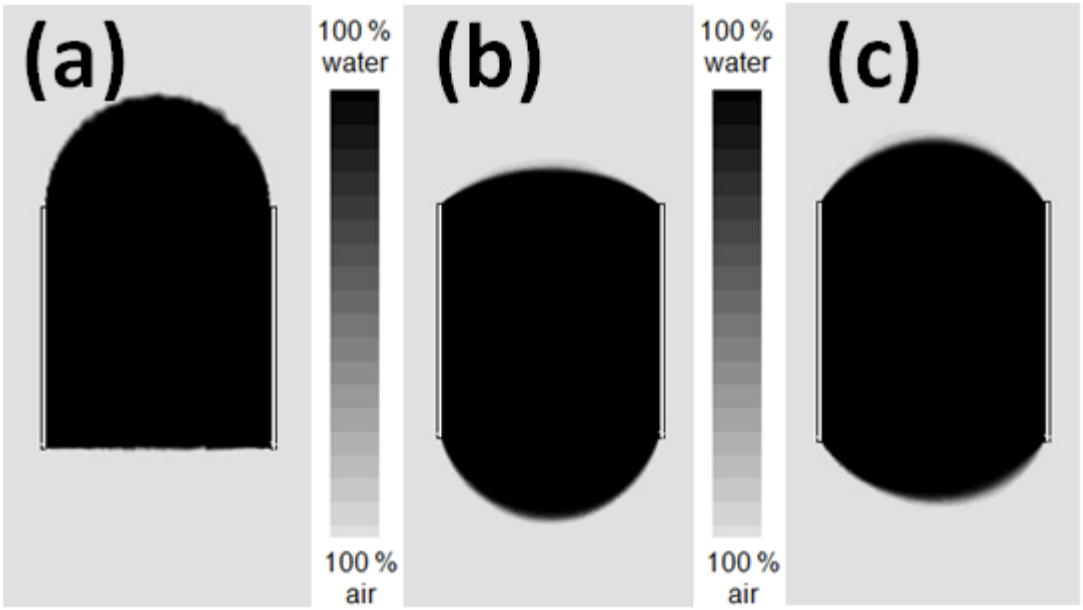

Figure 3.4 Droplet states at V=0.5 (a) Initial state at $\bar{t}$=0, (b) Intermediate state at $\bar{t}$=1, (c) Final state at $\bar{t}$=3.

Figure 3.5(a) shows a time-history plot of the center of mass of the droplet for V =0.5. The disturbed symmetric droplet state for $Y_{cm}(\bar{t}=0)$= 0.4 is used as the initial condition. The time-history plot shows a damped oscillatory motion with exponentially decaying amplitude. The oscillatory amplitude is large at the beginning depending on the size of initial disturbance, and the oscillatory motion is damped due to the viscous dissipation in the fluid, and the droplet returns to a symmetric state in time.

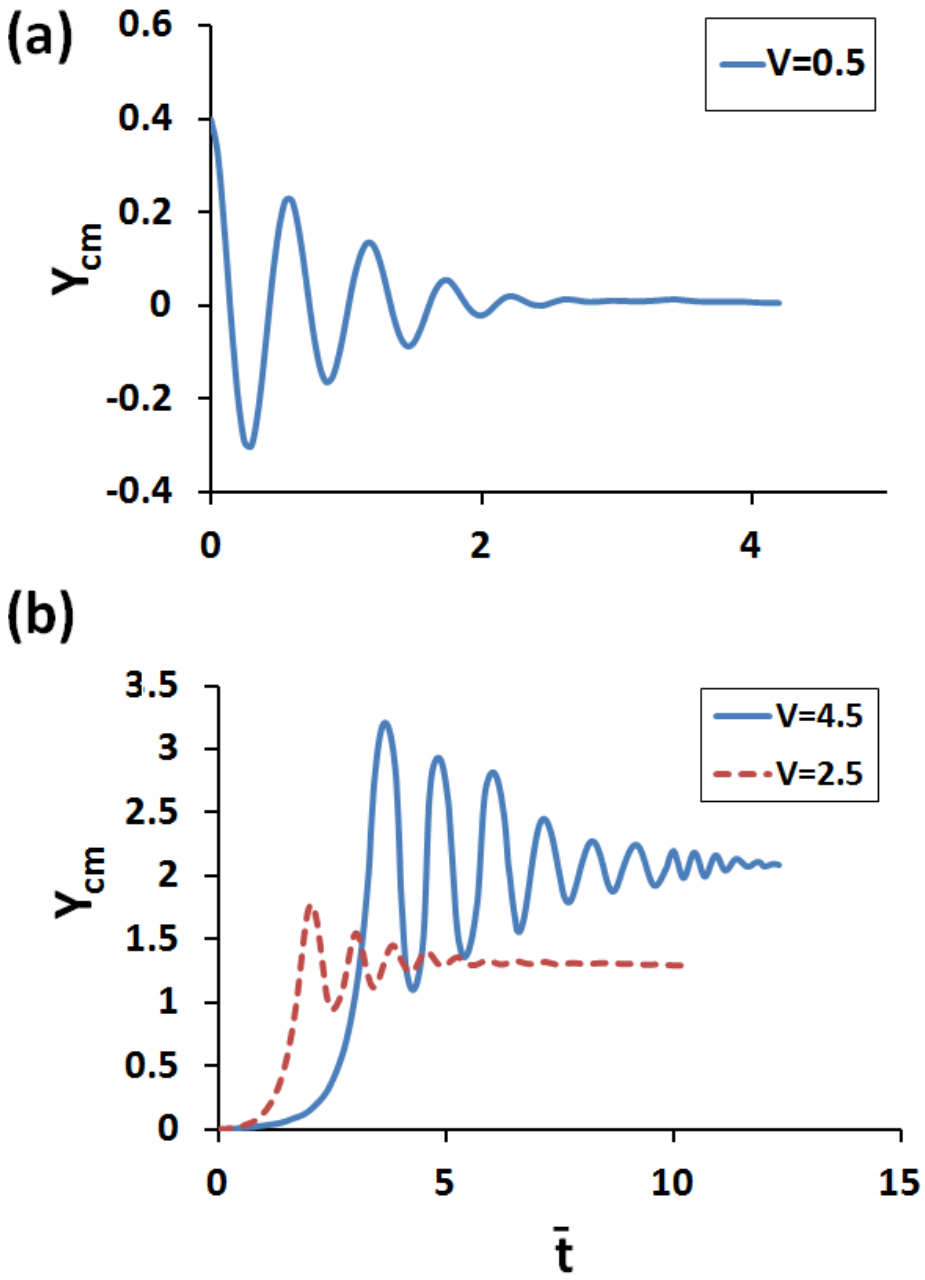

Figure 3.5 (a) Temporal change of center of mass at V=0.5. (b)Temporal change of center of mass at V=2.5 and V =4.5.

To demonstrate the convergence to a symmetric state at V = 0.5, the time history plots of a Hamiltonian of the system are presented in Figure 3.6(a). It can be seen that for the two cases of initial disturbances, $Y_{cm}(\bar{t}=0)$=0.4 and 0.2, at V = 0.5 the dynamics

of the disturbance are similar: after a nonlinear transient and when the disturbance becomes sufficiently small, $\overline{H}$ decays exponentially, $\overline{H} = Ae^{\sigma_H \bar{t}}$, and with almost the same rate of decay ($\sigma_H = -3.14$) for both values of initial Y_{cm}.

Also shown in Figure 3.6(b) are time-history plots of the H for V=0.5 and 0.95. The comparison between $\sigma_H = -3.14$ for $V = 0.5$ and $\sigma_H = -2.39$ for $V = 0.95$ shows that the decay rate of a disturbance decreases as V increases toward the critical value and the flow loses its stability characteristics.

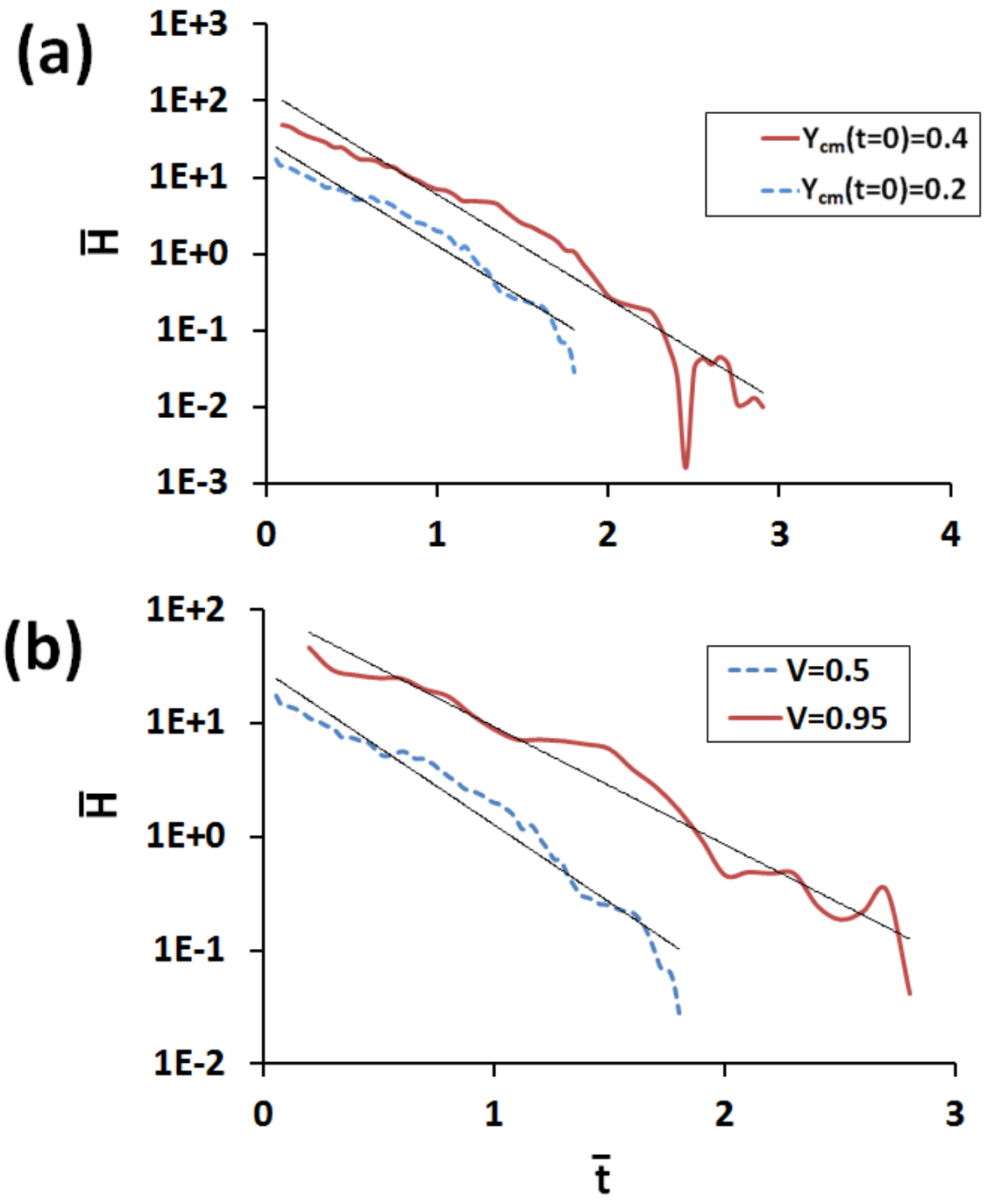

Figure 3.6 (a) The time history plots of the Hamiltonian at V=0.5 with initial disturbances $Y_{cm}(\bar{t}=0)=0.4$ and $Y_{cm}(\bar{t}=0)=0.2$ (b) The time history plot of the Hamiltonian at V=0.5 and V=0.95 with an initial disturbance $Y_{cm}(\bar{t}=0)=0.2$.

Now, cases with the droplet V>1 are studied. For V>1, both smaller and larger domains are used for 1<V≤1.6 and V>1.6, respectively. The initially symmetric droplet state for V=1.4 at $Y_{cm}(\bar{t}=0)=0$ is illustrated in Figure 3.7(a). The liquid droplet slowly transit to asymmetric state (Figure 3.7(b)), and after approximately $\bar{t}=6$ the droplet reaches to a stable asymmetric state (see Figure 3.7(c)). Similar dynamics were also observed at any other V > 1. However, the simulation time taking the disturbance to decay becomes shorter as increasing the initial disturbance size and longer as increasing the drop size. These transition phenomena have been also observed in the analytical and experimental studies by Theisen et al [8] and Hirsa et al [5].

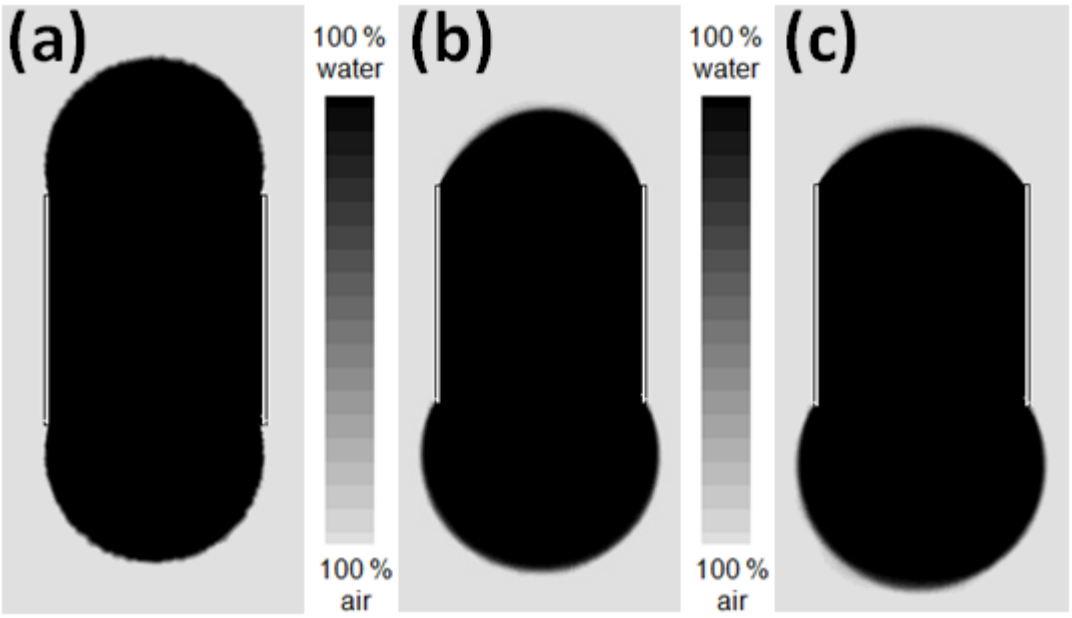

Figure 3.7 Droplet states at V=1.4 (a) Initial state at $\bar{t}=0$, (b) Intermediate state at $\bar{t}=1.6$ (c) Final state at $\bar{t}=6$

Figure 3.5(b) shows a time-history plot of the center of mass of another two droplet cases of V =2.5 and 4.5. The initial condition is symmetric state ($Y_{cm}=0$), the numerical

inaccuracy and round-off errors generate a very small asymmetric droplet disturbance for both cases. The time-history plots show the relatively small asymmetric disturbances that grow slowly in time and evolve in a nonlinear oscillation process. This oscillatory motion is damped due to the viscous dissipation in the flow, and the droplets for both cases reach steady asymmetric states. According to the figure the amplitudes of oscillatory motions are larger for larger V which affect a difference in the time it takes to damp the oscillatory motions to the steady asymmetric states. We also observe that the growth of the initial transition processes is faster for V=2.5 than that for V=4.5 which affects a difference in the time it takes to the asymmetric states. More discussions regarding the initial growth rate will be described based on the growth rates of Hamiltonian.

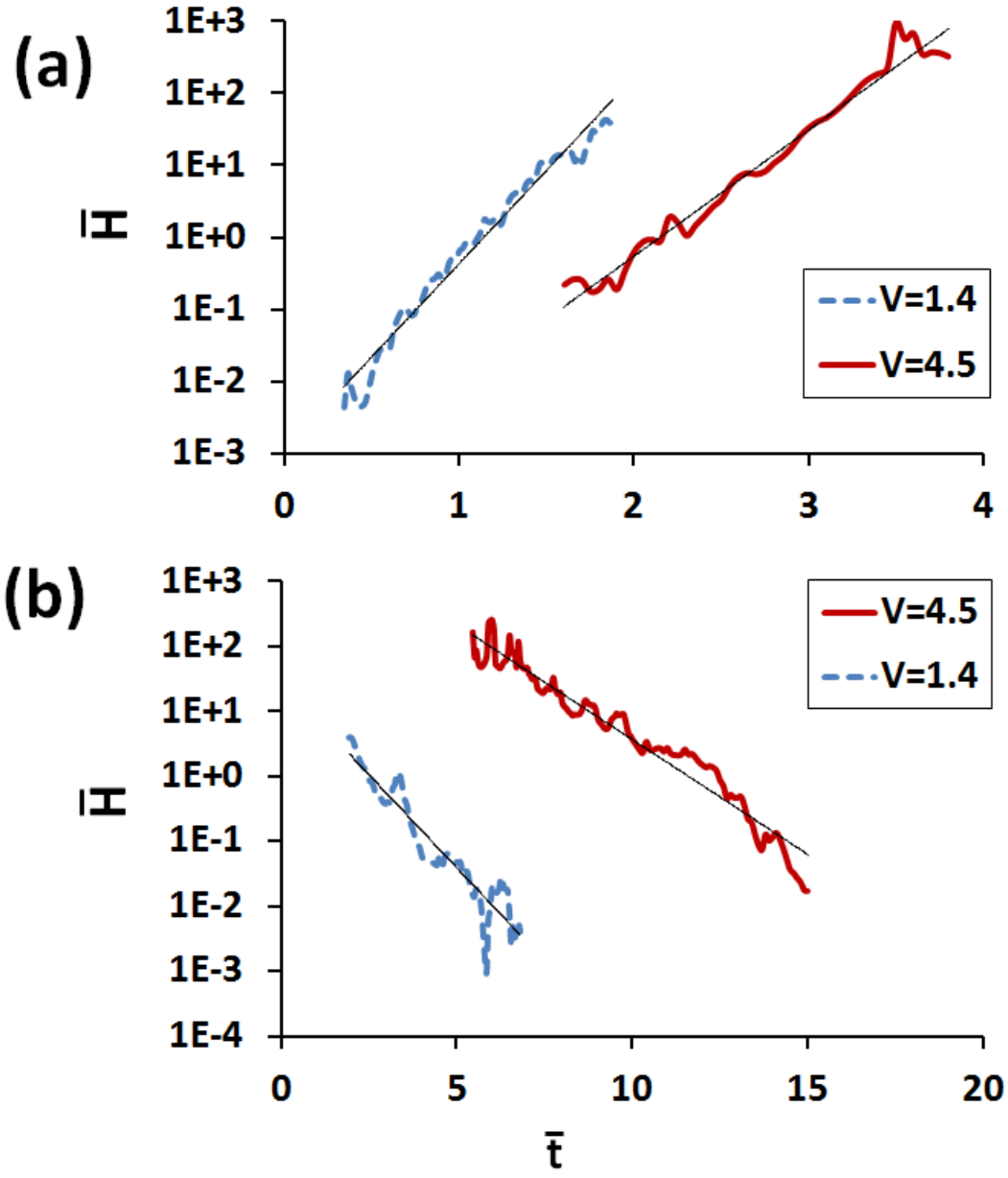

Figure 3.8 (a) The time history plot of the Hamiltonian at V=1.4 and 4.5. (b) The time history plot of the Hamiltonian at V=1.4 and 4.5.

The time history plots of a Hamiltonian for V>1 are shown in Figure 3.8(a) and Figure 3.8(b). Figure 3.8(a) describes the early growth rate of two droplet volumes V=1.4 and V=4.5 from symmetric states, and they are $\sigma_H = 5.87$ for $V = 1.4$ and $\sigma_H = 4.04$ for $V = 4.5$. For 0<V<1.8 We have observed that the growth rate becomes

larger with droplet size. The nonlinear effects become important as V increases above 1.6. Then the growth rate reaches a maximum at V = 1.8 ($\sigma_H = 6.48$) and decreases for higher values of V. It is also observed that the growth of the Hamiltonian at V=4.5 starts to appear at a later time, around $\bar{t}$=1.6. This is due to the time it takes for large droplets to create instability out of numerical errors in the symmetric solution and the slow reaction of the larger mass of the droplet.

The decay rates of Hamiltonian, $\bar{H}$, for the same two droplet volumes, V=1.4 and 4.5 are shown in Figure 3.8(b). They are $\sigma_H = -1.32$ and -0.82 for $V = 1.4$ and 4.5, respectively. We found that the decay rate becomes smaller as the volume size, V, increases. Then, the decay rate reaches a minimum at V_{min} =1.8 ($\sigma_H = -2.01$) and increases for higher V.

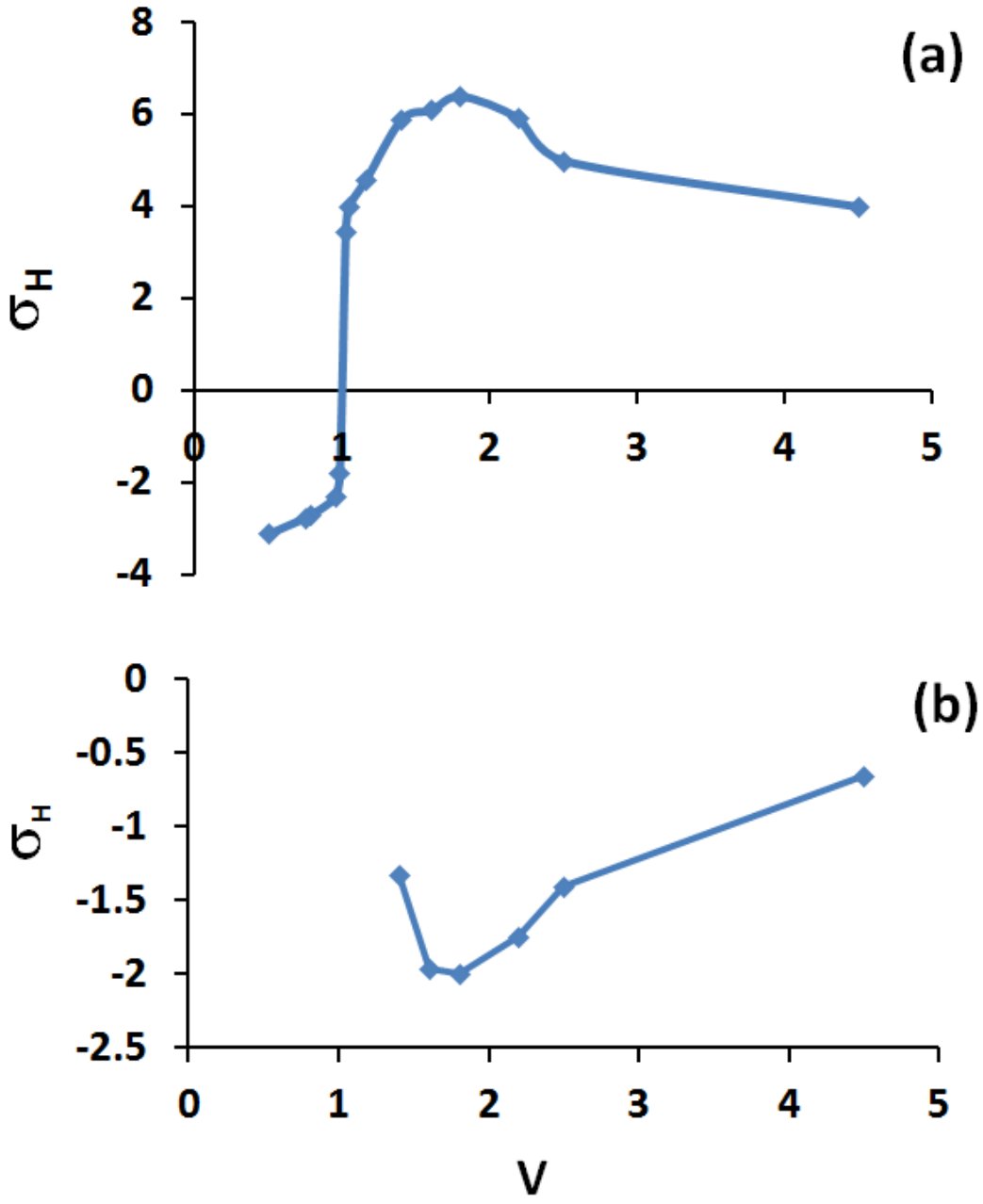

Figure 3.9 Stability characteristics of (a) the symmetric and (b) asymmetric states as functions of V.

The results of the growth and decay rates for various other droplet sizes are summarized in Figure 3.9(a) and (b). In Figure 3.9(a), it is found that σ_H for symmetric states grows monotonically with V, up to V=1.8. Moreover, $\sigma_H < 0$ when V<1 and

$\sigma_H > 0$ when V>1. The parameter σ_H has a maximum at V=1.8 and is less for higher values of V. This is due to the slow reaction of the larger mass of the droplet. It is found that σ_H is positive in the range 1<V<13. Note that when V=13, the droplet cap volumes become too large for the droplet surface tension to sustain their shapes. Thus, there is a collapse of the larger cap of the droplet. However, such large V cases are beyond the scope of this work.

Figure 3.9(b) shows that σ_H for asymmetric states is negative for all V>1. The σ_H decays monotonically with V, reaches a maximum decay rate at V=1.8, and becomes less for higher values of V. For V > 1.8 we observed that the time taking to complete the transition process becomes longer as V increases because both the growth rates from the symmetric states and the decay rates to the asymmetric states become slower.

The pitchfork bifurcation diagram obtained from the analytical model in Equation (3.2) is described as solid lines in Figure 3.10. It shows that the droplets have steady symmetric solutions for all V<1, and steady asymmetric solution for V>1. There also exists a V_{cr} (equals πr^2) of the droplet where asymmetric states suddenly bifurcate from the branch of symmetric states.

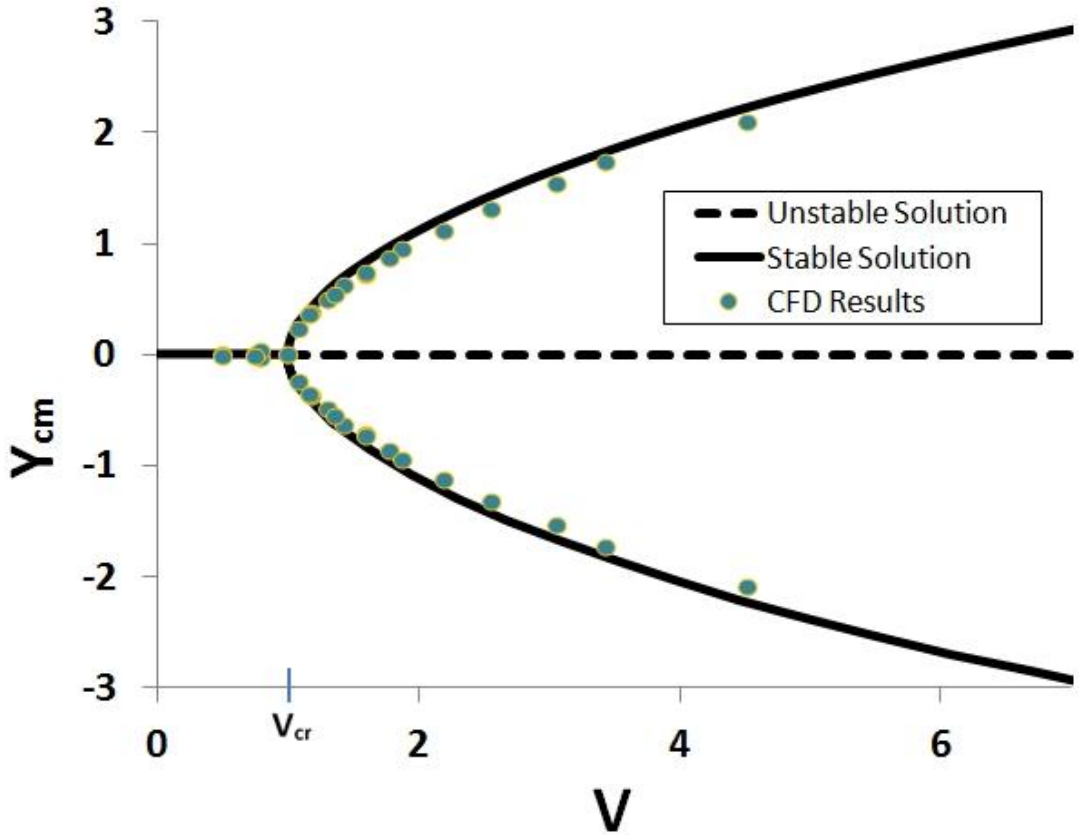

Figure 3.10 Comparison of the normalized center of mass obtained from the analytical expression with the simulation results.

The transition phenomena observed by CFD simulations can be explained by the Young-Laplace equation (3.1). A Large radius of curvature will result in a lower pressure across the droplet, and a lower radius of curvature will result in a higher pressure, while the interfacial tension stays constant. In the first case V<1, the droplet is initially in a symmetric state (R_U=R_L). When the droplet state is slightly disturbed (see Figure 3.11(a)), the droplet state becomes slightly asymmetric, and the upper radius of curvature R'_U becomes shorter than that of the lower R'_L. According to the Young's Laplace relationship, the pressure at the upper cap becomes higher than the one at the lower, and this pressure difference induces a driving force to move back the droplet to the initial symmetric state.

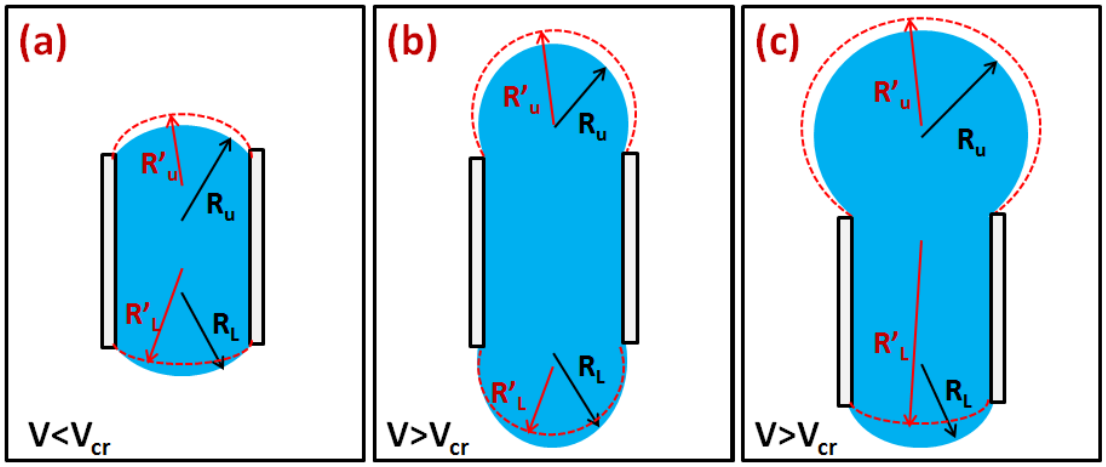

Figure 3.11 A symmetric droplet at state (blue) and a slightly perturbed state (red dashed lines) for (a) V<1, (b) V>1, (c) An asymmetric droplet state (blue) and a slightly perturbed state (red dashed lines) for V>1

In the second case we consider that the droplet is initially symmetric (R_U=R_L) and that the cap volume is greater than the critical volume V>1 (see Figure 3.11(b)). Then, the droplet state is disturbed and becomes slightly asymmetric such that the upper radius of curvature R'_U becomes longer than the lower one R'_L. Based on the Young's Laplace relationship, the pressure at the lower cap becomes higher than the one at the upper, and this pressure difference induces a driving force to move the droplet to upper side that leads the droplet to become more asymmetry.

Finally, we consider that the droplet is in a steady asymmetric state, R_U=R_L (see Figure 3.11(c)) and that the cap volume is greater than the critical volume V>1. When the droplet is slightly disturbed and becomes more asymmetric, the upper radius of curvature R'_U becomes shorter than the lower one R'_L. This leads that the pressure at the upper cap becomes higher than the one at the lower, and this pressure difference induces a driving force to move back the droplet to the steady asymmetric state.

Therefore, the droplets do not escape from the channel in the range of droplet volumes we have simulated.

From the above discussions, we found that when V<1 the symmetric state is found to be the only solution of the problem. However, when V>1 the symmetric state becomes unstable (described as a dashed line in Figure 3.10) and the two asymmetric states become the stable solutions. This discussion is verified by the CFD simulation results in Figure 3.10. It shows an excellent agreement between the analytical solutions and simulation results, especially near the critical volume. As V is increased above 3, the droplet asymmetry predicted by the analytical model becomes slightly larger than those found in the numerical simulations (within less than 2% deviation). The reason for the deviation might be related to the assumption of the circular shape of the droplet cap in the model. It is more difficult for the droplet cap to maintain its circular shape as V is increased.

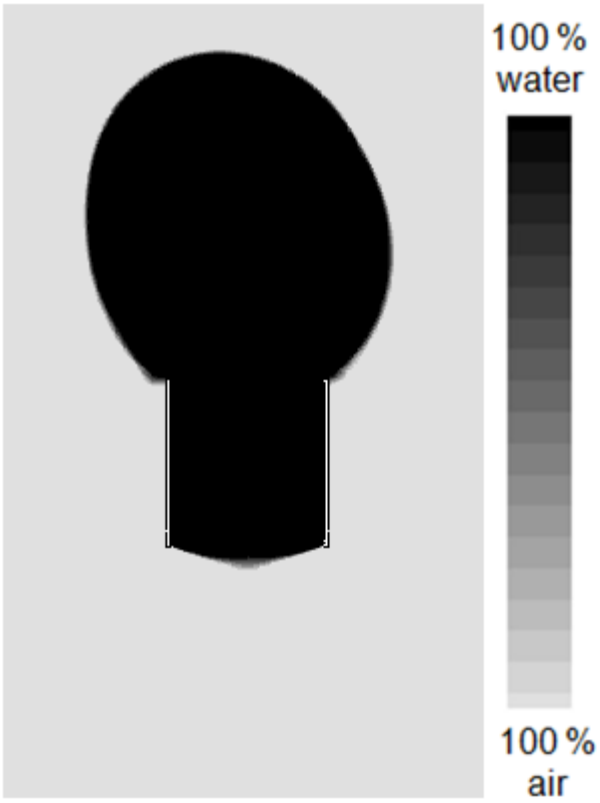

Figure 3.12 Extreme lateral tilting in droplet shape at a large droplet volume (V=4.5, $\bar{t}$=8.5)

In a few simulations, we noticed that as the droplet reaches the steady state the droplet interface thickness (which is the transition region between liquid and air phases) starts to become asymmetric like the one that is shown in the right side of the lower cap of the droplet in Figure 3.4(c) and the left side of the lower cap of the droplet in Figure 3.7(c). In addition, there are also a few cases where a tilting of droplet in a lateral direction is observed, such as the one shown in upper droplet cap in Figure 3.4 (b) and a more extreme tilting case is shown in Figure 3.12. The reasons behind these observations are, first, the asymmetric nature of the mesh used for these simulations, and second, the parallel algorithm that FLUENT uses to divide the domain in order to perform the iteration [20]. When the mesh is asymmetric, the location of nodes are not

equal between the centerline of the droplet body, and that leads to different error generation along the two sides of the droplet centerline. When parallel processing is used, every processor does the iterating task differently due to the difference in truncation and round-off of data output in each processor. This leads to a different error accumulation and residual results between processors [37]. Consequently, there is a slight asymmetry that will grow as the simulation time increases. Also, according to reference [38] the presence of simulation noise that comes from the numerical scheme, errors from numerical round-off, and small differences in tessellation, which is the creation of 2D mesh using a repetition of geometrical shape with no overlapping and no gaps, cause the simulation models that are in fact symmetric to lack perfect symmetry. Figure 3.13 shows that when a symmetric mesh is used the problem with the interface-thickness asymmetry is eliminated. However, Figure 3.14(a) shows that when the symmetric mesh is used with parallel processing, the lateral movement of the droplet still clearly appears. This problem is eliminated when the same symmetric mesh is used with a single processor (Figure 3.14(b)). The simulation time using a single processor with a symmetric mesh takes a tremendous amount of time, at least a week. Therefore, parallel processing with local refinement is used throughout this work. The observed asymmetric cases may have a small effect on the droplet dynamics, but it was observed that it has no significant effect on the droplet final state (as shown on Figure 3.15), and the droplet final state is what is needed for this research work.

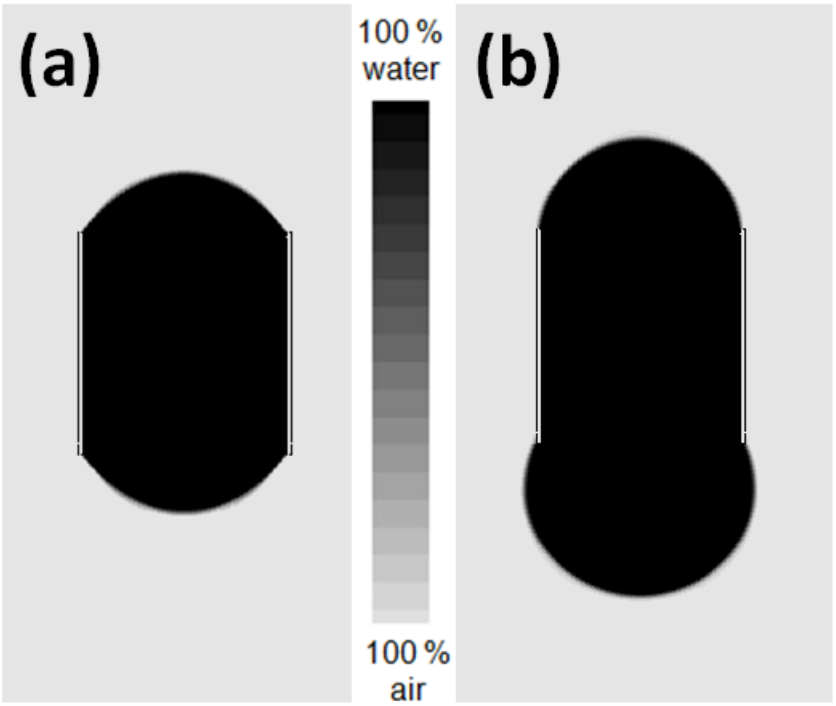

Figure 3.13 The final states of (a) V=0.5 and (b) V=1.4, (illustrated initially in Figures 3.4(c) and 3.7(c)) show interface symmetry when a symmetric mesh is used.

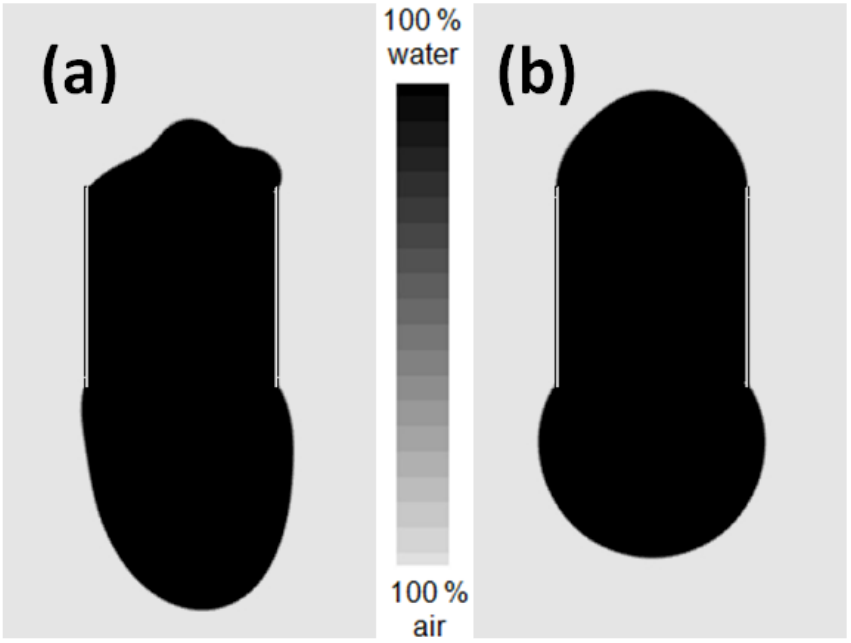

Figure 3.14 Droplet state at $\bar{t}$=3.15 for V=1.7 (and β=0.106, which will be discussed later in Chapter 5) using a symmetric mesh with (a) parallel processing, and (b) single processing.

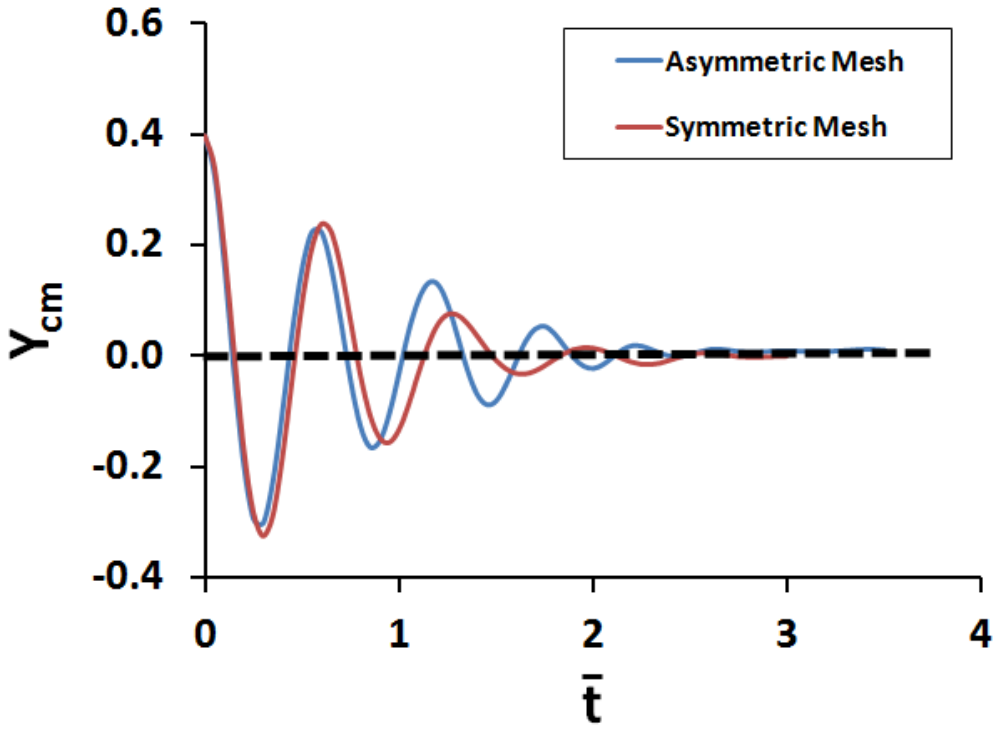

Figure 3.15 Temporal change of center of mass for V=0.5 for both symmetric and asymmetric mesh, showing that the final state for both cases is the same.

CHAPTER FOUR: CONTRACTING CHANNEL WITH ZERO GRAVITY

The symmetry-breaking state at the critical volume, V_{cr}, is expected to be a structurally unstable state, i.e., it is expected that the presence of even a slight degree of asymmetry in the experimental apparatus or in the numerical schemes changes the pitchfork bifurcation diagram into two separate branches of flow states. The theoretical studies of Slobozhanin et al demonstrate that the pitchfork bifurcation is sensitive to imperfections of geometry. This chapter provides the analysis of the effects of slight contraction of the channel geometry on the droplet behavior.

4.1 Mathematical Model

A droplet of a two-dimensional, viscous, Newtonian and incompressible fluid suspended from a contracted 2-D channel is investigated. Similar to the straight one, the channel is located in the center of the computational domain, and its width is $2r_u$ on the upper side of the channel, and $2r_L$ on the lower side of the channel. The length of the channel is 2L. R_U and R_L are the upper and lower cap radii of water drop curvatures, respectively. A contracting channel with the contraction ratio, ε, where $\varepsilon = \frac{r_U - r_L}{r_U}$, is considered (see Figure 4.1).

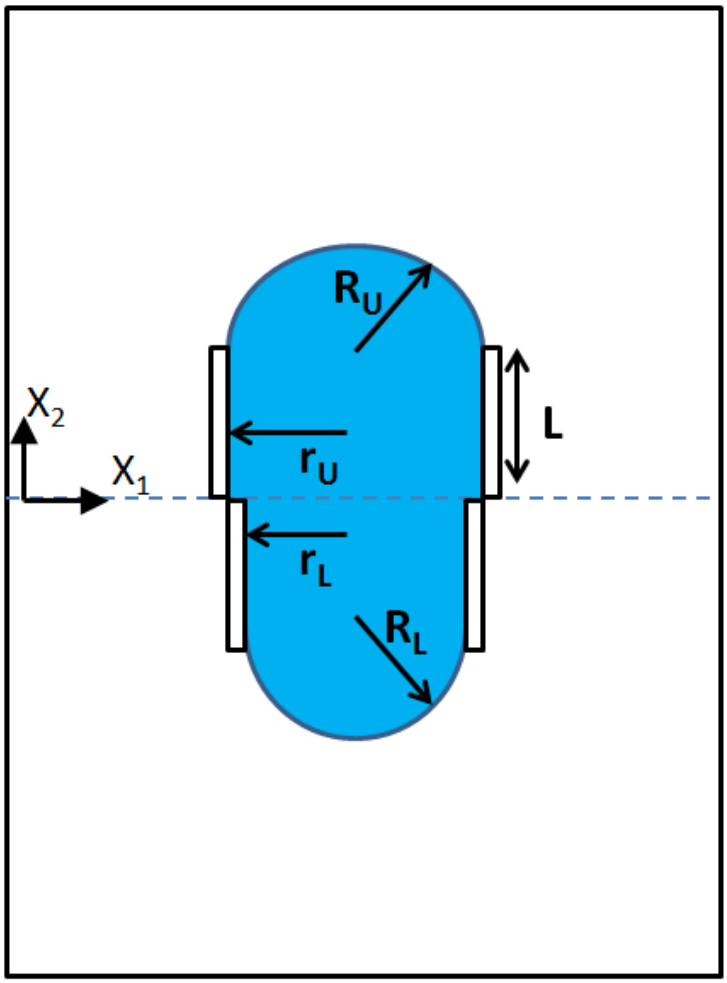

Figure 4.1 Contracting channel

The steady state solution of the contracted channel droplet is calculated from the capillary force using the Young-Laplace equation. Starting by writing the capillary force equation

$$F_\gamma = 2(r_U p_L - r_L p_U). \tag{4.1}$$

Rewriting the Equation 4.1 in terms of the Young-Laplace relationship

$$F_\gamma = 2\gamma\left(r_U\frac{1}{R_L} - r_L\frac{1}{R_U}\right). \quad (4.2)$$

At equilibrium, the right hand side of equation 4.2 is equal to zero

$$2\gamma\left(r_U\frac{1}{R_L} - r_L\frac{1}{R_U}\right) = 0, \quad (4.3)$$

and after rearranging we get the relation between R_U and R_L as follows:

$$R_U = \frac{r_L}{r_U}R_L. \quad (4.4)$$

In terms of the contraction ratio ε equation 4.4 is written as

$$R_U = (1-\varepsilon)R_L. \quad (4.5)$$

For the contracting channel, the same procedure as of that in the straight channel is used, where the relation between R_L and R_U is used to find the droplet state using the center of mass equation Y found from Appendix B

$$Y = \frac{2}{V_T}(I_U - I_L) + \frac{L}{V_T}(V_U - V_L) + \frac{L}{2V_T}(V_{0U} - V_{0L}). \quad (4.6)$$

The center of mass in Equation 4.6 is normalized with the upper channel width, r_U, which is kept fixed for all the contraction run cases. That is $Y_{cm}=Y/r_U$. The center of mass dependence of the droplet volume is discussed in the next section.

4.2 Results and discussion:

The analytical expression to compute the center of mass of the droplet at the steady state is studied here. The details of the derivation of the model are in Appendix B. The model shows that for any contraction ratio $\varepsilon > 0$, the bifurcation diagram deviate from its pitchfork nature for the straight channel case into two separate branches, a primary and a secondary branch. Note that when $\varepsilon < 0$, the channel is contracted in an opposite direction.

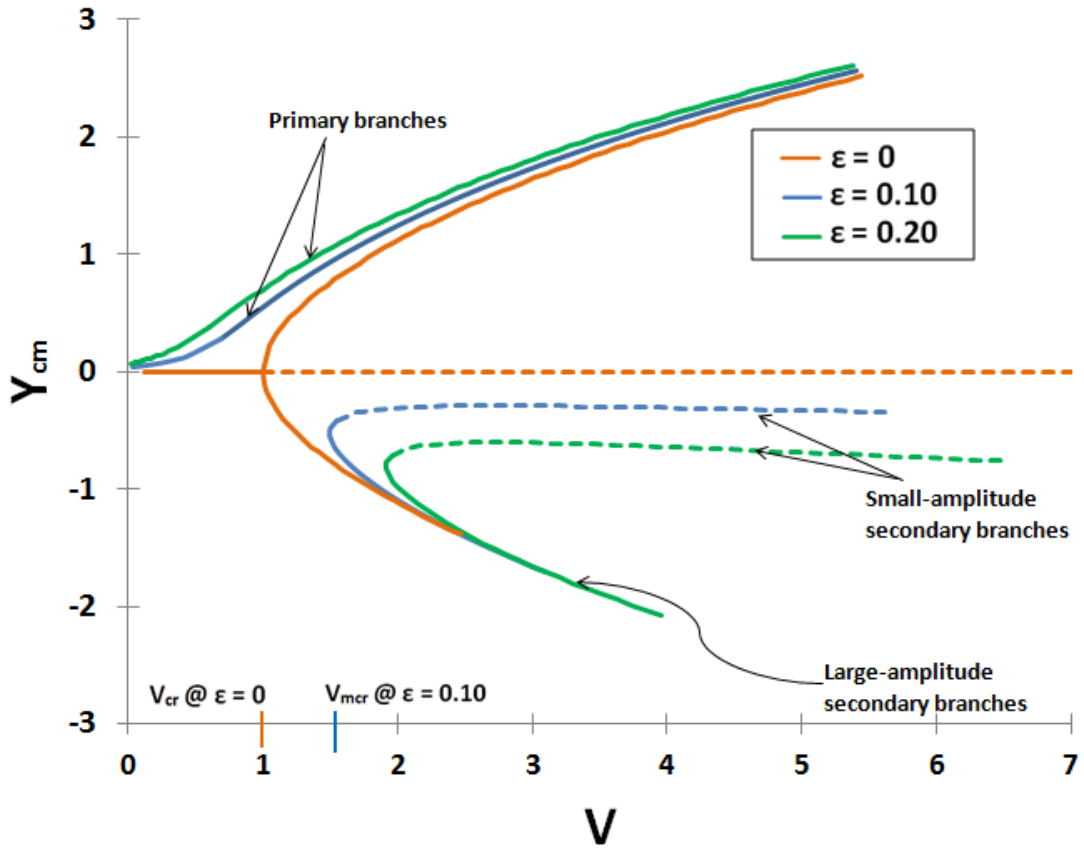

Figure 4.2 Analytical solutions for $\varepsilon = 0$, 0.10 and 0.20.

Figure 4.2 shows three analytical solutions for three contracting channel cases; $\varepsilon = 0,\ 0.10$, and 0.20. From the figure we see the case for the straight channel, $\varepsilon=0$, which was discussed in Chapter 3. It was observed in that chapter that the symmetric state for $V>V_{cr}$ is the unstable state, and the asymmetric state is stable. As the contracting ratio increases above zero, $\varepsilon=0.10$ and 0.20, we see that the critical volume V_{cr} is shifted to the right to become a modified critical volume V_{mcr}, and separate branches start to appear; a primary and secondary branch. The derivative of the center of mass Y_{cm} with respect to the cap volume at the modified critical volume V_{mcr} is equal to infinity, $dY_{cm}/dV = \infty$. The primary branch shows a smooth transition from a small-amplitude of a nearly symmetric state to a large-amplitude asymmetric state. When droplet cap volume is close to zero, $V\approx0$, the location of the center of mass Y_{cm} gets a little larger as the contraction ratio ε increases. The reason for this non-zero value is that the calculation of the center of mass, when V is near zero, considers only the volume of the droplet inside the contracted channel, which is slightly asymmetric depending on ε. On the other hand, when the droplet cap volume is large, $V>>1$, the location of center of mass becomes similar to that of the straight channel, because as the cap-volumes get much larger, the volumes inside the channel become negligible. In Figure 4.2, we also noticed that the transition of the primary branch near the critical volume, $V_{cr,}$ becomes smoother as ε gets larger. The secondary branch, in the other hand, consists of two droplet states; small and large-amplitude states that bifurcate from the modified critical volume V_{mcr}, where the value of V_{mcr} is larger than V_{cr}. As the contraction ratio ε increases, the modified critical volume, V_{mcr}, is increased. When droplet volume

increases, the center of mass location at the large-amplitude branch becomes similar to that of the straight channel, the reason for this is because when the droplet cap volume becomes significantly large, the volume of the liquid within the contracted channel becomes negligible, and therefore it becomes similar to that of the straight channel of ε=0. However, this similarity becomes untrue as the droplet cap volume, V, reaches the modified critical volume, V_{mcr}. For the small-amplitude branch, it is noticed that it deviates further from the symmetry line as the droplet total cap volumes, V, increase. This deviation rate with respect to the droplet cap volumes increases as the contraction ratio ε becomes larger. The reason for this deviation is that when ε becomes large, the balance in the radius of curvature of equation 4.3 will be valid only when one of the droplet caps appears mostly on one side of the channel. The capillary equilibrium at Equation 4.2 will also be valid at that location.

In order to verify the analytical solution and determine the unstable state, three CFD cases of ε=0.20 are used at two different volumes and three different settings. The first case has a droplet volume of V=1.6 and an initial center of mass of $Y_{cm}(\bar{t}=0)=-1.22$ (Figure 4.3(a)). At that location, the upper radius of curvature is infinite and the lower one is finite. According to Equation 4.2, the resultant upward force will be only from the bottom cap droplet. In Figure 4.2 we see that V=1.6 is below the modified critical volume for ε=0.20, therefore, there exist only one asymmetric solution at the primary branch at $Y_{cm}=1.14$. In Figure 4.3 (b) we see a transition of the droplet from lower asymmetric state to the upper asymmetric state at $\bar{t}=1.1$. Figure 4.3 (c) shows the final steady-state of the droplet at the primary branch, and it is located at a center of mass of $Y_{cm}=1.13$ at $\bar{t}=4$. The analytical result is in a good agreement with the CFD result. This

result shows that the equilibrium state at the primary branch is a stable state and that there is no equilibrium droplet state at $Y_{cm} < 0$.

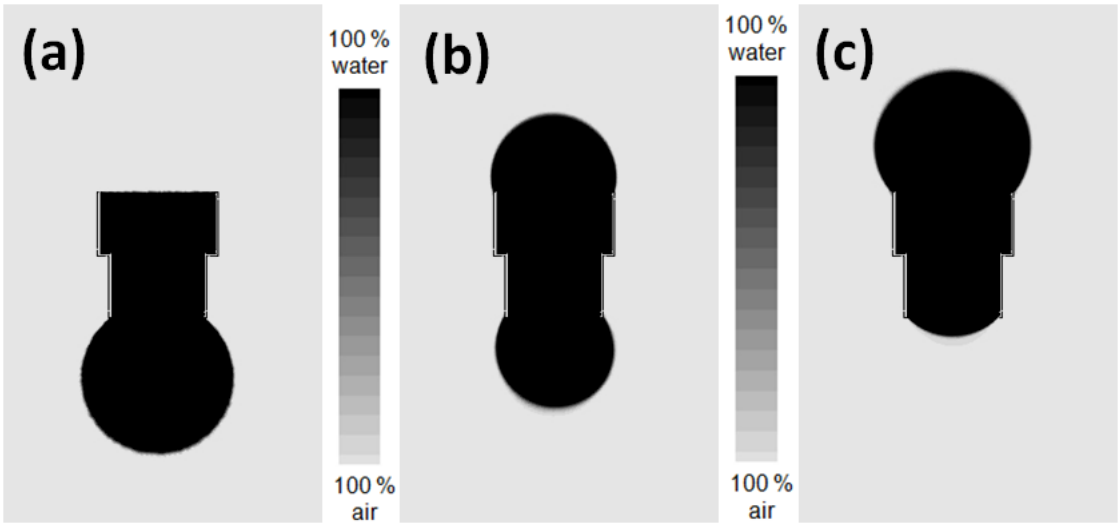

Figure 4.3 Droplet states for $\varepsilon = 0.20$ at V=1.6 with V_{mcr}=1.9 a) Initial state at $\bar{t}$=0, (b) Intermediate state at $\bar{t}$=1.1, (c) Equilibrium state at $\bar{t}$=4.

The second case is for V=2.5 and the center of mass is at $Y_{cm}(\bar{t}=0)$=-0.55, which is slightly below the low-amplitude secondary branch (see Figure 4.4(a)). According to the stability diagram in Figure 4.2, that center of mass location is just below the analytical small-amplitude line of the secondary branch, where the analytical center of mass location for that droplet volume is Y_{cm}=-0.60. Therefore, at that location the radius of curvatures are not in equilibrium as in Equation 4.4. According to Equation 4.2, this non-equilibrium force balance implies that the upper capillary force is larger than the lower one. Therefore, the difference in capillary forces shifts the droplets to the lower direction, where it will eventually reaches equilibrium steady state. Figure 4.4 (b) shows the transition of the droplet from its unsteady location at $\bar{t}$=1.9 toward its stable

steady-state location in Figure 4.4 (c) at Y_{cm}=-1.48 and $\bar{t}$=4. From the analytical results, the droplet's center of mass anticipated final location is on the large-amplitude asymmetric line of the secondary branch, where the final equilibrium state is at Y_{cm}=-1.41. The CFD result showed a good agreement with the analytical one. These results show that the small-amplitude state may be the unstable state, and the large-amplitude state is the stable state.

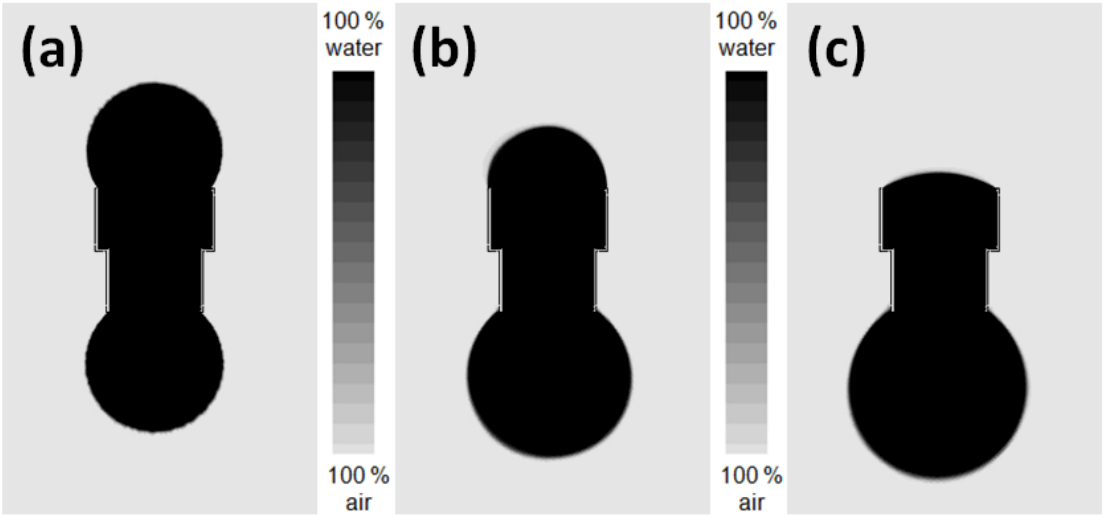

Figure 4.4 Droplet states for $\varepsilon = 0.20$ at V=2.5 with V_{mcr}=1.9 a) Initial state at $\bar{t}$=0, (b) Intermediate state at $\bar{t}$=1.9, (c) Equilibrium state at $\bar{t}$=4.

The final case is for the same volume as the second case, but with an initial location of center mass that is slightly above the small-amplitude equilibrium state. Figure 4.5 (a) shows the initial location of a droplet suspended on channel with contracting ratio of ε=0.20. The initial center of mass is at $Y_{cm}(\bar{t}=0)$ =-0.13. At that state, the radius of curvatures are not balanced as in Equation 4.5, therefore, the upward capillary force in Equation 4.2 leads the droplet to transit (see Figure 4.5 (b)) to the

equilibrium steady-state of the primary branch as shown in Figure 4.5 (c) at Y_{cm}=1.58. Analytically, the location of the center of mass at the equilibrium steady-state for this case is Y_{cm}=1.60. The CFD results once again match very well the analytical ones, and they show that the small-amplitude equilibrium state of the secondary branch is unstable whereas the large-amplitude of the primary branch is stable.

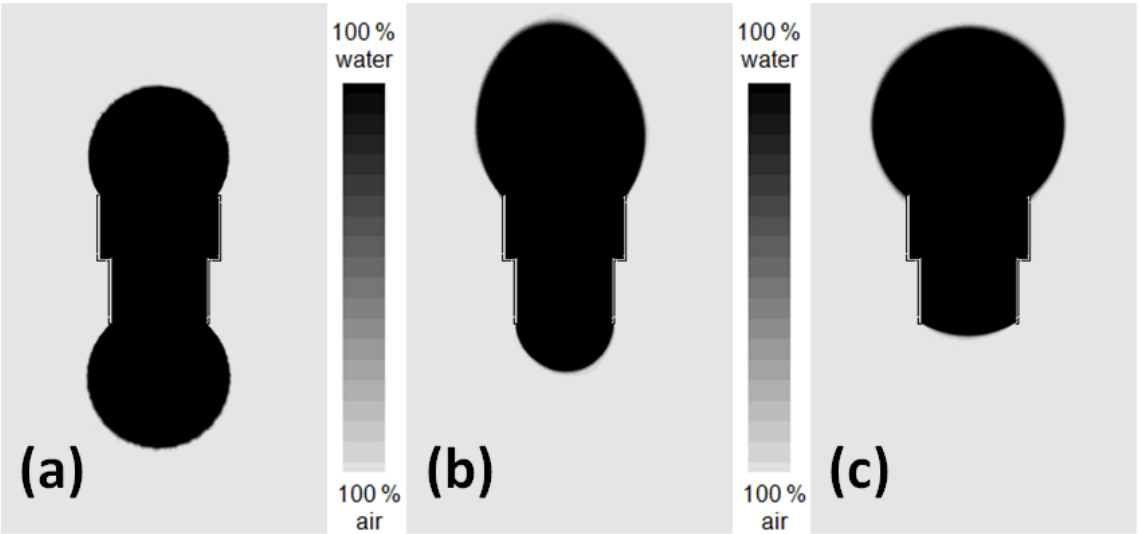

Figure 4.5 Droplet states for $\varepsilon = 0.20$ at V=2.5 with V_{mcr}=1.9 a) Initial state at $\bar{t}$=0, (b) Intermediate state at $\bar{t}$=1.8, (c) Equilibrium state at $\bar{t}$=6.

Additional simulation results for various droplet cap volumes are shown on Figure 4.6. Two CFD cases of contraction ratio ε were used; ε=0.10 and 0.20. Figure 4.6 shows that there exists CFD results above the modified critical volume, V_{mcr}, for both primary and secondary stable state branches. For volumes less than V_{mcr}, CFD results exist only on the primary branch. For the unstable state of the secondary branch, we see that there are no equilibrium CFD results. Moreover, it is difficult to obtain CFD results at the modified critical volume, V_{mcr}, of the secondary branch, because any

numerical disturbance will have a large effect on the stability at that location, which leads the droplet to shift to the stable steady state at the primary branch. Note that the secondary-small amplitude state exists mathematically obtained from Equations 4.5 and 4.6. At that location, the droplet radii of curvature R_U and R_L has the relation of Equation 4.5, that is $R_U = (1 - \varepsilon)R_L$. When the droplet state is disturbed, R_U changes to either smaller or greater than $(1 - \varepsilon)R_L$. Thus, the pressure at the lower cap changes to either larger or smaller than the upper cap, and this pressure difference induces a driving force to move the droplet to either the stable asymmetric state of the primary branch or the secondary branch. All CFD results show a good agreement with the analytical ones for both contraction ratios. These results lead to the conclusion that the large-amplitude solutions are the stable state, and the small-amplitude ones are the unstable state.

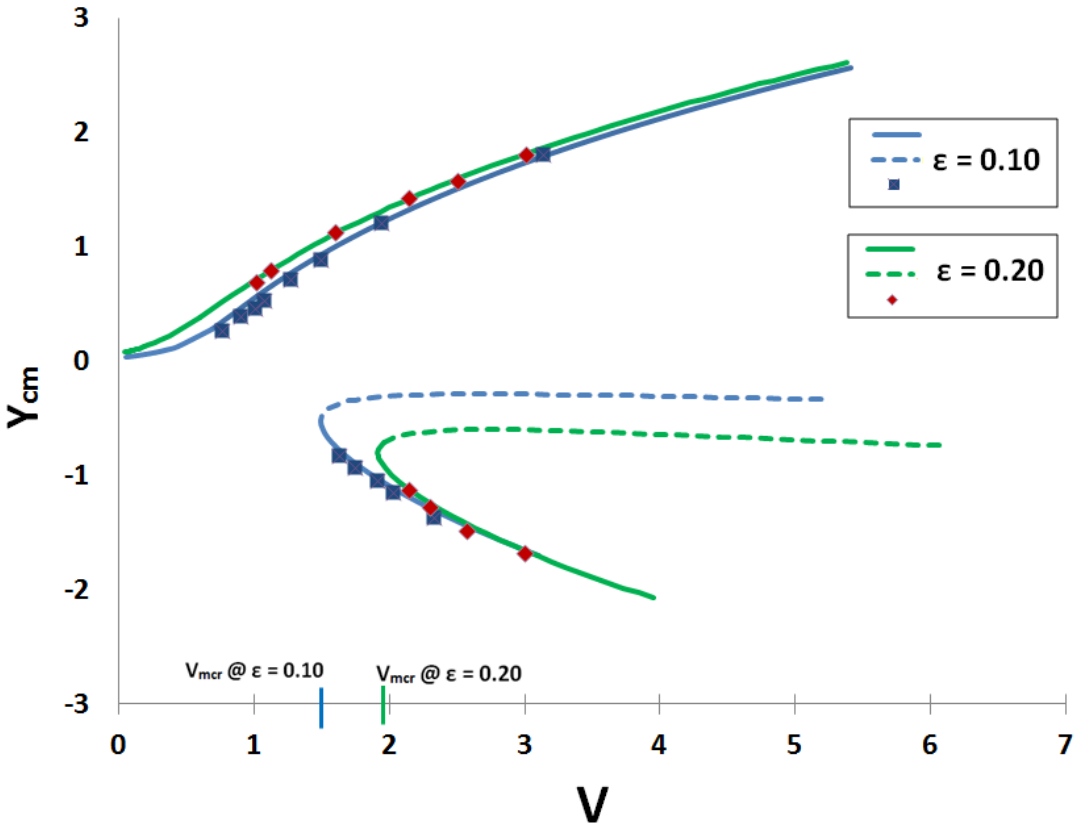

Figure 4.6 Analytical expression (solid line for stable, dashed line for unstable), and CFD solution (dotted marks) of center of mass for $\varepsilon = 0.10$ and $\varepsilon = 0.20$

An explicit explanation of the physical mechanism of the droplet behavior is illustrated in the next paragraphs. In the first case, when $V<V_{mcr}$, and the droplet's center of mass location is at the unsteady state, as shown in Figure 4.7.

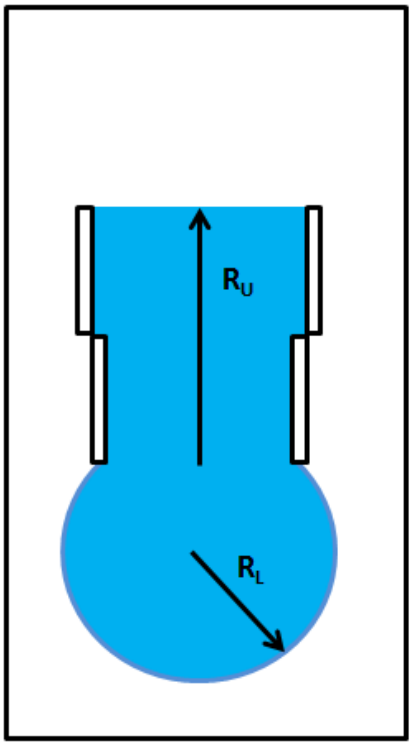

Figure 4.7 Initial condition starting from an unsteady state.

At that state, the upper radius of curvature is infinite, and the lower radius of curvature is finite. According to Equation (4.2), the resultant force is equal to:

$$F_\gamma = 2\gamma\left(r_U\frac{1}{R_L} - r_L\frac{1}{R_U}\right),$$

this leads Equation (4.2) to become

$$F_\gamma = 2\gamma\left(r_U\frac{1}{R_L} - 0\right),$$

and the resultant force is positive. It shifts the droplet in the upward direction with the above capillary.

Without any perturbation or disturbance, the resultant force will push the droplet to reach its final steady state as shown in Figure 4.3(c). At that state, Equation 4.5 applies, and the resultant force is equal to zero,

$$2\gamma\left(r_U\frac{1}{R_L}-r_L\frac{1}{R_U}\right)=0. \quad (4.3)$$

The second case is for $V>V_{mcr}$, and the droplet's center of mass location is starting at the unstable secondary branch location. At that location the droplet is at equilibrium, Equation (4.5) applies, and therefore Equation (4.3) also applies.

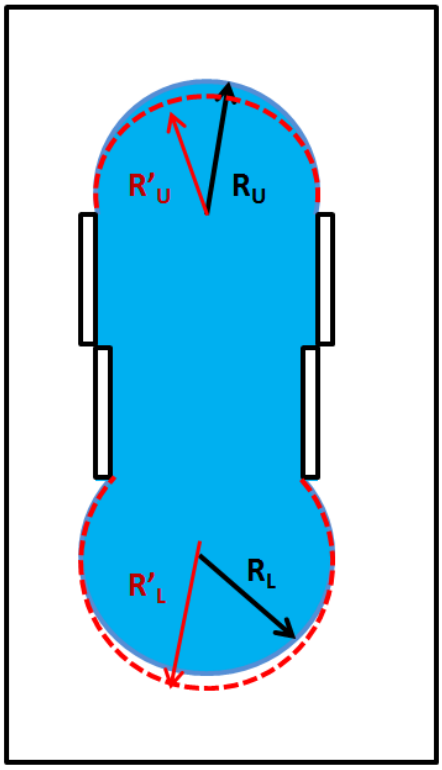

Figure 4.8 Perturbation is introduced to an unstable droplet in an equilibrium state.

As the droplet is perturbed as shown in Figure 4.8, the upper radius of curvature becomes smaller, $R'_U < R_U$, and the lower radius of curvature becomes larger, $R'_L > R_L$. Therefore, according to Equation (4.3) the resultant capillary force becomes negative as follows

$$2\gamma\left(r_U\frac{1}{R'_L}-r_L\frac{1}{R'_U}\right)<0,$$

and that negative resultant force will leads the droplet's center of mass location to move toward stable equilibrium secondary branch, where

$R'_U = (1-\varepsilon)R'_L$, and

$2\gamma\left(r_U \frac{1}{R'_L} - r_L \frac{1}{R'_U}\right) = 0.$

The final case is also for $V>V_{mcr}$, and the droplet's center of mass is at an equilibrium stable state of the secondary branch. At that location, both Equation (4.3) and (4.5) apply. When the droplet is perturbed in the lower direction (see Figure 4.9), the radii of curvature both

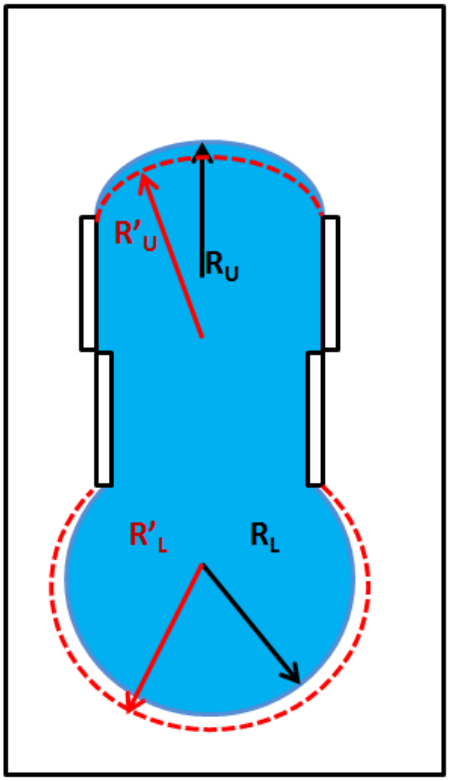

Figure 4.9 Perturbation is introduced to a stable droplet in an equilibrium state.

become larger. However, the amount of increase for the radius of curvature is larger for the upper radius than that for the lower one. That is, $R'_U >> R_U$, and $R'_L > R_L$. Therefore,

$R'_U > R'_L$, and this leads to have the first term of Equation 4.3 to become larger than the second term. Therefore, when the lower perturbation occurs

$$2\gamma\left(r_U \frac{1}{R'_L} - r_L \frac{1}{R'_U}\right) > 0,$$

and that positive resultant force will push back the droplet' center of mass to return to the stable equilibrium state of the secondary branch.

CHAPTER FIVE: STRAIGHT CHANNEL WITH GRAVITY

In this chapter, a droplet of a two-dimensional, viscous, Newtonian, and incompressible fluid surrounded by air is studied in a channel where the droplet is suspended and under a variable gravitational force. Similar to the previous chapters, the channel is located in the center of the computational domain, and the channel's width and length are 2r and 2L, respectively (see Figure 3.2 in chapter 3). R_U and R_L are the upper and lower cap radii of curvatures, respectively.

5.1 Mathematical model

Similar to the contracting channel case, the presence of gravity, g>0, alters the equilibrium relationship between R_U and R_L. In order to consider the effect of gravity on the droplet stability, we start by performing a vertical force balance on the droplet system

$$F_{inert} = F_\gamma + F_\mu + F_g, \tag{5.1}$$

where F_{inert} is the inertia force of the droplet and depends on liquid density ρ, the total droplet volume V_T , and the acceleration of the center of mass location Y_{cm}. The inertia force term is written as follow:

$$F_{inert} = \rho V_T \frac{\partial^2 Y_{cm}}{\partial t^2}. \tag{5.1a}$$

The first term of the right hand side of equation (5.1), F_γ, is the capillary force that resulted from the two droplet caps. The parameter F_γ can be expressed as functions of the channel half width r and the pressure difference between the droplet caps $(p_U - p_L)$,

$$F_\gamma = 2r(p_L - p_U). \tag{5.1b}$$

With the Young-Laplace relation, the capillary force can also be written as

$$F_\gamma = 2r\gamma\left(\frac{1}{R_L} - \frac{1}{R_U}\right). \tag{5.1c}$$

In Equation (5.1), F_μ, which is the viscous force along the channel walls per unit depth, is written as

$$F_\mu = 2\int_{-L}^{L} \tau_w \, dy, \tag{5.1d}$$

where $\tau_w = \mu\left(\frac{\partial V_{vel}}{\partial y}\right)_w$ is the shear force along a wall, L is the channel half length, μ is viscosity, and V_{vel} is velocity in vertical direction. Finally, the gravitational force is denoted as F_g, and it is expressed as

$$F_g = -\rho V_T g, \tag{5.1e}$$

where V_T is the total droplet volume. Rewriting equation (5.1), we get

$$\rho V_T \frac{\partial^2 Y_{cm}}{\partial t^2} = 2r\gamma\left(\frac{1}{R_L} - \frac{1}{R_U}\right) + 2\mu \int_{-L}^{L} \left(\frac{\partial V_{vel}}{\partial y}\right)_w dy - \rho V_T g. \quad (5.2)$$

As the system approaches to the final equilibrium state, terms associated with velocities and accelerations will be diminished. Thus, equation (5.2) yields

$$0 = 2r\gamma\left(\frac{1}{R_L} - \frac{1}{R_U}\right) - \rho V_T g. \quad (5.2a)$$

Re-arranging the above obtains the relationship between R_L and R_U,

$$R_U = \frac{1}{\frac{1}{R_L} - \frac{\rho V_T g}{2r\gamma}} \ . \quad (5.2b)$$

Since total volume consists of two droplet cap volumes V_{U+L} and the channel volume V_0, equation (5.2 b) is then written as

$$R_U = \frac{1}{\frac{1}{R_L} - (V_{U+L} + V_0)\frac{\rho g}{2r\gamma}} \ . \quad (5.2c)$$

When the radius of curvature R is normalized by the channel half width r, equation (5.2b) becomes

$$\bar{R}_U = \frac{1}{\frac{1}{\bar{R}_L} - (\eta + \beta)}, \tag{5.2d}$$

where β is a design parameter defined as $\frac{\rho 2rLg}{\gamma}$. The parameter β depends on the geometry of the system and fluid properties. Thus, it remains unchanged for each design case. The parameter β and the bond number B has a relation of $\beta = cB$, where c is a coefficient that describes the ratio of the channel half width, r, and height, L. On the other hand, η is a run parameter defined as $\frac{\rho V_{U+L} g}{2\gamma}$. The run parameter varies with the droplet cap volume.

From equation (5.2d), the maximum beta value, β_{max}, occurs when $\bar{R}_U$ goes to infinity, or

$$\beta_{max} = \left(\frac{1}{\bar{R}_{L_{in}}}\right) - \eta, \tag{5.3}$$

where the in subscript denotes as an initial value.

5.2 Results and discussion

In a preliminary study for g=0, β and η are equal to zero. Thus, $R_L = R_U$ (see Equation (5.2d). The analytical solution is shown in Figure 3.9 and fully explained in Chapter 3. As gravity is introduced, β and η values become positive. The first case is for g=9.81 m/s^2. The fluid properties (ρ, γ) are kept the same as in the preliminary case (g=0), thus for g=9.81 m/s^2, $\beta = 0.207$. Corresponding analytical and CFD results are shown in Figure 5.1. In this case, there exists only one stable state that gradually

changes from nearly symmetric to asymmetric state as volume increases to V=2.2. The volume V=2.2 in this case is called the primary branch maximum volume V_{p_max}, and it depends on β_{max} as V_U approaches to zero (or $\bar{R}_U$ approaches to infinity). This analytical prediction has been verified by CFD results, represented as dotted marks along the analytical stable solution. Note that the CFD solution starts to deviates from 2.2<V<3.4, the reason for this will be explained later. For V>3.4, there exists no CFD solution because the mass of the droplet is sufficiently large that the capillary force cannot keep the droplet pinned in the channel.

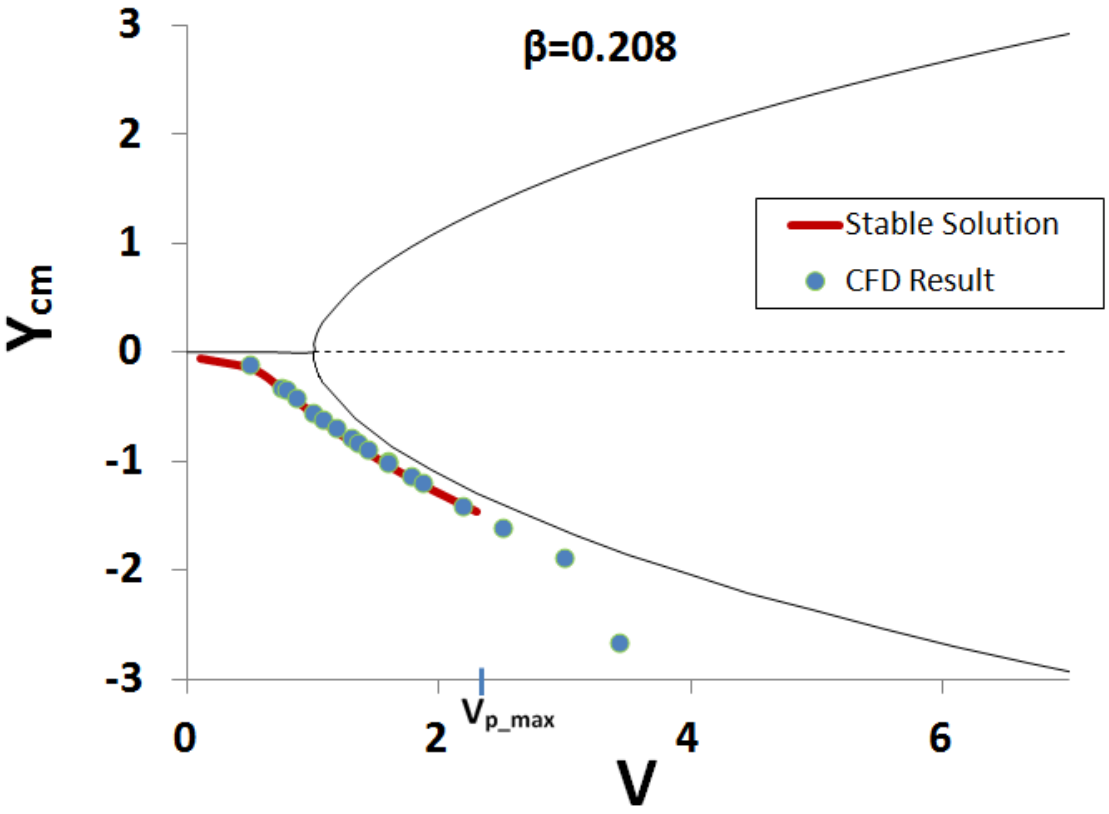

Figure 5.1 Analytical expression (thick solid line), and CFD solution (dotted marks) for $\beta = 0.208$

For cases with $\beta > 0$, the bifurcation diagram will shift from its symmetric state at Y_{cm}=0. In an effort to determine the existence of the secondary branch state, the value

of β is varied. Four values of β are tested in our study; $\beta = 0.0420, 0.0640, 0.106$ and 0.208. Figure 5.2 shows the analytical as well as the CFD solution for the $\beta = 0.042$ value, which corresponds to a gravity of 2 m/s^2. The figure shows that the critical volume for g=0 is shifted to V_{mcr}, where V_{mcr}=1.38. The primary state extends from V=0 to V_{p_max}=8.62 (as it will be shown later on Figure 5.3). Starting from the modified critical volume V_{mcr}, the secondary state bifurcates into stable and unstable states. The upper branch of the secondary state is stable, while the lower branch (dashed line) is an unstable state. The discussions of stability of the droplet state using CFD will be described later in this chapter. In the unstable state, Equation (5.2d) still holds, but the droplet cannot maintain its state due to numerical inaccuracy that creates a slight disturbance, which leads to shifting the droplet to either the primary or secondary asymmetric stable state. All solutions have been tested by CFD simulations (dotted line in Figure 5.2), and they are in close agreement with analytical solutions. At V_{mcr} the numerical disturbance will have a significant effect on the stability of the center of mass, therefore, it is difficult to obtain CFD results at that location.

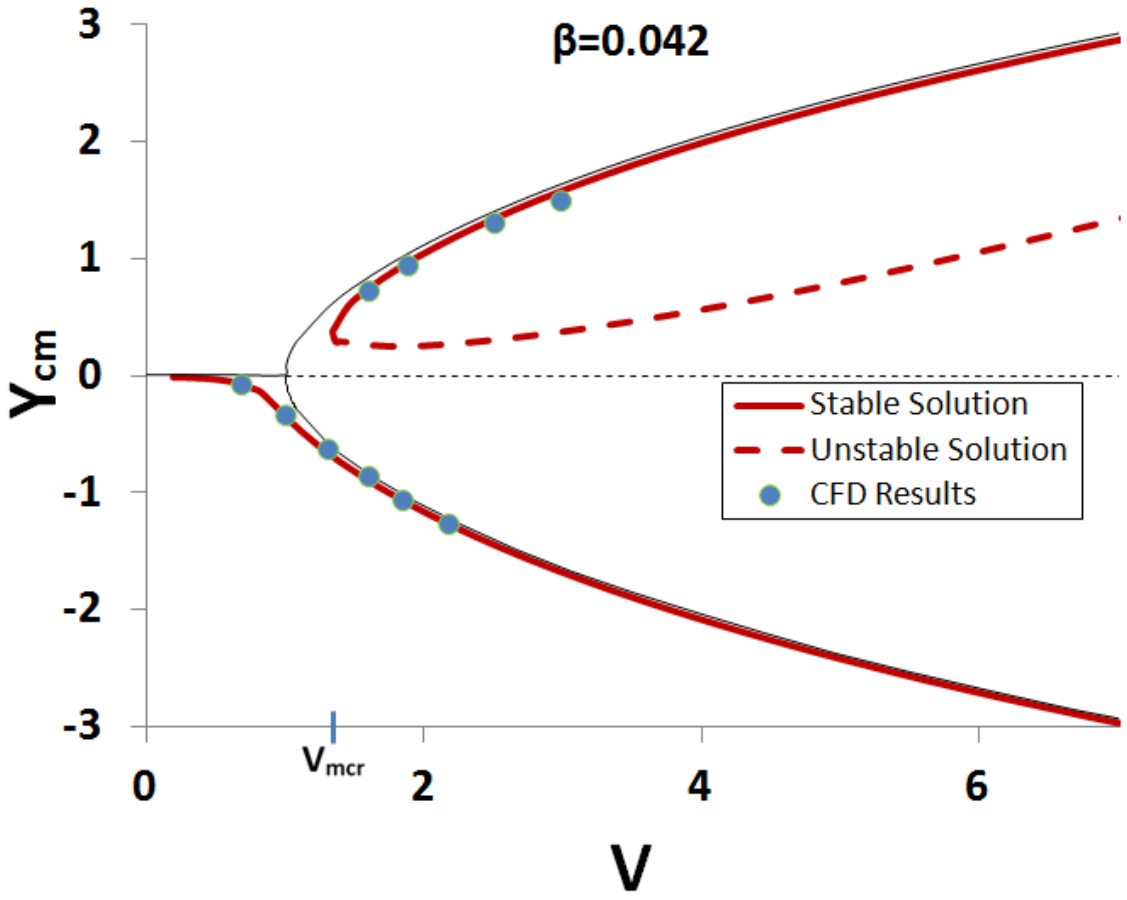

Figure 5.2 Analytical expression (thick solid line), and CFD solution (dotted marks) of center of mass for $\beta = 0.042$

The analytical solutions for the four β cases, which are verified with CFD, are shown in Figure 5.3. In the figure, there are 4 primary lower branches ($Y_{cm}<0$). The primary maximum volume, V_{p_max}, that the droplet can sustain while $Y_{cm}<0$, increases with decreasing the value of β, as indicated in Figure 5.3. Solutions of the secondary branch are in a form of airfoil-like closed loops, where the leading edge of the loop is the modified critical volume V_{mcr}. The large-amplitude asymmetric state along the secondary branch is stable, and the small-amplitude asymmetric state along the secondary branch is unstable. Note that these states meet again at the trailing edge of the

loop, which is defined as a secondary maximum volume V_{s_max}. From both CFD and analytical cases, we found that as the value of β increases, the value of V_{mcr} gets larger and V_{s_max} becomes smaller, which leads to the solution loops to become nested. When β reaches a value of approximately 0.127, the secondary branch disappears. The corresponding value is called the critical β, or β_{cr}=0.127, which is a universal value for this droplet system. Note that for $\beta > \beta_{cr}$ there exists only a primary branch. When $\beta < \beta_{cr}$, the secondary branch exists, and the maximum volume of the primary state, V_{p_max}, is located in between the modified critical volume, V_{mcr}, and the secondary maximum volume, V_{s_max}. The reason for this is when the droplet is asymmetric on the secondary branch, i.e., Y_{cm}>0, the lower radius of curvature produces a large upward force against the droplet's weight, which sustains the droplet for larger V_U. When droplet is on the opposite side residing at the primary branch, the lower radius of curvature is much smaller; therefore, the upward force cannot sustain the droplet volume.

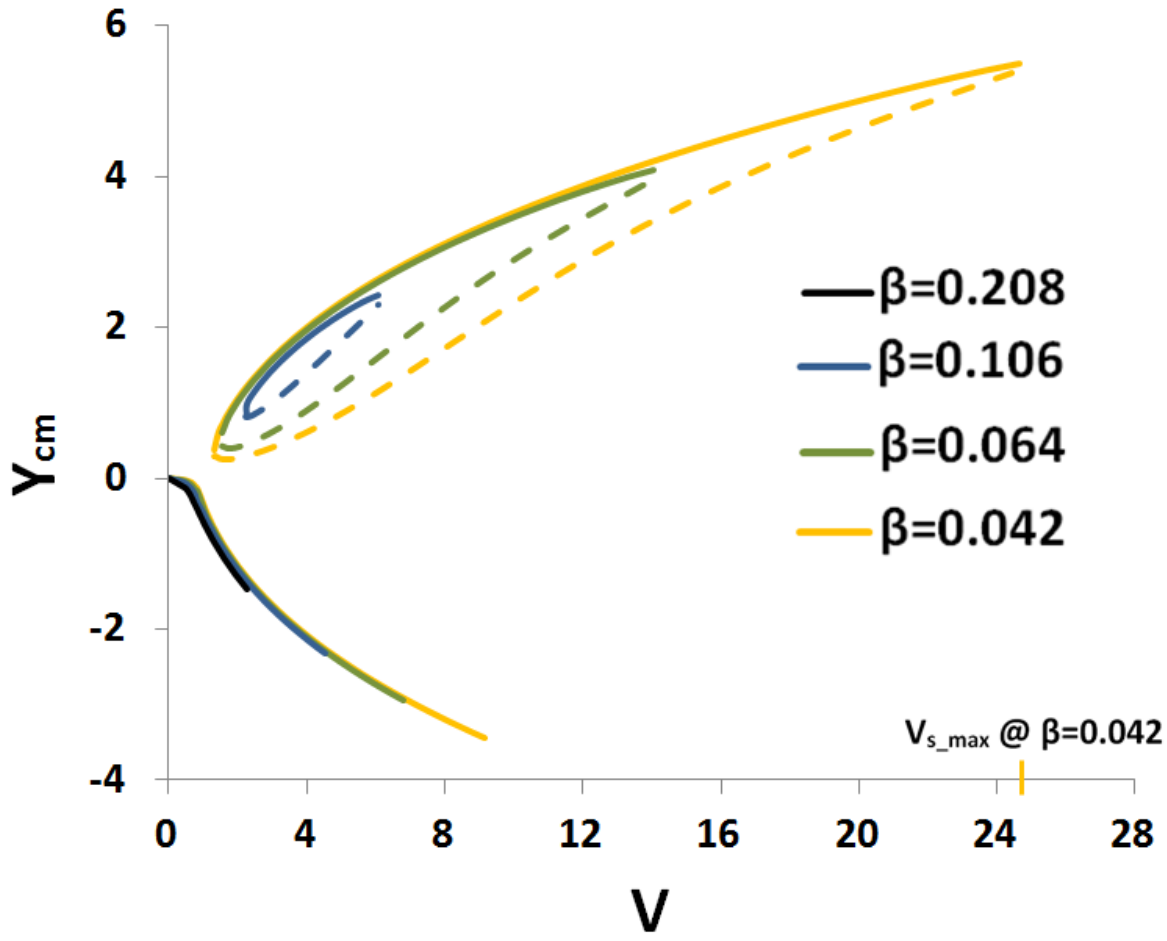

Figure 5.3 Stability chart for $\beta = 0.042$ ($g = 2\ m/s^2$), 0.064 ($g = 3m/s^2$), 0.106 ($g = 5m/s^2$) and 0.208 ($g = 9.81m/s^2$).

It should be noted that at droplet volumes near the maximum, the CFD results of the center of mass location start to deviate from its analytical one, and in other cases it goes beyond the maximum droplet volume (also as shown in Figure 5.1). Figure 5.4 shows the case for β=0.106. As the primary branch of the analytical solution reaches its maximum value of V_{p_max}=4.5, we notice that there still exists a CFD solution beyond V_{p_max}. From the figure we see that the CFD maximum volume is V_p=5.5, that is a deviation value of 22% from the analytical volume. Similarly, on the secondary branch, there was a deviation in the center of mass Y_{cm} at volumes greater than V=3. At V=6,

the analytical Y_{cm} at V_{s_max} is 2.42, while CFD results show 10% deviation at Y_{cm}=2.18. The reason for these variations in the simulation results is due to the failure of a perfectly spherical droplet cap assumption. This is evident in the deformation (see Figure 5.5) of the droplet surfaces on the CFD simulation especially at larger droplet volumes. However, the analytical solution predicts very well up to V_{p_max}, which implies that the droplet maintains its spherical shape around that volume. In addition, unlike the CFD results on the primary branch, on the secondary branch there was no CFD results beyond the V_{s_max}. The reason is that the inertial force resulting from the gravity and the upper capillary force at that location are much larger than the lower capillary force from the droplet. Therefore, the droplet forcefully moves downward and completely detaches from the channel wall.

On the primary branch, the location of the center of mass near V=5.5 starts to deviate significantly due also to the deformation of the droplet. As seen in Figure 5.5, when the droplet starts to deform (red dashed line in the figure), the radius of curvature becomes smaller than that of the perfectly circular case (blue dashed line), and that imposes a larger lower capillary force. The upper radius of curvature is very large as the upper cap is almost flat; therefore, the upper capillary force is negligible. Therefore, at that state, the lower capillary force is at equilibrium with the opposite gravitational force and the upper capillary force as well.

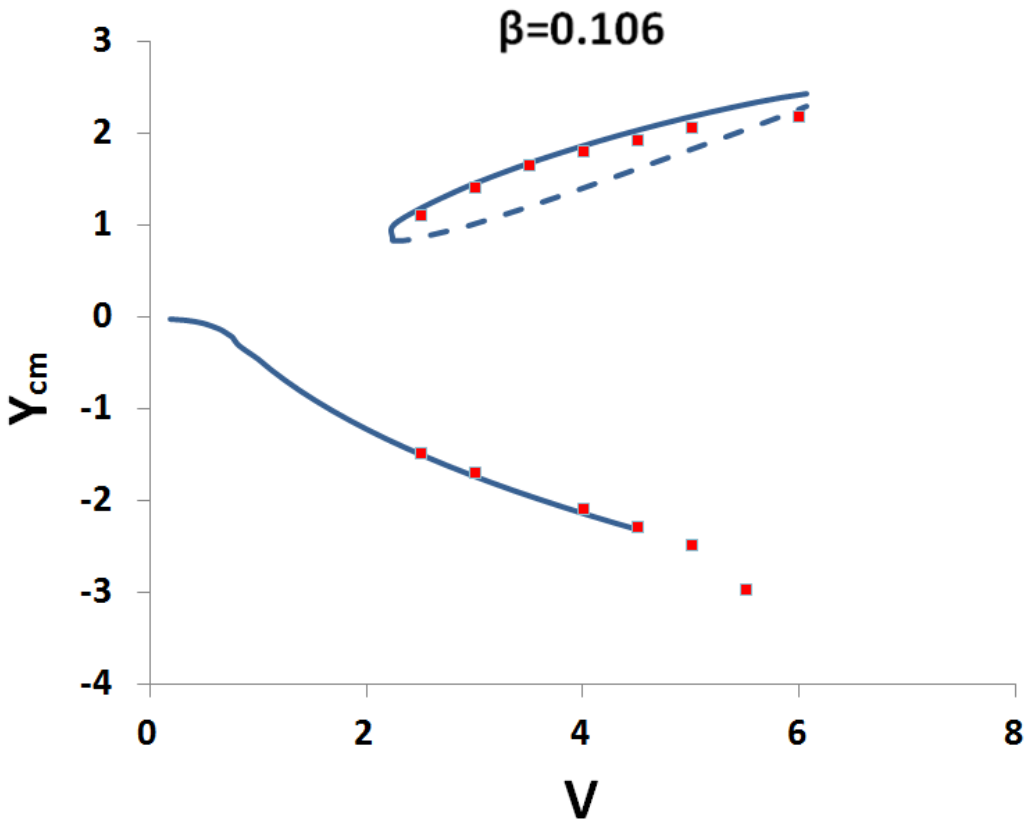

Figure 5.4 Deviation of CFD results (dots) from the analytical ones (solid and dashed lines) at β=0.106.

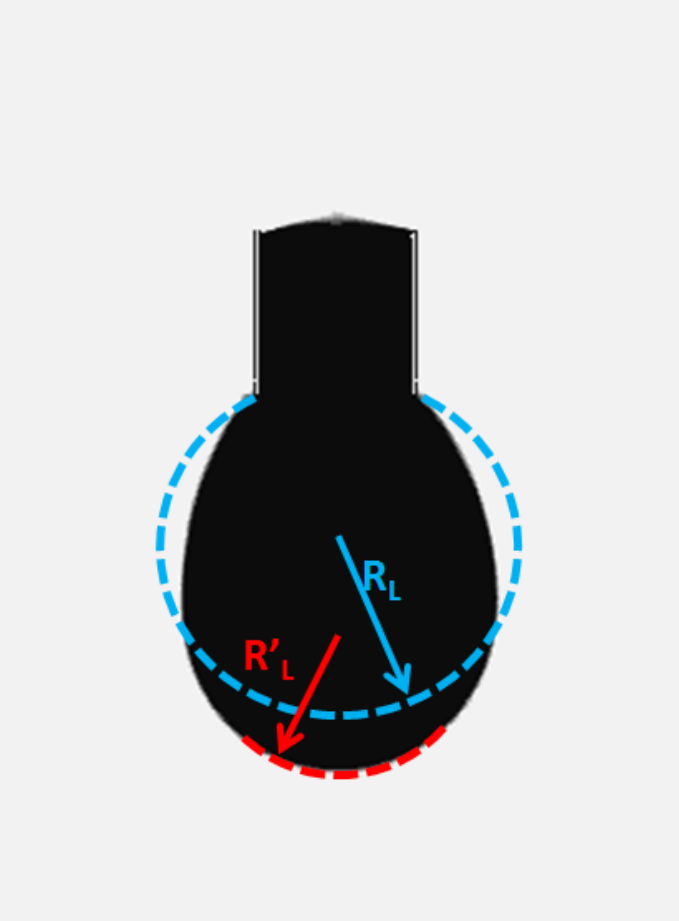

Figure 5.5 Droplet final state at V=5.5 and β=0.106, shows a deformation on the droplet surface.

To further verify the analytical stability state numerically, a single value of $\beta = 0.106$ (g=5 m/s^2) is tested for five droplet volumes: V=1.7 for the case below the modified critical volume V_{mcr},; three cases of V=3, which are within the upper and lower solution of the secondary branch; and V=7, which is greater than the secondary maximum volume V_{s_max}, where there are no solutions. Figure 5.6(a) shows the CFD image of the initial condition of the first case, namely, $\beta = 0.106$ and V=1.7, where the initial center of mass is $Y_{cm}(\bar{t}=0)=0.92$. At this time, both capillarity and gravity produce a downward force. According to the stability chart (Figure 5.3), the initial cap

volume is smaller than V_{mcr}, which results in not having any solution on the secondary branch; however, there exists an analytical solution on the primary branch at Y_{cm}=-1.03. Figure 5.6(b) shows the simulation transition ($\bar{t}$=0.5) of the droplet, which still moving downward. Figure 5.6(c) shows the equilibrium state, where Y_{cm}=-1.01. Analytical and CFD results are in good agreement.

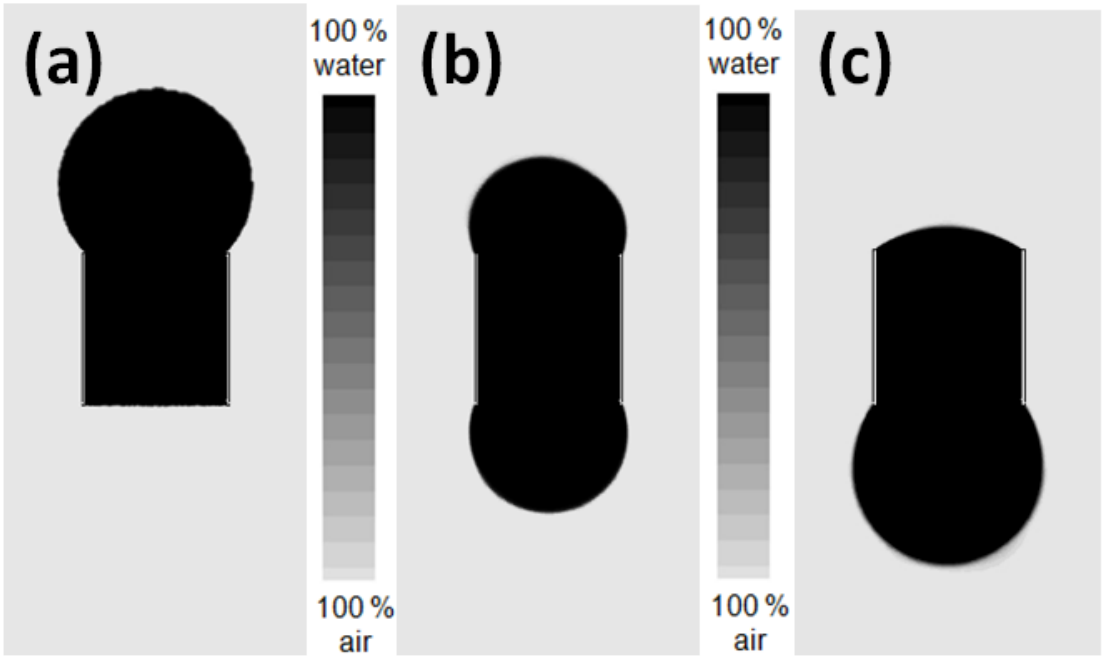

Figure 5.6 Droplet states for $\beta = 0.106$ at V=1.7 with V_{mcr}=2.25 (a) Initial state at $\bar{t}$=0, (b) Intermediate state at $\bar{t}$=0.5, (c) Equilibrium state at $\bar{t}$=3.

When the droplet volume is V=3, and starting with an initial center of mass location that lies above the unstable state line, the equilibrium state should be on the upper-stable state line. Figure 5.7(a) shows the CFD simulation of the initial state of V=3, and the center mass is Y_{cm}=1.78. As the droplet in the simulation begins to move,

it oscillates within the region above the unsteady state (Figure 5.7(b)), and then it settles at the steady asymmetric state of the secondary branch at Y_{cm}=1.48 and $\bar{t}$=5 (Figure 5.7(c)). The analytical solution on Figure 5.3 shows that the upper stable state for V=3 and $\beta = 0.106$ is Y_{cm}=1.47, which is a close match with the CFD results.

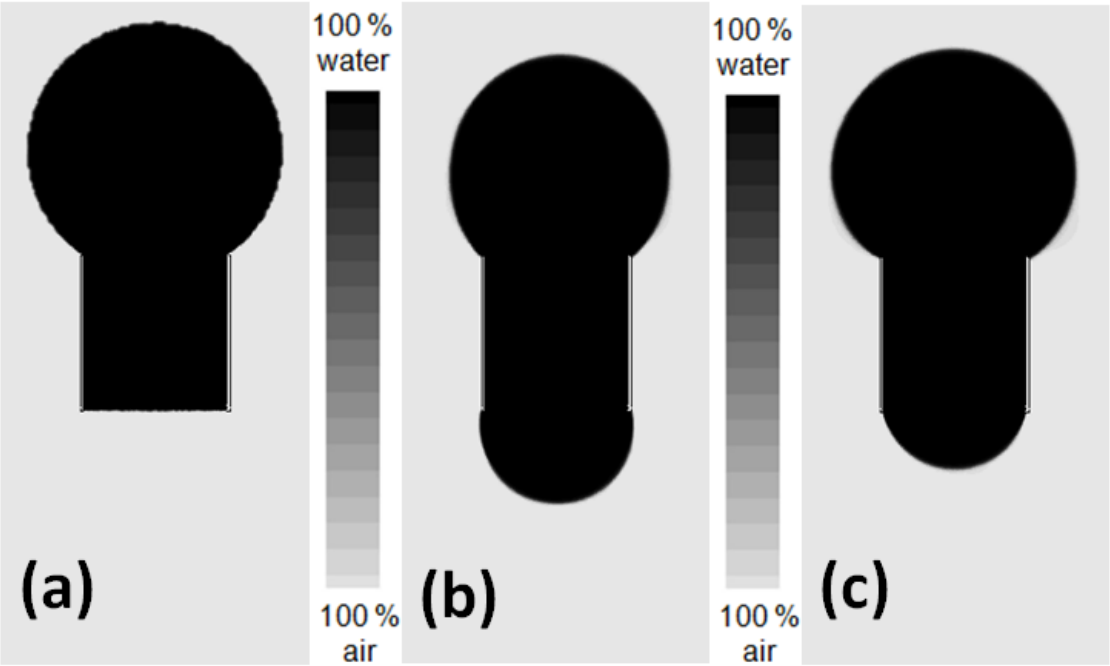

Figure 5.7 Droplet states for $\beta = 0.106$ at V=3 with V_{mcr}=2.25 and V_{s_max}=6.07 a) Initial state at $\bar{t}$=0, (b) Intermediate state at $\bar{t}$=1.1, (c) Equilibrium state at $\bar{t}$=5.

The third case is for V=3, and the initial condition is at the unstable state of the secondary branch at $Y_{cm}(\bar{t}=0)$=1.02, as shown in Figure 5.8(a). The droplet shifts from the unstable state to the stable state of the secondary branch and stays in equilibrium at at Y_{cm}= 1.49 at $\bar{t}$=3. This simulation case proves that the small-amplitude secondary branch is the unstable state.

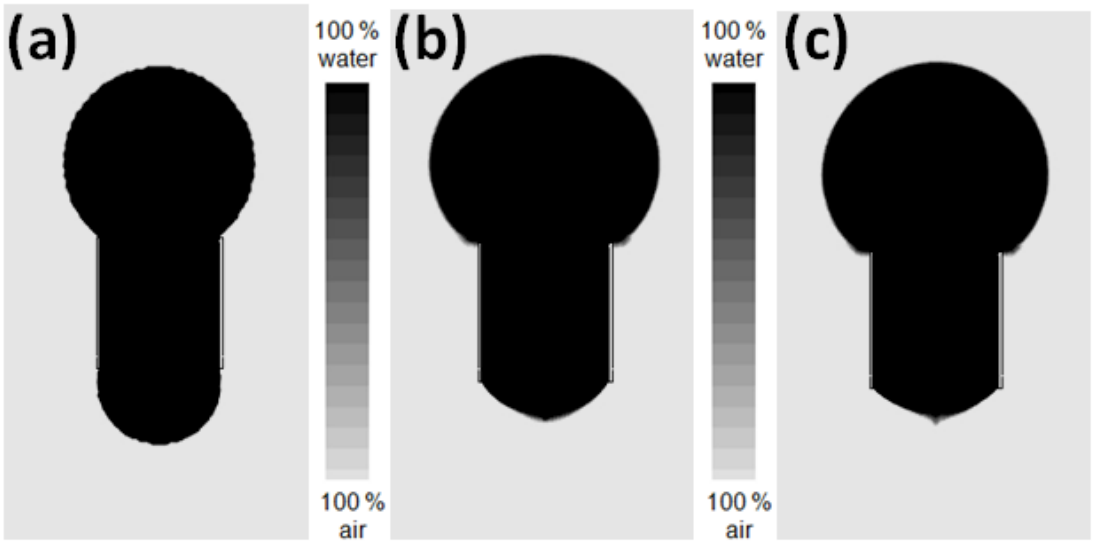

Figure 5.8 Droplet states for $\beta = 0.106$ at V=3 with V_{mcr}=2.25 and V_{s_max}=6.07 a) Initial state at $\bar{t}$=0, (b) Intermediate state at $\bar{t}$=0.9, (c) Equilibrium state at $\bar{t}$=3.

The fourth case is also for V=3, and the initial condition is below the unstable state line. Figure 5.9 (a) shows the initial condition at $Y_{cm}(\bar{t}=0)$=-1.78, which is well below the unstable state line. The droplet then transits towards the primary stable state as shown at $\bar{t}$=0.9 in Figure 5.9 (b). The equilibrium state occurs at $\bar{t}$=2.5 and Y_{cm}=-1.74 (Figure 5.9 (c)), which matches very well with the analytical solution results of Y_{cm}=-1.76, shown on the stability graph on Figure 5.3.

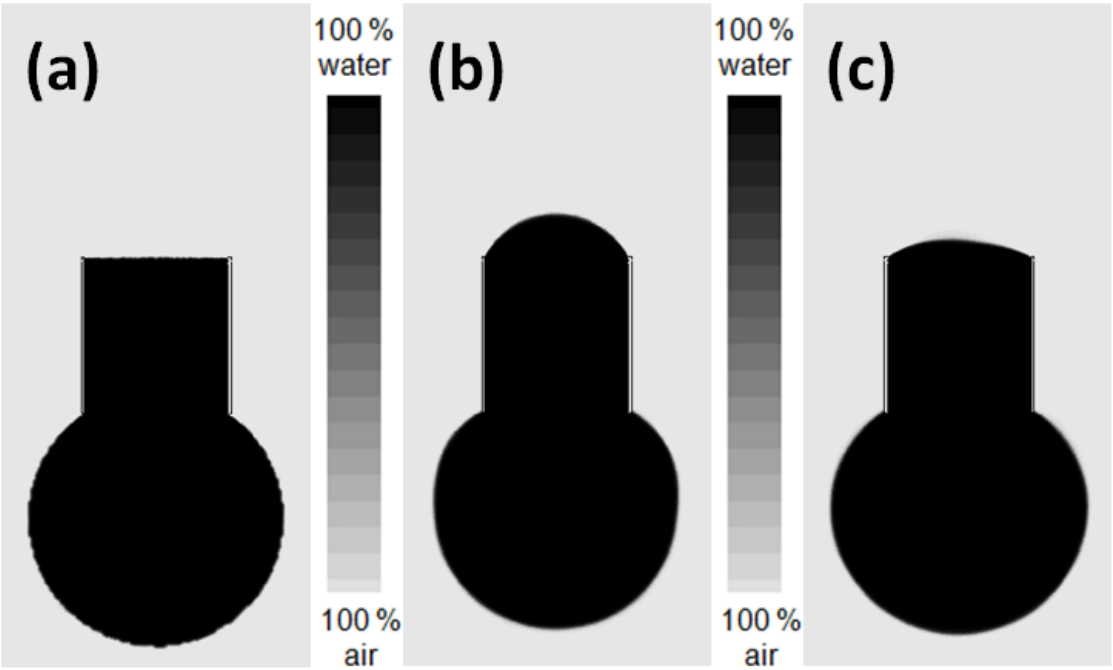

Figure 5.9 Droplet states for $\beta = 0.106$ at V=3 with V_{p_max}=4.29 a) Initial state at $\bar{t}$=0, (b) Intermediate state at $\bar{t}$=0.9, (c) Equilibrium state at $\bar{t}$=2.5.

The final case is for the much larger volume of V=7 which is larger than V_{s_max}. This implies that there is no stable state for this droplet on both primary and secondary branches. As shown in Figure 5.10 (a), the initial state is at $Y_{cm}(\bar{t}=0)$=1.02. At that center of mass, the gravity force exerted on the droplet exceeds any capillary force the droplet cap can sustain; therefore, it goes through the channel, shown at $\bar{t}$=1.3 on Figure 5.10 (b), and fully detaches from the channel walls at $\bar{t}$=1.7 (Figure 5.10 (c)). This result is expected from the analytical results.

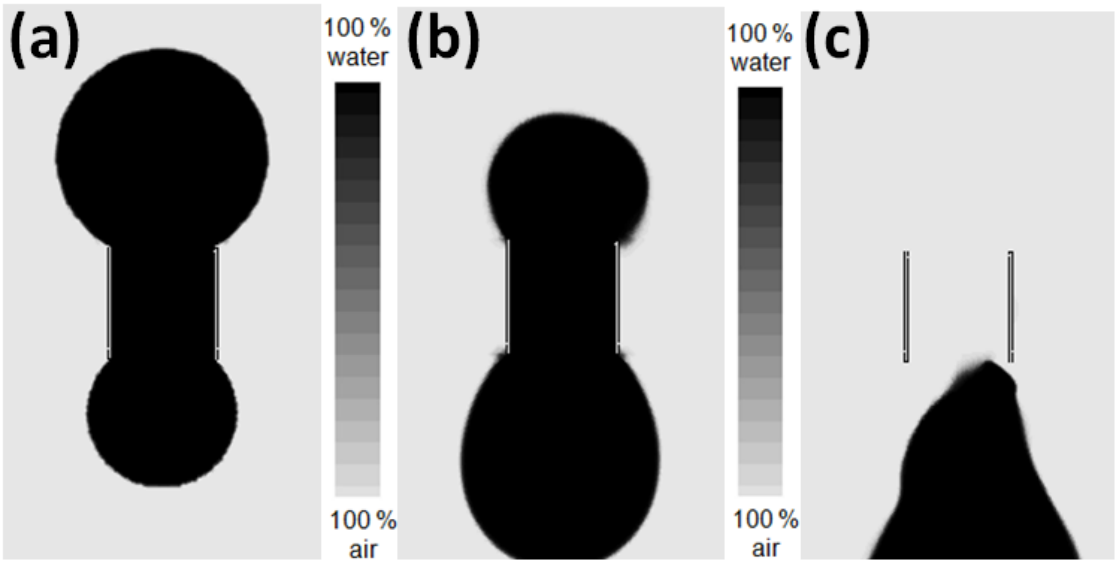

Figure 5.10 Droplet states for $\beta = 0.106$ at V=7 with V_{mcr}=2.25 and V_{s_max}=6.07. a) Initial state at $\bar{t}$=0, (b) Intermediate state at $\bar{t}$=1.3, (c) Detachment $\bar{t}$=1.7.

The physical mechanism of the droplet behavior is discussed next. The first case is for $V<V_{mcr}$, and the droplet's center of mass is starting from an asymmetric and positive center of mass, away from the stable primary branch, as shown in Figure 5.11.

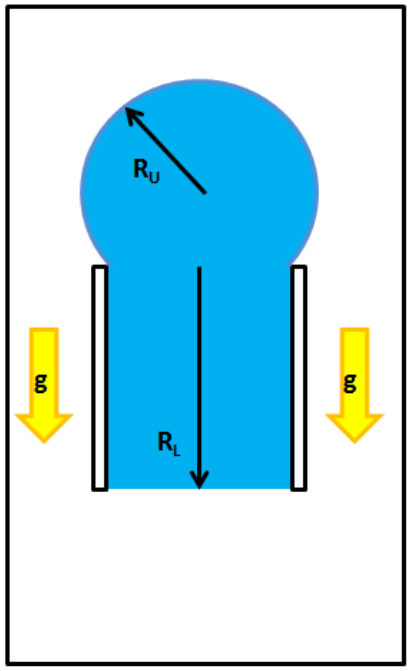

Figure 5.11 Asymmetric initial condition for a droplet under gravitational force.

According to the Young-Laplace relation of Equation (5.1c), the capillary force is written as follows:

$$F_R = 2r\gamma\left(0 - \frac{1}{R_U}\right) - \rho V_T g = -\frac{2r\gamma}{R_U} - \rho V_T g,$$

and therefore, there is a negative capillary force in addition to negative gravitational force that lead the droplet's center of mass to move towards the stable primary branch solution. Note that we neglected the opposite shear force resulted from the fluid viscosity due to its minimal effect. The viscous force will have a contribution on the timing at which the droplet reaches its final state, but not on the final state location, which is our concern here.

The second case is for $V>V_{mcr}$, the droplet's center of mass is located at the unstable secondary branch. At that location, both radii of curvatures are in equilibrium as in Equation (5.2d), and their resultant force is equal the total gravitational force, as shown in Equation (5.2a). With little modification Equation (5.2a) is as follows

$$2r\gamma\left(\frac{1}{R_L} - \frac{1}{R_U}\right) = \rho V_T g.$$

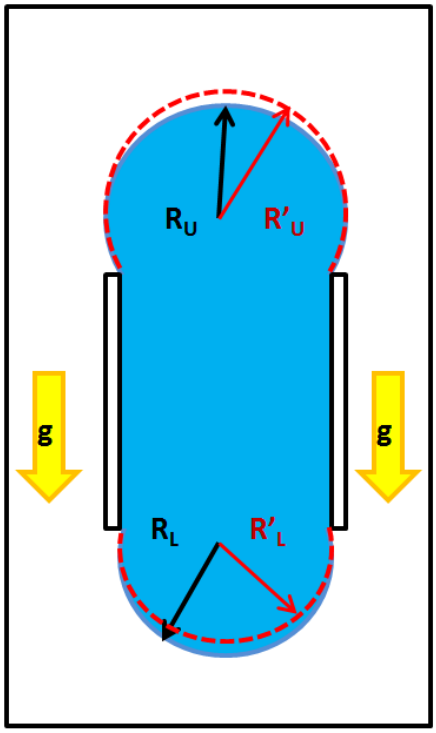

Figure 5.12 Initial unstable state of a droplet under gravitational force.

When a small perturbation is introduced to the droplet on a direction opposite to the gravitational force, as shown in Figure 5.12, the upper radius of curvature becomes larger, $R'_U > R_U$, and the lower one becomes smaller, $R'_L < R_L$. When that occurs, the capillary term of Equation 5.2 becomes larger than the gravitational term. That is,

$$2r\gamma\left(\frac{1}{R'_L}-\frac{1}{R'_U}\right) > \rho V_T g,$$

and that will cause the droplet to move opposite of the gravitational force, and shifts toward the stable state of the secondary branch.

The final case is for $V > V_{mcr}$, and the center of mass of the droplet is on the stable state of the secondary branch. At that location, both Equations (5.2a) and (5.2d) apply. As a little disturbance is introduced as shown in Figure 5.13, the lower radius of curvature becomes much larger, $R'_L >> R_L$, and the upper radius of curvature also

becomes larger but not as much as the lower one, $R'_U > R_U$. Therefore, the negative force resulting from the upper radius of curvature is much larger than the lower one, and the resultant force from both caps is less than the gravitational force, that is,

$$2r\gamma\left(\frac{1}{R'_L}-\frac{1}{R'_U}\right) < \rho V_T g.$$

This downward force will bring the droplet's center of mass location back to its stable state at the secondary branch.

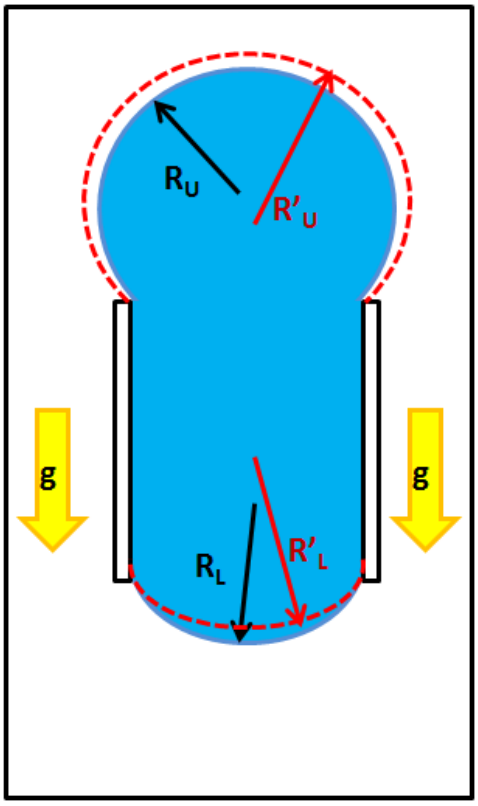

Figure 5.13 Initial stable state of a droplet under gravitational force

As discussed in the previous section, in addition to gravity g, the β parameter is also a function of the channel volume V_o, density ρ, and surface tension γ. This indicates that the change of these variables will yield a similar droplet final state.

However, although the initial states are the same, the droplet dynamics toward the equilibrium state will not be the same, as discussed in the next paragraph.

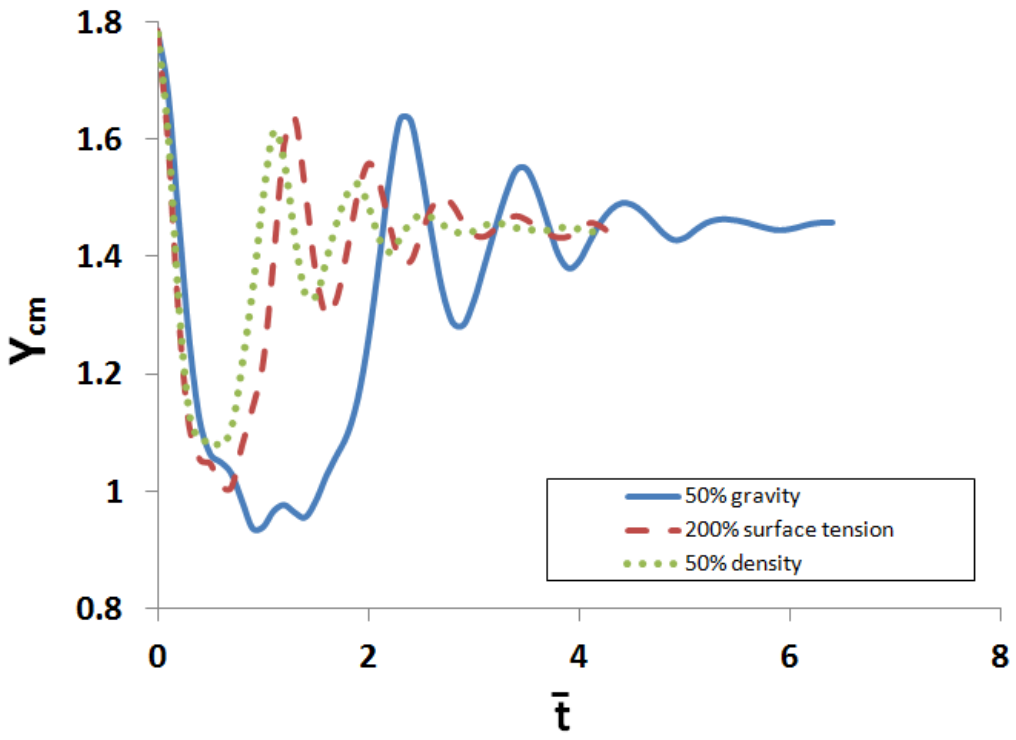

Figure 5.14 The time rate of change of the center of mass at $\beta = 0.106$

Three CFD cases are performed where the β value remains fixed. Some of the fluid properties that are variable in β, as well as of gravity, have been changed from their original values, that is, g=9.81 m/s^2, $\rho = 998.2\ kg/m^3$, $\gamma = 0.072\ N/m$ and $\beta = 0.204$. The three cases are for V=3, and in the first case, the gravity is reduced by 50%, and all the fluid properties are kept the same. In the second case, the density is reduced by 50%, and in the third and final cases the surface tension is doubled. It should be noted that after each change, β is now 0.106, and the channel volume V_0 is kept constant for all cases. From Figure 5.14 one can observe that the final center of mass

reaches the final steady state at Y_{cm}=1.4 for all the three cases. The oscillation, however, for each case differs, especially for the gravity-change case where it reaches the steady state at $\bar{t}$=7. For the surface tension case, the droplet reaches the steady state at $\bar{t}$=5, and for the density case, the center of mass reaches the final steady state at little shorter time than in the surface tension case, at $\bar{t}$=4.5. It can be seen that there is a small difference when varying the surface tension and density; however, the big difference occurs when altering the gravity value.

When density or gravity is reduced by half, F_g becomes halved according to equation (5.1e). However, the density case also reduces the inertia of the system (see equation (5.1a)), which reduces the amplitude of oscillation and the time to converge to the steady-state. On the other hand, the gravity case does not reduce the inertial force of the system, indicating that the system induces higher amplitude of oscillation and longer time to converge to the steady-state.

When the surface tension is doubled, the force balance equation (5.1) of the surface tension case becomes same as that of density case if the viscous force term is doubled. Since the viscous term is smaller for the surface tension case, the oscillation motion becomes longer and induces longer time to converge to the steady-state. Such a difference in droplet dynamics might affect the final droplet state depending on its initial state. For example, high amplitude of the droplet oscillation might pass the unstable state line and loses its stability on the secondary branch, which could lead to settling on the primary branch, or detaching completely out of the channel walls.

CHAPTER SIX: SUMMARY AND FUTURE WORK

6.1 Summary

We studied the stability of a two-dimensional, incompressible water droplet, with two cylindrical-caps that is pinned in a straight channel, through the use of CFD. Suspended droplet states are measured by the location of the center of mass of the droplet initially with zero gravity effect, then followed by a contraction in the channel holding the droplet $\varepsilon>0$, and finally with the effect of gravity, $\beta>0$. When g is neglected and channel is straight, there is a critical droplet volume, V_{cr}, where a bifurcation of asymmetric states occurs. For $V<V_{cr}$, there exists only one stable and symmetric droplet state. On the other hand, when $V>V_{cr}$, there exist three droplet states: two asymmetric stable states and one symmetric unstable state. Analytical and CFD simulation results showed that these equilibrium states would be achieved when the upper and lower radii of curvature were equal. We then computed Hamiltonian of the droplet system using CFD simulations for various droplet volumes. We demonstrated that σ_H for symmetric cases grows monotonically with V. Moreover, $\sigma_H < 0$ when V<1 and $\sigma_H > 0$ when V>1. σ_H becomes the maximum at V=1.8 and less for higher values of V. This was due to the slow reaction of the larger mass of the droplet. Yet, it is found that σ_H is always positive in the range of our study 1<V<13. We also found that σ_H for asymmetric cases is negative for all V<1. The σ_H decays monotonically with V, reaches a maximum decay rate at V=1.8, and becomes less for higher values of V. For V > 1.8 we observed that the time taking to complete the transition process becomes longer as V increases because both the growth rates from the symmetric states and the decay rates to the

asymmetric states become slower. We also explained this transition phenomena based on the Laplace-Young equation. The CFD simulations clarify the relationship between the experimental observations and the theoretical analysis of the droplet behavior.

When the channel holding the droplet has a contraction ratio of $\varepsilon>0$, the bifurcation diagram loses its pitchfork nature shape, and two separate branches appear. A primary branch then goes from nearly symmetric state to asymmetric location as it passes through the droplet's critical volume. The primary branch is found to be stable at all its equilibrium states. The secondary branch is also asymmetric, and it bifurcates from a modified critical volume V_{mcr}. The large-amplitude state of the secondary branch is stable, and the small-amplitude is unstable. As the contraction ratio ε gets larger, the modified critical volume V_{mcr} also becomes larger. We found that the unstable branch of the secondary branch deviates further from the symmetry line as the droplet volume gets larger. In addition, that deviation rate with respect to the droplet cap volume becomes higher as ε becomes large. However, no maximum droplet volumes were observed.

When g is considered, β and η have values greater than zero, which alters the relationship between R_U and R_L. Gravity also changes the pitchfork bifurcation diagram of a droplet system into two separate branches with equilibrium (and steady) states. Similar to the contracted channel case, the primary branch describes a gradual and stable change of the droplet state from nearly symmetric to asymmetric as the droplet volume, V, is increased above V_{cr}. The secondary branch appears at a modified critical volume, V_{mcr}, and describes two additional asymmetric states for $V>V_{mcr}$. Both branches have maximum volumes to sustain its weight. The value of V_{p_max} decreases as

β increases. The secondary branches of droplet states are in the form of nested loops that consist of an upper stable state and a lower unstable state. Both upper and lower states of the secondary branch are bounded by V_{mcr} and V_{s_max}. As the value of β increases, V_{mcr} increases, and V_{s_max} decreases, which leads to smaller loops that are nested inside each other. There is a limit value of β for the secondary stability branch to exist, and this limit is called β_{cr}. Using analytical results, the critical β is approximately equal to $\beta_{cr} \approx 0.127$. When $\beta > \beta_{cr}$, there is only one stable droplet state, and that is the primary asymmetric state that extends from V=0 to V_{p_max}. When $\beta < \beta_{cr}$, both primary and secondary branches exist. Changing some of the major properties of β, namely ρ, γ and g, has a significant effect on the dynamics of the center of mass. Gravity, however, has the most impact as it shows a higher amplitude oscillation that can lead the droplet to move from the secondary stability branch towards its primary stable branch. However, it will settle there if and only if $V<V_{p\_max}$. When $V>V_{p\_max}$, analytically there should be no solution. However, CFD shows more solutions beyond the V_{p_max}, all these solutions deviate as the droplet volume gets larger until it reaches a certain volume where the droplet will just detach from the channel walls. The deviation is due to the deformation of the droplet interface as the volume gets beyond V_{p_max}, and the detachment from the channel wall is because the droplet becomes sufficiently large that the capillary force cannot keep the droplet pinned in the channel.

6.2 Future work

The current study has successfully showed the limitation of gravity force, through the value of β, that a droplet can sustain while it is suspended in a vertical

direction. Also it showed the effect of the contraction in channel wall on the stability behavior of the droplet system. However, more CFD studies can be done to investigate the stability of a similar droplet system design, also more ideas can implemented from combining both current studies to improve existing applications that have already been tested experimentally.

In the current investigation, the stability of the droplet is studied under a constant gravitational force. A suggested future study might be the case to consider periodic external force field, which has been done experimentally by many researchers (references [5, 10, 15, 39, 40]). Another investigation may include reducing the droplet system to the nano-scale, and observe the droplet stability behavior at that very small scale. Another recommendation might be to examine the behavior of the droplet when surfactant molecules are introduced at the droplet interface as that may have effect on the droplet surface tension, and therefore the droplet's capillary force. A final recommendation is to investigate the introduction of two types of asymmetry in the droplet system; a force field asymmetry through the gravitational force and geometrical asymmetry through the contraction of a channel, and examine their effect on stability of the droplet system.

REFERENCES

1. Vogel, M.J. and P.H. Steen, *Capillarity-based switchable adhesion.* Proceedings of the National Academy of Sciences of the United States of America, 2010. **107**(8): p. 3377-3381.

2. Malouin, B.A., et al., *Electromagnetic liquid pistons for capillarity-based pumping.* Lab on a Chip, 2011. **11**(3): p. 393-397.

3. Baird, E. and K. Mohseni, *Digitized Heat Transfer: A New Paradigm for Thermal Management of Compact Micro Systems.* Components and Packaging Technologies, IEEE Transactions on, 2008. **31**(1): p. 143-151.

4. Paik, P., V.K. Pamula, and K. Chakrabarty. *Thermal effects on droplet transport in digital microfluidics with applications to chip cooling*. in *Thermal and Thermomechanical Phenomena in Electronic Systems, 2004. ITHERM '04. The Ninth Intersociety Conference on*. 2004.

5. Lopez, C.A. and A.H. Hirsa, *Fast focusing using a pinned-contact oscillating liquid lens.* Nature Photonics, 2008. **2**(10): p. 610-613.

6. Stan, C.A., *Liquid optics: Oscillating lenses focus fast.* Nat Photon, 2008. **2**(10): p. 595-596.

7. Olles, J.D., et al., *Optical performance of an oscillating, pinned-contact double droplet liquid lens.* Optics Express, 2011. **19**(20): p. 19399-19406.

8. Theisen, E.A., et al., *Capillary dynamics of coupled spherical-cap droplets.* Journal of Fluid Mechanics, 2007. **580**: p. 495-505.

9. Slobozhanin, L.A. and J.I.D. Alexander, *The stability of two connected drops suspended from the edges of circular holes.* Journal of Fluid Mechanics, 2006. **563**: p. 319-355.

10. Slater, D.M., et al., *Chaotic motions of a forced droplet-droplet oscillator.* Physics of Fluids, 2008. **20**(9): p. 1 -8

11. Russo, M.J. and P.H. Steen, *Instability of Rotund Capillary Bridges to General Disturbances - Experiment and Theory.* Journal of Colloid and Interface Science, 1986. **113**(1): p. 154-163.

12. Ramalingam, S.K. and O.A. Basaran, *Axisymmetric oscillation modes of a double droplet system.* Physics of Fluids, 2010. **22**(11): p. 1-8.

13. Bostwick, J.B. and P.H. Steen, *Capillary oscillations of a constrained liquid drop.* Physics of Fluids, 2009. **21**(3): p. 1-10.

14. Pozrikidis, C., *Stability of sessile and pendant liquid drops.* Journal of Engineering Mathematics, 2012. **72**(1): p. 1-20.

15. Hirsa, A.H., et al., *Low-dissipation capillary switches at small scales.* Applied Physics Letters, 2005. **86**(1).

16. Malouin, B.A., M.J. Vogel, and A.H. Hirsa, *Electromagnetic control of coupled droplets.* Applied Physics Letters, 2010. **96**(21).

17. Majumdar, S.R. and D.H. Michael, *The Equilibrium and Stability of Two Dimensional Pendent Drops.* Proceedings of the Royal Society of London. Series A, Mathematical and Physical Sciences, 1976. **351**(1664): p. 89-115.

18. Chen, L.H. and H.C. Chang, *Equilibrium Shapes of Liquid Bridges under Gravity - Symmetry-Breaking and Imperfect Bifurcations of Two-Dimensional Bridges.* Journal of Colloid and Interface Science, 1987. **120**(2): p. 377-388.

19. Brown, R.A. and L.E. Scriven, *ON THE MULTIPLE EQUILIBRIUM SHAPES AND STABILITY OF AN INTERFACE PINNED ON A SLOT.* Journal of Colloid and Interface Science, 1980. **78**(2): p. 528-542.

20. FLUENT, *Fluent 6.3 Guide.* Fluent Inc.

21. White, F.M., *Viscous fluid flow*. 3rd ed. McGraw-Hill series in mechanical engineering2006, New York, NY: McGraw-Hill Higher Education. xxi, 629 p.

22. Rodriguez-Valverde, M.A., M.A. Cabrerizo-Vilchez, and R. Hidalgo-Alvarez, *The Young-Laplace equation links capillarity with geometrical optics.* European Journal of Physics, 2003. **24**(2): p. 159-168.

23. Nichita, B.A., I. Zun, and J.R. Thome, *A Level Set Method Coupled With a Volume of Fluid Method for Modeling of Gas-Liquid Interface in Bubbly Flow*. Journal of Fluids Engineering-Transactions of the Asme, 2010. **132**(8): p. 1-15.

24. Fachinotti, V.D. and A. Cardona, *A fixed-mesh Eulerian-Lagrangian approach for stress analysis in continuous casting.* International Journal for Numerical Methods in Engineering, 2007. **70**(6): p. 728-755.

25. Das, T.K., *Prediction of jet breakup length in liquid-liquid systems using the Rayleigh-Tomotika analysis.* Atomization and Sprays, 1997. **7**(5): p. 549-559.

26. Gao, Z.L., D. Vassalos, and Q.X. Gao, *Numerical simulation of water flooding into a damaged vessel's compartment by the volume of fluid method.* Ocean Engineering, 2010. **37**(16): p. 1428-1442.

27. Hoffmann, A.C. and H.A. Vandenbogaard, *A Numerical Investigation of Bubbles Rising at Intermediate Reynolds and Large Weber Numbers.* Industrial & Engineering Chemistry Research, 1995. **34**(1): p. 366-372.

28. Popov, G., et al., *Numerical-Simulation of Viscous-Liquid Sloshing in Arbitrarily Shaped Reservoirs.* Aiaa Journal, 1993. **31**(1): p. 10-11.

29. Harlow, F.H. and J.E. Welch, *Numerical Calculation of Time-Dependent Viscous Incompressible Flow of Fluid with Free Surface.* Physics of Fluids, 1965. **8**(12): p. 2182-2189.

30. Jaworski, Z. and P. Pianko-Oprych, *Two-phase laminar flow simulations in a kenics static mixer - Standard Eulerian and Lagrangian approaches.* Chemical Engineering Research & Design, 2002. **80**(A8): p. 910-916.

31. Acharya, S., et al., *Pressure-based finite-volume methods in computational fluid dynamics.* Journal of Heat Transfer-Transactions of the Asme, 2007. **129**(4): p. 407-424.

32. Chorin, A.J., *Numerical Solution of Navier-Stokes Equations.* Mathematics of Computation, 1968. **22**(104): p. 745-762.

33. Tannehill, J.C., D.A. Anderson, and R.H. Pletcher, *Computational fluid mechanics and heat transfer*. 2nd ed. Series in computational and physical processes in mechanics and thermal sciences1997, Washington, DC: Taylor & Francis. xxi, 792 p.

34. Tecplot, *Tecplot 360.* TECPLOT.

35. Ku, T.C., J.H. Ramsey, and W.C. Clinton, *Calculation of Liquid Droplet Profiles from Closed-Form Solution of Young-Laplace Equation.* Ibm Journal of Research and Development, 1968. **12**(6): p. 441-447.

36. Faraldo-Gomez, J.D. and B. Roux, *Characterization of conformational equilibria through Hamiltonian and temperature replica-exchange simulations: Assessing entropic and environmental effects.* Journal of Computational Chemistry, 2007. **28**(10): p. 1634-1647.

37. Wilkinson, B. and C.M. Allen, *Parallel programming : techniques and applications using networked workstations and parallel computers* 1999, Upper Saddle River, N.J.: Prentice Hall. xv, 431 p.

38. Golovinskiy, A., J. Podolak, and T. Funkhouser, *Symmetry-Aware Mesh Processing Mathematics of Surfaces XIII*, E. Hancock, R. Martin, and M. Sabin, Editors. 2009, Springer Berlin / Heidelberg. p. 170-188.

39. Tsukada, T., et al., *A Theoretical and Experimental-Study on the Oscillation of a Hanging Drop.* Journal of Chemical Engineering of Japan, 1987. **20**(1): p. 88-93.

40. Basaran, O.A., *Nonlinear Oscillations of Viscous-Liquid Drops.* Journal of Fluid Mechanics, 1992. **241**: p. 169-198.

41. Gradshtein, I.S., I.M. Ryzhik, and A. Jeffrey, *Table of integrals, series, and products*. Corr. and enl. ed1980, New York: Academic Press. xlv, 1160 p.

APPENDIX A: CENTER OF MASS CALCULATION FOR STRAIGHT CHANNEL

The center of mass at the equilibrium state has been formulated so that it is as a function of h_i and r.

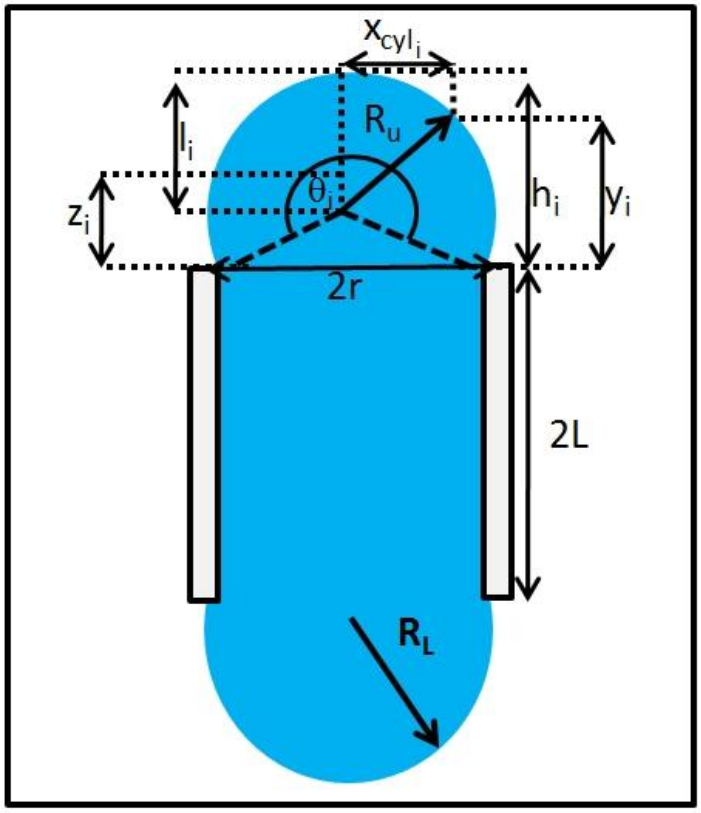

Figure A-1 Droplet domain labels.

The total droplet volume, V_T, is the sum of the two cap volumes $V_U + V_L$ and the volume of the liquid in the channel V_0, where

$$V_T = V_0 + V_U + V_L, \quad \text{(A-1)}$$

$$V_0 = 4rL, \text{ and} \quad \text{(A-2)}$$

$$V_i = \frac{1}{2} R_i^2 (\theta_i - \sin\theta_i). \quad \text{(A-3)}$$

The subscript, i, denotes the upper or lower cap, (U or L).

From Figure A-1

$$\theta_i = 2\sin^{-1}\left(\frac{r}{R_i}\right). \quad \text{(A-4)}$$

After substituting equation A-4 in equation A-3, Equation A-1 yields

$$V_T = 4rL + \frac{1}{2}[R_i^2(\theta_i - \sin\theta_i) + R_i^2(\theta_i - \sin\theta_i)]. \quad \text{(A-5)}$$

Eliminating radius of curvature R_i for the droplet height h_i

$$h_i = R_i\left(1 - \cos\left(\frac{\theta_i}{2}\right)\right) \quad \text{(A-6)}$$

$$\frac{h_i}{R_i} = \left(1 - \cos\left(\frac{\theta_i}{2}\right)\right) = 1 \mp \left(1 - \sin^2\left(\frac{\theta_i}{2}\right)\right) = 1 \mp \left(1 - \frac{r^2}{R_i^2}\right)^{\frac{1}{2}} \quad \text{(A-7)}$$

After futher manipulation we get the radius of curvature R_i as a function of the radius of the channel and the droplet height as follows:

$$R_i = \frac{h_i^2 + r^2}{2h_i} \quad \text{(A-8)}$$

Based on the relation between the variable point x_{cyl_i} and the integration variable y_i in Figure A-1, we find:

$$l_i^2 = y_i^2 + \frac{r^2 - h_i^2}{h_i} y_i + \frac{\left(r^2 - h_i^2\right)^2}{4h_i^2} \ . \quad \text{(A-9)}$$

Since $R_i^2 = x_{cyl_i}^2 + l_i^2$, $\quad x_{cyl_i}$ becomes

$$x_{cyl_i}^2 = -y_i^2 + \frac{h_i^2 - r^2}{h_i} y_i + r^2 \quad \text{(A-10)}$$

Now we calculate the z_i and Y_{cm}, where z_i is the center of mass for V_i

$$YV_T = +(z_U V_U) + (LV_U) - (z_L V_L) - (LV_L)$$

Since $2I_i = z_i V_i$, the center of mass becomes

$$Y = \frac{2}{V_T}(I_U - I_L) + \frac{L}{V_T}(V_U - V_L), \tag{A-11}$$

where $I_i = \int_0^h y_i \left(-y^2 + \frac{h_i^2 - r^2}{h_i} y + r^2\right)_i^{\frac{1}{2}} dy_i$

Using reference [41], the above integral becomes

$$I_i = \frac{(h_i^2 - r^2)(h_i^2 + r^2)^2}{16 h_i^3}\left[\sin^{-1}\left(\frac{h_i^2 - r^2}{h_i^2 + r^2}\right) + \frac{1}{2}\pi\right] + \frac{r^3}{3} + \frac{r(h_i^2 - r^2)^2}{8 h_i^2} \tag{A-12}$$

APPENDIX B: CENTER OF MASS CALCULATION FOR CONTRACTED CHANNEL

The center of mass at the equilibrium state has been formulated so that it is as a function of h_i and r_i. The total droplet volume, V_T, is the sum of the two cap volumes $V_U + V_L$ and the volume of the liquid in the channel V_{0L} and V_{0U}, where

$$V_T = V_{0U} + V_{0L} + V_U + V_L, \tag{B-1}$$

$$V_{0U} = 4r_U L, \text{ and} \tag{B-2b}$$

$$V_{0L} = 4r_L L, \text{ and} \tag{B-2b}$$

$$V_i = \frac{1}{2}R_i^2(\theta_i - \sin\theta_i). \tag{B-3}$$

The subscript, i, denotes the upper or lower cap, (U or L).

From Figure A-1

$$\theta_i = 2\sin^{-1}\left(\frac{r_i}{R_i}\right). \tag{B-4}$$

After substituting equation A-4 in equation A-3, Equation A-1 yields

$$V_T = 4rL + \frac{1}{2}[R_i^2(\theta_i - \sin\theta_i) + R_i^2(\theta_i - \sin\theta_i)]. \tag{B-5}$$

Eliminating radius of curvature R_i for the droplet height h_i

$$h_i = R_i\left(1 - \cos\left(\frac{\theta_i}{2}\right)\right) \tag{B-6}$$

$$\frac{h_i}{R_i} = \left(1 - \cos\left(\frac{\theta_i}{2}\right)\right) = 1 \mp \left(1 - \sin^2\left(\frac{\theta_i}{2}\right)\right) = 1 \mp \left(1 - \frac{{r_i}^2}{R_i^2}\right)^{\frac{1}{2}} \tag{B-7}$$

After futher manipulation we get the radius of curvature R_i as a function of the radius of the channel and the droplet height as follows:

$$R_i = \frac{h_i^2 + {r_i}^2}{2h_i} \tag{B-8}$$

Based on the relation between the variable point x_{cyl_i} and the integration variable y_i in Figure A-1, we find:

$$l_i^2 = y_i^2 + \frac{r_i{}^2 - h_i^2}{h_i} y_i + \frac{\left(r_i{}^2 - h_i^2\right)^2}{4h_i^2} \quad . \tag{B-9}$$

Since $R_i^2 = x_{cyl_i}^2 + l_i^2$, x_{cyl_i} becomes

$$x_{cyl_i}^2 = -y_i^2 + \frac{h_i^2 - r_i{}^2}{h_i} y_i + r_i{}^2 \tag{B-10}$$

Now we calculate the z_i and Y_{cm}, where z_i is the center of mass for V_i

$$YV_T = (z_U V_U) + (LV_U) - (z_L V_L) - (LV_L) - \frac{LV_{0L}}{4} + \frac{LV_{0U}}{4}$$

Since $2I_i = z_i V_i$, the center of mass becomes

$$Y = \frac{2}{V_T}(I_U - I_L) + \frac{L}{V_T}(V_U - V_L) + \frac{L}{2V_T}(V_{0U} - V_{0L}), \tag{B-11}$$

where $I_i = \int_0^h y_i \left(-y^2 + \frac{h_i^2 - r^2}{h_i} y + r_i{}^2\right)_i^{\frac{1}{2}} dy_i$

Using reference [41], the above integral becomes

$$I_i = \frac{\left(h_i^2 - r_i{}^2\right)\left(h_i^2 + r_i{}^2\right)^2}{16h_i^3}\left[\sin^{-1}\left(\frac{h_i^2 - r_i{}^2}{h_i^2 + r_i{}^2}\right) + \frac{1}{2}\pi\right] + \frac{r^3}{3} + \frac{r_i\left(h_i^2 - r_i{}^2\right)^2}{8h_i^2} \tag{B-12}$$